

**STUDY OF OPTICAL DESTRUCTION TECHNIQUES FOR
OPTICAL DISCS**

by

Taeyoung Choi

A Dissertation Submitted to the Faculty of the
COLLEGE OF OPTICAL SCIENCES

In Partial Fulfillment of the Requirements
For the Degree of

DOCTOR OF PHILOSOPHY

In the Graduate College

THE UNIVERSITY OF ARIZONA

2008

UMI Number: 3303987



UMI Microform 3303987

Copyright 2008 by ProQuest Information and Learning Company.
All rights reserved. This microform edition is protected against
unauthorized copying under Title 17, United States Code.

ProQuest Information and Learning Company
300 North Zeeb Road
P.O. Box 1346
Ann Arbor, MI 48106-1346

THE UNIVERSITY OF ARIZONA
GRADUATE COLLEGE

As members of the Dissertation Committee, we certify that we have read the dissertation prepared by Taeyoung Choi entitled Study of Optical Destruction Techniques for Optical Discs and recommend that it be accepted as fulfilling the dissertation requirement for the Degree of Doctor of Philosophy.

Tom D. Milster Date: 05/02/2008

Alan Kost Date: 05/02/2008

José M. Sasián Date: 05/02/2008

Final approval and acceptance of this dissertation is contingent upon the candidate's submission of the final copies of the dissertation to the Graduate College.

I hereby certify that I have read this dissertation prepared under my direction and recommend that it be accepted as fulfilling the dissertation requirement.

Dissertation Director: Tom D. Milster Date: 05/02/2008

STATEMENT BY AUTHOR

This dissertation has been submitted in partial fulfillment of requirements for an advanced degree at the University of Arizona and is deposited in the University Library to be made available to borrowers under rules of the Library.

Brief quotations from this dissertation are allowable without special permission, provided that accurate acknowledgment of source is made. Requests for permission for extended quotation from or reproduction of this manuscript in whole or in part may be granted by the head of the major department or the Dean of the Graduate College when in his or her judgment the proposed use of the material is in the interests of scholarship. In all other instances, however, permission must be obtained from the author.

SIGNED: Taeyoung Choi

TABLE OF CONTENTS

LIST OF FIGURES	7
LIST OF TABLES	16
ABSTRACT	17
1 INTRODUCTION	19
1.1 Basic description of research	19
1.2 Motivation for this study.....	20
1.3 Outline of dissertation.....	21
2 BACKGROUND	23
2.1 Optical data storage.....	23
2.1.1 Principles of optical data storage	25
2.1.2 Light source and optical beam spot	27
2.1.3 Storage media and various formats of optical data storage technology.....	29
2.1.4 Focus and tracking servo systems.....	31
2.1.5 Performance	37
2.2 Gaussian beams and Hermite-Gaussian beams.....	38
2.2.1 Gaussian beam	39
2.2.2 Hermite-Gaussian beams	42
2.3 High-power laser diode (HPLD).....	45
2.3.1 Introduction.....	45
2.3.2 Basic optical characteristics of HPLD beam	49
2.3.3 Modeling methods of an optical system using a laser beam.....	54
3 BASIC REQUIREMENTS OF OPTICAL DATA DESTRUCTION (ODD) SYSTEM.....	57
3.1 Light source	57
3.2 Focus sensor.....	59
3.3 Package dimensions	60
3.4 Objective lens and actuator.....	62
3.5 Detector.....	63
3.6 Servo electronics.....	63
4 INVESTIGATION INTO HPLD BEAMS AND METHODS OF MODELING OPTICAL SYSTEM USING HPLD	65
4.1 Lateral modes of HPLD	65
4.2 Coherence of HPLD beam	70

TABLE OF CONTENTS - *Continued*

4.3	Modeling of an optical system using HPLD	79
5	DESIGN AND CONSTRUCTION OF THE ODD SYSTEM	94
5.1	Basic function and optical configuration	94
5.2	Optical characteristics	96
5.3	Thermal and mechanical considerations	97
5.4	Construction of ODD system	99
6	DOE FOCUS SERVO	103
6.1	Basics of DOEs	103
6.2	Conceptual operation of DOE focus sensor	105
6.3	Design of DOE focus sensor	108
6.4	Fabrication of the DOE	114
6.4.1	Fabrication tool and procedure	114
6.4.2	Problem with a single-step fabrication and solutions	115
6.5	Simulation of the ODD system	121
6.6	Simulation and characterization of DOE focus servo	124
6.7	Error sources and tolerance analysis	130
6.8	FES from the constructed ODD system	141
7	CHANGE IN DATA MARKS AND GROOVE STRUCTURES OF CD-R DISCS IN RESPONSE TO A HIGH POWER LASER BEAM	144
7.1	Recording mechanism in writable media	145
7.2	Exposure experiments	146
7.3	Dynamic Measurement and Results	148
7.4	Static Measurements and Results	150
7.5	Chapter conclusions	156
8	FURTHER DESTRUCTION TESTS USING ODD SYSTEM	158
8.1	Introduction	158
8.2	Destruction test of CD-ROM discs	159
8.3	Destruction test of CD-R discs	160
8.4	Destruction test of CD-RW discs	162
8.5	Summary of the destruction test results	164
9	CONCLUSIONS AND FUTURE WORK	165
9.1	Conclusions	165
9.2	Future work	168

TABLE OF CONTENTS - *Continued*

APPENDIX I: ACRONYMS AND ABBREVIATIONS	170
APPENDIX II: BLOCKDIAGRAM OF LABVIEW PROGRAM CONTROLLING ODD SYSTEM.....	172
APPENDIX III: PUBLISHED JOURNAL PAPER	174
REFERENCES	188

LIST OF FIGURES

Figure 2.1 Small sections of a compact disc (CD) and a digital versatile disc (DVD) are displayed relative to the laser spots that are focused onto them during recording and readout.....	24
Figure 2.2 Optical recording. The process of recording data onto an optical disc starts with the user input data stream converted to a current drive signal for the laser diode. Intense pulses from the laser cause physical changes in the surface of the recording medium as the disc spins, which result in spiral tracks of data marks.....	26
Figure 2.3 Optical retrieval. A constant, low power laser beam scans a data track to readout data from the disc. Reflected light, which is modulated by the data mark pattern, causes modulation in the reflected light. The reflected light is directed to servo and data detectors with a beam splitter, which convert the light modulation in a current signal that is then decoded.....	27
Figure 2.4 An optical disc is used so that the focusing laser light is passed through the clear side of the substrate and illuminates the data-mark pattern on the other side. The thickness of the cover layer is designed to reduce effects of contamination on the surface of the disc, like dust or fingerprints.....	29
Figure 2.5 The astigmatic focusing technique uses a special lens in the servo optics before a quadrant-cell detector. The servo optics lens introduces a small amount of astigmatism into the beam along a diagonal direction on the detector. As the spinning disc goes into and out of focus, the astigmatism forces the light spot to change shape. A difference signal from the detector quadrants produces an FES that indicates the amount of defocus.....	33
Figure 2.6 The push-pull tracking error signal (TES) is generated by using a split-cell servo detector and sensing the difference in light level between the cells. Since grooves of the disc diffract light like a grating, diffracted orders overlap and generate an interference pattern. As the laser spot moves off track, the relative phase change in the diffracted orders produces bright and dark patterns on the detector. The TES difference signal indicates the relative off-track location of the laser spot	34
Figure 2.7 The three-spot tracking sensor uses two auxiliary laser spots that ride edges of the track as the disc spins. The spot are reimaged onto separate detector elements. If the data track is not centered, the amount of light reflected from each auxiliary spot changes. One detector spot becomes brighter, and the other dims. A difference signal produces a reliable TES.....	35
Figure 2.8 Evolution of a Gaussian beam.....	40

LIST OF FIGURES - *Continued*

Figure 2.9 Plot of the lens formula for a lowest-order Gaussian beam. The object and image distances normalized by f are plotted for several values of a parameter ($z_R/f = 0, 0.25, 0.5, 1, 2$)	41
Figure 2.10 (a) Simulated 2-D Hermite-Gaussian modes and (b) transverse modes of a CO ₂ laser observed in [Kogelnik 1967]. In (a), transverse irradiances simulated over the $6w_o \times 6w_o$ area. The mode numbers (p, q) are presented on top of the corresponding modes.	45
Figure 2.11 (a) Geometry of an LD and the emerging beam and (b) optical power vs. injection (P-I) curve along with spectra below and above the threshold current I_{th} ..	46
Figure 2.12 (a) Spectrum of HPLD output beam ($I/I_{th} = 1.08$), (b) image of multiple lasing modes from the HPLD operating at $I/I_{th} = 1.56$ and (c) images of lateral modes belonging to one longitudinal mode when the HPLD is operated at $I/I_{th} = 1, 1.03, 1.17$ and 1.6 [Mailhot <i>et al.</i> 2000].	50
Figure 2.13 (a) Near-field irradiance profile and (b) far-field intensity profile of the HPLD output beam in the lateral (x) direction. Numbers 1 and 2 next to the curves indicate the injection current levels of $I/I_{th} = 1.02$ and 1.58, respectively [Mailhot <i>et al.</i> 2000].	51
Figure 2.14 (a) Parabolic gain and refractive index profiles in the x direction parallel to the active layer. (b) Phase front propagating within an active layer. This phase front is planar in vertical (y) direction and cylindrical in the lateral direction. The emerging beam from an LD looks like it originates from a point source at the facet in the vertical (y) direction but from a point source inside the LD cavity in the lateral (x) direction, which implies inherent astigmatism.	53
Figure 3.1 Images of a phthalocyanine CD-R disc exposed to a focused CO ₂ laser beam. (a) Undamaged data marks on the data layer (imaged by a 100 \times microscope objective), and (b) top-view and (c) side-view of melted and bubbled polycarbonate (imaged by a 10 \times microscope objective).	58
Figure 3.2 Schematic of a small-form factor ODD device with an evaluation head. The proposed dimensions of the entire device are 200mm \times 150mm in the disc plane and 100mm in the device height.....	61
Figure 3.3 Diagram of a closed-loop control system for a DOE focus servo.....	64

LIST OF FIGURES - *Continued*

Figure 4.1 Images of near-field irradiances and far-field intensity of the HPLD beam at $I/I_{th}= 1.29$. Multiple peaks in the distributions are indicative of lasing of higher-order lateral modes.....	66
Figure 4.2 Layout of a double-pass monochromator setup for observing the spectrally-resolved HPLD beam. f_2 is the focal length of L2 and the sum of the distances between L2 and DG1 and between DG1 and DG2 is set to be equal to f_2 . The periods of DG1 and DG2 are $0.83\mu\text{m}$ and $1.67\mu\text{m}$, respectively.....	67
Figure 4.3 Images of near-field irradiances of spectrally-resolved HPLD lasing modes ($P_{out}= 1\text{W}$) and the corresponding spectra measured in an optical spectrum analyzer at the injection current of (a) $I/I_{th}= 1.06$, (b) $I/I_{th}= 1.29$ and (c) $I/I_{th}= 1.61$	69
Figure 4.4 Coherence measurement of HPLD beam. (a) Experiment setup, (b) separation at HPLD output aperture and (c) the central portion of the cross slit with slit widths of $26\mu\text{m}$	72
Figure 4.5 Interferogram fringes from the YDSI experiment. The HPLD is operated at $I/I_{th}=1.03$. The numbers in the images are the separation of the two points at the HPLD.....	75
Figure 4.6 Interferogram fringes from the YDSI experiment. The HPLD is operated at $I/I_{th}=1.29$. The numbers in the images are the separation of the two points at the HPLD.....	76
Figure 4.7 Interferogram fringes from the YDSI experiment. The HPLD is operated at $I/I_{th}=1.61$. The numbers in the images are the separation of the two points at the HPLD.....	77
Figure 4.8 Normalized mutual intensity, μ_{12} , as a function of separation at the HPLD aperture at different current levels ($I/I_{th}=1.06, 1.29, 1.61$).	78
Figure 4.9 A simple two-lens setup where Lens 1 geometrically collimates the beam emitted from an HPLD and Lens 2 focuses the incident beam. The solid and dashed lines imply the slow-axis and fast-axis beams, respectively, which are presented on the same plane.....	79

LIST OF FIGURES - *Continued*

- Figure 4.10 Experimental measurements. (a) Transverse irradiance images of an HPLD beam collimated in the fast axis observed at different distances from Lens 1. The vertical (slow-axis) width increases, but the beam remains collimated in the horizontal (fast-axis) direction. (b) Transverse irradiance images of the HPLD beam being focused by Lens 2 through its back focal plane. The minimum beam radii occur at the back focal plane in the horizontal (fast-axis) direction and at around 5.6mm after the back focal plane in the vertical (slow-axis) direction due to the systematic astigmatism of the HPLD beam. All the images are observed at $I/I_{th} = 1.29$ 80
- Figure 4.11 (a) Normalized Gaussian beam waist location after Lens 2 as a function of the normalized beam waist location before Lens 2. The waist location in the slow axis varies significantly as z_2 or the separation between Lens 1 and Lens 2, S , changes. (b), (c), (d) Axial profiles of the beam widths in the fast axis (dashed line) and the slow axis (solid line) through the two-lens system for the three cases: $S / (f_1 + f_2) = 0.2, 1, 5$, respectively. The systematic astigmatism is nontrivial in (b) and (d) when no inherent astigmatism at the HPLD facet is assumed for this simulation. 83
- Figure 4.12 Simulated transverse irradiance images of (a) the lowest-order mode ($p = 0$) and (b) the 5th order mode ($p = 5$) through the back focal plane of Lens 2. (c) Through-focus transverse simulated irradiance images of an incoherent superposition of six low-order modes ($p = 0, 1, 2, 3, 4, 5$) with equal power weight factors..... 85
- Figure 4.13 Slow-axis irradiance profiles of the HPLD lateral modes at the LD facet observed in Fig. 2.13(a) when $I/I_{th} = 1.29$ and the corresponding Hermite-Gaussian modes with $w_o = 32\mu\text{m}$. The irradiances are normalized and the spans of the abscissas are the same in all the plots..... 87
- Figure 4.14 Through-focus transverse beam irradiances when the measured (a) FWHM ($3 \times 25.6^\circ$) and (b) FW1/e² ($3.5 \times 54^\circ$) of the far-field HPLD beam are used as the full widths of the ray angular distribution. 89
- Figure 4.15 Summary of through-focus transverse beam irradiances from the real HPLD beam and from different simulation methods, presented in Figs. 4.10, 4.12, and 4.14. All the images are in the same scale. 92
- Figure 5.1 A schematic of an optical data destruction system. The beam from a high power laser diode is collimated, passes through various optics and focused on the data layer of a disk. The focus-lock is achieved with a DOE focus sensor and a closed-loop feedback servo. 95
- Figure 5.2 Mechanical alignment method. A tube with an optical element mounted is placed on top of two round steel rods and is secured by a fixture. 98

LIST OF FIGURES - *Continued*

Figure 5.3 Mechanical drawing of a prototype ODD system.....	100
Figure 5.4 Constructed prototype ODD system.....	101
Figure 5.5 Control panel in LabVIEW program.....	102
Figure 6.1 Knife-edge focusing method. (a) disc in focus ($FES = 0$), (b) disc too close to the objective lens ($FES > 0$) and (c) disc too far from the lens ($FES < 0$).....	106
Figure 6.2 Mechanism of focus error signal generation. The reflected beam from a disc is incident on the DOE comprised of two slanted gratings, which produce two diffracted patterns. Only $+3^{\text{rd}}$ order beams fall on the quad-cell detector. Depending on the direction of defocus at the disc, the error signal becomes either positive or negative.	107
Figure 6.3 (a) Geometry of the DOE comprising two slanted gratings and (b) diffracted beams from Grating II as observed at the detector. Λ is the grating period, θ_g is the grating angle, the z -axis is the optical axis, and (D_x, D_y) are the dimensions of the quad-cell active area.	109
Figure 6.4 (a) The region of DOE design parameters (Λ, θ_g) that separate the two $+3^{\text{rd}}$ order beams in the x -axis are shaded, and (b) the curves for several c values that separate the $+3^{\text{rd}}$ orders from the other orders in the y -axis are overlapped with the shaded region in (a). The “ \times ” mark in (b) indicates the selected parameters for the DOE for the prototype ODD system. See Section 6.3 for more details.....	113
Figure 6.5 (a) Designed DOE in a bitmap representation and (b) microscopic image of the fabricated DOE on a glass substrate. Pixelation in the designed DOE is apparently transferred to the fabricated DOE. Pixelation results from the bit-wise representation of the pattern and generates unwanted diffraction patterns.	118
Figure 6.6 The first approach to solve the pixelation problem. (a) The designed DOE pattern is rotated by the grating angle so that Grating I is written along the laser fast-scan direction and Grating II is written at a steep angle of twice the grating angle. Images of the fabricated Grating I (b) and Grating II (c). Pixelation is completely removed from Grating I, but not from Grating II (c).....	119

LIST OF FIGURES - *Continued*

Figure 6.7 The second approach to solve the pixelation problem. (a) Bitmap representation of Masks I and II for Gratings I and II and alignment marks. Both gratings are written in the fast-scan direction so that the line-edges are straight. (b) Images of alignment marks printed on the DOE substrate after double exposure. (c) Fabricated DOE ($\Lambda = 30.5\mu\text{m}$, $\theta_g = 42^\circ$) on a chrome substrate. A microscopic image of the region near the grating boundary is also provided.....	120
Figure 6.8 Picture of diffraction patterns of the DOE fabricated in the two-step method when illuminated by a collimated HeNe laser beam. Patterns I and II are generated from Gratings I and II, respectively. No unwanted diffraction patterns are present due to straight line edges of the gratings. The 3 rd order beams are used for focus sensing.	121
Figure 6.9 Layouts of (a) the imaging subsystem with traces of rays from the source to the disc and (b) the whole ODD system with traces of rays from source to disc and to detector in the non-sequential raytracing (NSR) model.	122
Figure 6.10 Grayscale transverse irradiances of rays simulated using an NSR method at the source, the disc, and the detector plane. The irradiance distribution in (c) is plotted in log-scale to show all the present diffraction orders regardless of their diffraction efficiency.....	123
Figure 6.11 Simulated diffraction patterns on the detector plane with defocus at the disc obtained using the NSR method. The irradiance distribution is plotted in log-scale to show all the present diffraction orders regardless of their diffraction efficiency. The size of observation window is $4 \times 5\text{mm}$, and a quad-cell detector ($1.2 \times 0.6\text{mm}$) is drawn to have the +3 rd orders on it.	123
Figure 6.12 A typical FES is drawn along with several performance parameters of a focus servo, which are the slope through best focus, lock-on range, linearity within $\pm 2\mu\text{m}$ and focus offset.....	125
Figure 6.13 Simulated signals as a function of defocus at disc ($ \Delta z < 50\mu\text{m}$). (a) Two summed detector signals (A+C, B+D) and (b) a normalized FES.....	128
Figure 6.14 Simulated signals as a function of defocus at disc ($ \Delta z < 1\text{mm}$). (a) Four detector signals (A, B, C, D), (b) two summed detector signals (A+C, B+D) and (c) a normalized FES.....	129

LIST OF FIGURES - *Continued*

Figure 6.15 Simulated signals when the HPLD is rotated about the z axis ($ \Delta z < 50\mu\text{m}$). The first row shows four detector signals (A, B, C, D), the second row shows two summed detector signals (A+C, B+D) and the bottom row shows normalized FES signals.	132
Figure 6.16 Simulated signals when the HPLD is rotated about the z axis ($ \Delta z < 1\text{mm}$). The first row shows four detector signals (A, B, C, D), the second row shows two summed detector signals (A+C, B+D) and the bottom row shows normalized FES signals.	133
Figure 6.17 Simulated signals when the DOE is rotated about the z axis ($ \Delta z < 50\mu\text{m}$). The first row shows four detector signals (A, B, C, D), the second row shows two summed detector signals (A+C, B+D) and the bottom row shows normalized FES signals.	134
Figure 6.18 Simulated signals when the DOE is rotated about the z axis ($ \Delta z < 1\text{mm}$). The first row shows four detector signals (A, B, C, D), the second row shows two summed detector signals (A+C, B+D) and the bottom row shows normalized FES signals.	135
Figure 6.19 Simulated signals when the detector is decentered in the x axis ($ \Delta z < 50\mu\text{m}$). The first row shows four detector signals (A, B, C, D), the second row shows two summed detector signals (A+C, B+D) and the bottom row shows normalized FES signals.	136
Figure 6.20 Simulated signals when the detector is decentered in the x axis ($ \Delta z < 1\text{mm}$). The first row shows four detector signals (A, B, C, D), the second row shows two summed detector signals (A+C, B+D) and the bottom row shows normalized FES signals.	137
Figure 6.21 Simulated signals when the detector is decentered in the y axis ($ \Delta z < 50\mu\text{m}$). The first row shows four detector signals (A, B, C, D), the second row shows two summed detector signals (A+C, B+D) and the bottom row shows normalized FES signals.	138
Figure 6.22 Simulated signals when the detector is decentered in the y axis ($ \Delta z < 1\text{mm}$). The first row shows four detector signals (A, B, C, D), the second row shows two summed detector signals (A+C, B+D) and the bottom row shows normalized FES signals.	139

LIST OF FIGURES - *Continued*

Figure 6.23 Experimental detector signals and FES. Two summed detector signals for a defocus range of (a) $ \Delta z < 20\mu\text{m}$ and (b) $ \Delta z < 1\text{mm}$, and (c) FES for $ \Delta z < 1\text{mm}$. The humps in (b) and (c) originate from intense +1 st and/or 0 th orders penetrating into the quad-cell detector when a large defocus is introduced, and are only observed in a focus search mode of the actuator.....	143
Figure 7.1 Recording mechanism in writable media. (a), (b) dye/reflector feature and (c) substrate feature.....	146
Figure 7.2 RF data signals and histograms from (a) unexposed and (b), (c) exposed sections of phthalocyanine-dye discs ($\text{EX}= 9.4\text{nJ}/\mu\text{m}^2$). Small boxed portions of the upper signals are magnified in the lower signals. In (c), undestroyed data signals are intermittently shown due to the use of an overlap factor smaller than one.	149
Figure 7.3 Optical microscope images of unexposed and exposed data marks on cyanine discs. (a) Unexposed data marks on dye/substrate sample, (b) exposed data marks on dye/substrate sample ($\text{EX}= 4.3\text{nJ}/\mu\text{m}^2$) and (c) exposed data marks on substrate-only sample ($\text{EX}= 4.3\text{nJ}/\mu\text{m}^2$). In (b) and (c), the upper portion of the observation area is unexposed.	151
Figure 7.4 Profiles of a cyanine-dye disc measured using an AFM (a) before and (b) after exposure to a high-power laser beam ($\text{EX}= 4.3\text{nJ}/\mu\text{m}^2$).	151
Figure 7.5 Optical microscope images of unexposed and exposed data marks on phthalocyanine discs. (a) Unexposed data marks on dye/substrate sample, (b) exposed data marks on dye/substrate sample ($\text{EX}= 2.2\text{nJ}/\mu\text{m}^2$), (c) exposed data marks on substrate-only sample ($\text{EX}= 2.2\text{nJ}/\mu\text{m}^2$), (d) exposed data marks on dye/substrate sample ($\text{EX}= 9.4\text{nJ}/\mu\text{m}^2$) and (e) exposed data marks on substrate-only sample ($\text{EX}= 9.4\text{nJ}/\mu\text{m}^2$). In each figure, a representative data mark is circled.	153
Figure 7.6 Profiles of a phthalocyanine-dye disc measured using an AFM (a) before and (b) after exposure ($\text{EX}= 9.4\text{nJ}/\mu\text{m}^2$).	154
Figure 7.7 Optical microscope images of unexposed and exposed data marks on azo discs. (a) Unexposed data marks on dye/substrate sample, (b) exposed data marks on dye/substrate sample ($\text{EX}= 2.8\text{nJ}/\mu\text{m}^2$) and (c) exposed data marks on substrate-only sample ($\text{EX}= 2.8\text{nJ}/\mu\text{m}^2$). In (b) and (c), a small upper portion of the observation area is unexposed.	155
Figure 7.7 Profiles of an azo-dye disc measured using an AFM (a) before and (b) after exposure to a laser beam ($\text{EX}= 2.8\text{nJ}/\mu\text{m}^2$).	156

LIST OF FIGURES - *Continued*

- Figure 8.1 Optical microscope images of unexposed and exposed data marks on CD-ROM disks. (a) Unexposed and exposed data marks on through-substrate sample ($EX= 50nJ/\mu m^2$), and (b) unexposed and exposed data marks on through-substrate sample ($EX= 200nJ/\mu m^2$). In each image, an upper portion of the observation area is unexposed. On the exposed areas, aluminum in the reflective layers oxidizes, making data marks indiscernible. 160
- Figure 8.2 Optical microscope images of the unexposed and exposed data marks on phthalocyanine-dye CD-R disks. (a) Unexposed and exposed data marks on substrate-only sample ($EX= 15nJ/\mu m^2$). (b) Unexposed and exposed data marks on through-substrate sample ($EX= 35.5nJ/\mu m^2$). Bubbles are formed in some of the exposed area. (c) Unexposed and exposed data marks on substrate sample ($EX= 35.5nJ/\mu m^2$). The boundary between two exposed areas when exposed at the overlap factor N_o of 1. The radial width of the bubbled area is $130\mu m$. In (a) and (b), the upper portion of the images is unexposed. 161
- Figure 8.3 Optical microscope images of unexposed and exposed data marks on (a) through-substrate sample of a cyanine-dye CD-R disk ($EX= 30nJ/\mu m^2$) and (b) through-substrate sample of an azo-dye CD-R disk ($EX= 23.7nJ/\mu m^2$). In each figure, an upper portion of the observation area is unexposed. 163
- Figure 8.4 Optical microscope images of unexposed and exposed data marks on CD-RW disks.(a) Unexposed and exposed data marks on through-substrate sample ($EX= 17.5nJ/\mu m^2$), and (b) unexposed and exposed data marks on through-substrate sample ($EX= 30nJ/\mu m^2$). 163

LIST OF TABLES

Table 2.1 Comparison of CD, DVD and BD technologies. (All specs are for a single-sided single layer disc).....	24
Table 2.2 Several low-order Hermite polynomials.....	43
Table 4.1 Beam waists and Rayleigh ranges in the slow and fast axes. ($f_1 = 4.52\text{mm}$ and $f_2 = 25.8\text{mm}$ are used for focal lengths of Lens 1 and Lens 2).....	81
Table 4.2 Comparison of Hermite-Gaussian propagation method and NSR method.....	93
Table 6.1 Selected design parameters for the DOE focus sensor.....	114
Table 6.2 Measured efficiencies of diffraction orders from the gratings in the fabricated DOE and theoretical diffraction efficiencies from an ideal binary amplitude grating.....	117
Table 6.3 Simulated performance parameters of the DOE focus servo.....	127
Table 6.4 Performance parameters of the DOE focus servo when the HPLD is rotated about the z axis.....	140
Table 6.5 Performance parameters of the DOE focus servo when the DOE is rotated about the z axis.....	140
Table 6.6 Performance parameters of the DOE focus servo when the detector is decentered in the x axis.....	141
Table 6.7 Performance parameters of the DOE focus servo when the detector is decentered in the y axis.....	141
Table 8.1. Summary of destruction tests on CD-R and CD-RW discs	164

ABSTRACT

The topic of this dissertation is on the investigation of optical techniques for completely destroying data stored in optical discs. Complete and secure destruction of data is important when disposal of an optical disc containing sensitive and possibly classified information is concerned, since some information can be retrieved even from a fragment of a disc. After several candidate techniques and related systems are examined and fundamental system components are identified, an optical data destruction (ODD) system using a focused high power laser beam is devised, and a prototype system is designed and constructed. The ODD system uses a high power laser diode (HPLD) to expose data marks on optical discs and maintains the focused laser beam on a data layer by a focus servo using a diffractive optical element (DOE).

The optical characteristics of the beam emitted from an HPLD are thoroughly investigated, and a few methods of modeling an HPLD beam in an optical system are studied. With the understanding of the HPLD beam properties, a limited-divergence raytracing (LDRT) model is developed to predict the propagation behavior of the HPLD beam in an optical system and shows good agreement with the real HPLD beam. This LDRT method is used to model the HPLD beam in the ODD system and simulate the resultant focus error signal with and without fabrication errors.

The DOE focus sensor overcomes the problems in conventional focus sensors associated with the use of an intense line beam. The DOE comprising two angled gratings

is designed to use only two weak 3rd order beams for focus sensing and fabricated on a chrome-coated glass substrate using a maskless lithography tool.

The constructed ODD system is then used to perform destruction tests on various optical discs, which are examined using static and dynamic methods of data observation and retrieval. The observations show that data marks are optical invisible or completely covered with numerous micro-bubbles. These test results demonstrate that secure and complete destruction of data on optical discs is achieved using an ODD system. Successful destruction, however, depends greatly on exposure conditions and the type of optical media.

1 INTRODUCTION

1.1 Basic description of research

Optical data storage is a dominant technology for audio, video and multimedia distribution, as well as computer software, since the advent of compact discs (CD) in 1983. Recently, researchers developed Digital Versatile Discs (DVD), High-Definition DVD (HD-DVD) and Blu-ray Discs (BD) to satisfy the consumer demand for higher storage capacity and data transfer rate and have been making efforts to develop next-generation optical storage technologies. As optical media are widely used in one's daily life, the secure disposal of the data stored on the media has become an issue. This dissertation is focused on the study of optical destruction techniques of data in optical storage media.

For the data destruction study, an engineering tool that uses a high power laser beam is introduced. An intense line beam that scans over data changes the optical and topological properties of data marks and their surrounding layers such as a polycarbonate substrate and a reflective layer, making data marks unreadable and unrecoverable even using a microscope technique [Kasanavesi *et al.* 2004]. Such an optical data destruction (ODD) system using a high power laser beam and a novel focus sensor compatible with the intense line beam is designed and built to be used in a number of destruction experiments on various CD formats such as CD read-only memory (CD-ROM), CD-Recordable (CD-R), and CD-ReWritable (CD-RW). In the course of investigation, several interesting results are obtained, such as a new understanding of designing optical

systems with a high power laser diode (HPLD), development of a new type of focus servo system, and understanding changes in physical data marks and surrounding layers upon high power exposure.

1.2 Motivation for this study

Secure disposal of an optical disc means that no useful data can be recovered, even from a disc fragment. The definition of “secure disposal” has a lot to do with data recovery techniques and capabilities. In data disposal point of view, one may think that data are unreadable when a disc is mechanically damaged disc or broken into pieces. Although data may not be readable from a conventional disc readout system, there could be a need to retrieve information from the disc. It might be necessary to all the available or inventive methods of data recovery, regardless of time and cost. For example, Kasanavesi and his colleagues published a systematic approach to retrieve data from a broken piece of a CD by applying various signal and image processing algorithms to a series of microscopic images of data marks obtained using a high power microscope. [Kasanavesi *et al.* 2004]. In spite of the estimated total recovery time for a whole CD of 475 hours, their study shows that absolute time in pre-groove (ATIP) information, a time code that indicates the time elapsed from the beginning of a CD data signal, can be recovered with a probability of 0.5 as long as the track length in the fragment is greater than 5mm. The recovery of ATIP information from a disc fragment is meaningful in that once ATIP information is known, the physical location of the recovered data bytes from a disc fragment can be accurately determined and significant information can be retrieved by

combining data from multiple fragments. As a result, the physical dimension of contiguous data in the track direction should be smaller than 5mm to ensure secure deposit of data. Therefore, there is a need to ensure all usable data on an optical disc is destroyed, which is the primary subject of this work.

1.3 Outline of dissertation

The structure of the dissertation is as follows. In Chapter 2, the fundamentals of optical data storage are reviewed, and a Gaussian beam and a Hermite-Gaussian beam representing a laser beam are examined. Also, Chapter 2 presents studies on the optical characteristics of a beam emitted from an HPLD and investigates different methods for modeling an optical system using an HPLD. In Chapter 3, essential components of an ODD system, including a light source and a focus sensor, and how they are chosen over other candidates are discussed. In Chapter 4, optical characteristics of an HPLD beam such as spectrally-resolved lateral modes, optical spectra and coherence at different current levels are investigated. Also, a few methods of modeling an HPLD beam in an optical system are examined and their pros and cons are presented. Chapter 5 provides design of the DOE focus sensor and fabrication of the DOE. Chapter 6 explains the design aspects of an ODD system, including its functionality and optical characteristics. An optical model of the ODD system is set up using a geometrical raytracing method, and its performance is estimated from the simulated focus error signal (FES). In addition, the assembly of a prototype ODD system is described, as well as thermal and mechanical issues with the system. Chapter 7 presents a study on the physical and topological change

in the structures of CD-R discs when exposed to a high power laser beam. The results of further destruction tests on various optical media using the prototype ODD system are provided in Chapter 8.

This dissertation concludes with a review of the accomplishments and future directions in the development of ODD systems in Chapter 9. In addition, Appendix I explains a glossary of acronyms and abbreviations, and Appendix II provides the graphical representation of the control program for the ODD system. A paper published in the journal *Optical Engineering* is presented in Appendix III.

2 BACKGROUND

This chapter reviews background on topics that are needed to understand optical data destruction (ODD) techniques and to design and implement an ODD system. Firstly, optical data storage technology is examined, including basic principles, light sources, storage media and formats for different technologies, servo techniques and performance parameters. Secondly, the fundamentals of Gaussian beams and Hermite-Gaussian beams are reviewed, and the propagation property of an astigmatic beam is described using Gaussian beam optics. Thirdly, information about a high-power laser diode (HPLD) is presented. The definition and common applications of a HPLD are provided. Optical characteristics are listed, including the near- and far-field distributions, lateral modes and their influences on beam divergence angles and spatial coherence, and astigmatism. Finally, several potential methods for modeling HPLD optical systems are reviewed.

2.1 Optical data storage

Optical data storage is found around us in the forms of Compact Discs (CDs), Digital Versatile Discs (DVDs), MiniDiscs and so on. Since the advent of CD technology, it has been prosperous as a means of computer software and multimedia distribution due to its distinct features, such as removability of the storage medium and low production cost of discs. Moreover, recently introduced DVD and Blu-ray technologies enable users to store more information and access it faster than CD technology, as illustrated in Fig. 2.1 and compared in Table 2.1. Further increase in data capacity and data transfer rate is

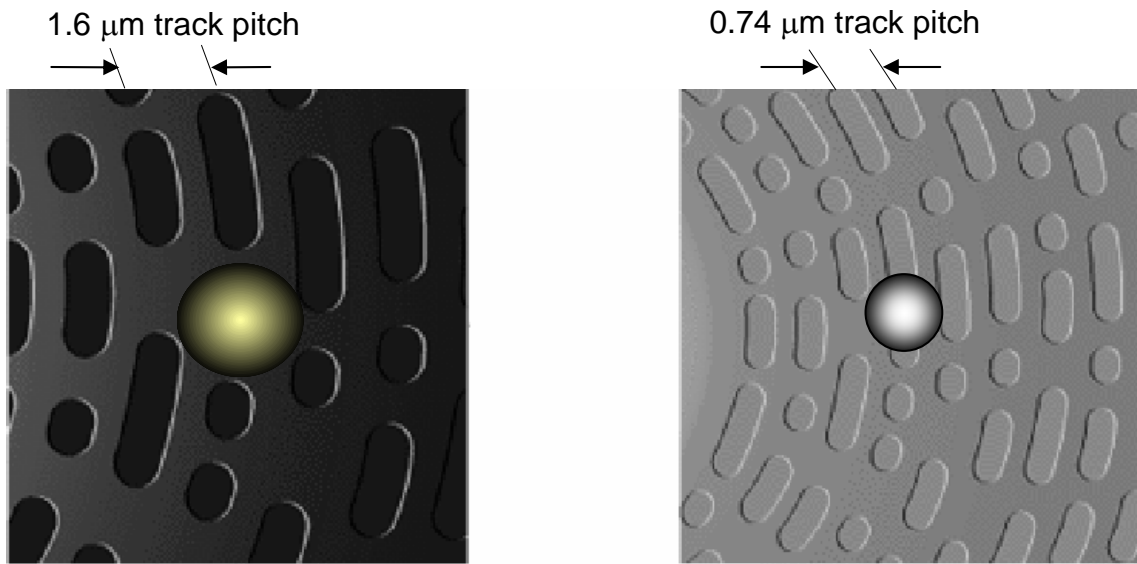


Figure 2.1 Small sections of a compact disc (CD) and a digital versatile disc (DVD) are displayed relative to the laser spots that are focused onto them during recording and readout.

Table 2.1 Comparison of CD, DVD and BD technologies. (All specs are for a single-sided single layer disc)

	CD	DVD	HD-DVD	BD
Wavelength	780 nm	650 nm	405 nm	405 nm
Numerical aperture	0.45	0.6	0.65	0.85
Track pitch	1.6 μm	0.74 μm	0.4 μm	0.32 μm
Protection layer	1.2 mm	0.6 mm	0.6 mm	0.1 mm
Min. length pit	0.83 μm	0.4 μm	0.204 μm	0.15 μm
Data transfer rate	1.38 Mbits/sec	11.08 Mbits/sec	36Mbits/sec	36 Mbits/sec
Capacity	0.74 GB	4.7 GB	15 GB	25 GB

indispensable for the next-generation optical data storage technology. Note that technical facts in this section are based on a few books on optical data storage [Marchant 1990, Milster 2004].

2.1.1 Principles of optical data storage

Optical data storage systems use light to write and read information. The digital information is recorded on and retrieved from optical discs using tightly focused laser light. The processes of recording and retrieving data are schematically shown in Figs. 2.2 and 2.3, respectively. In the recording process, digital data are encoded and modulated into a data stream that is used as a drive signal for a laser diode (LD). The modulated light emitted from the LD is focused onto an optical disc through illumination optics. The focused light beam heats the storage medium and changes its reflective properties, resulting in a data mark. As the disc rotates, data marks are produced in spiral tracks around the center of the disc. In case of prerecorded discs, data marks are generated in the form of pits on a master disc, and replicas are inexpensively made by injection molding in a few seconds.

In the readout process, the laser is operated at a low constant output power level in order not to change the reflection property of the medium. After passing the beam splitter, the laser beam is focused onto the disc and modulated upon reflection as the recorded data marks pass under the focused beam spot. The modulated light is directed to detectors through servo and data optics and converted to electrical signals by amplifiers and decoders.

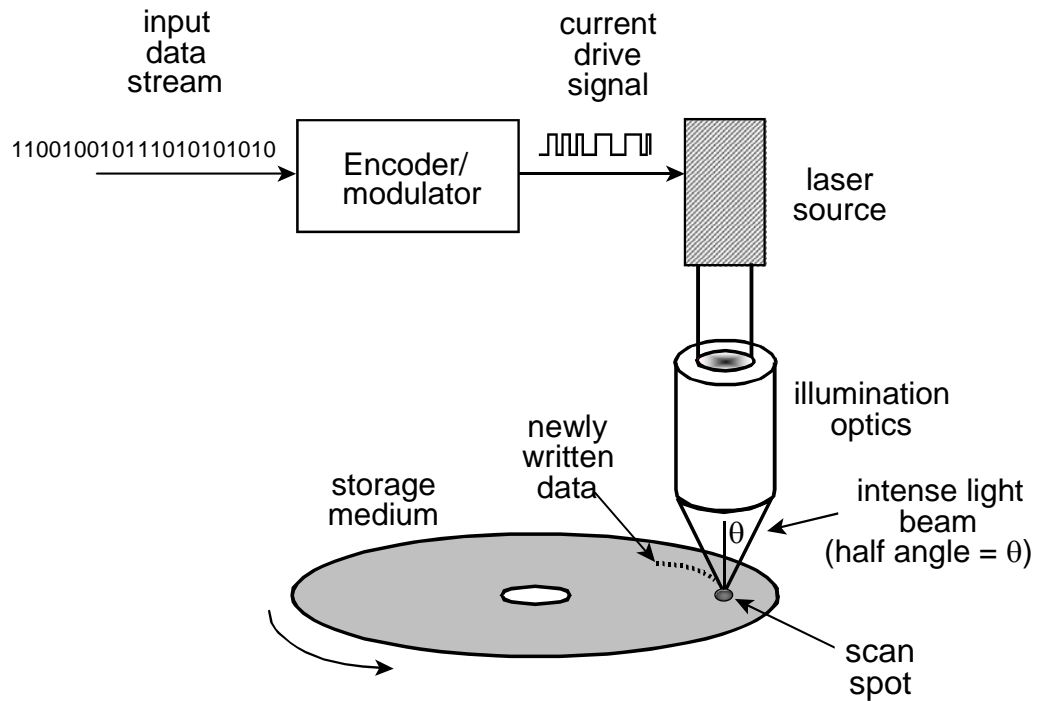


Figure 2.2 Optical recording. The process of recording data onto an optical disc starts with the user input data stream converted to a current drive signal for the laser diode. Intense pulses from the laser cause physical changes in the surface of the recording medium as the disc spins, which result in spiral tracks of data marks.

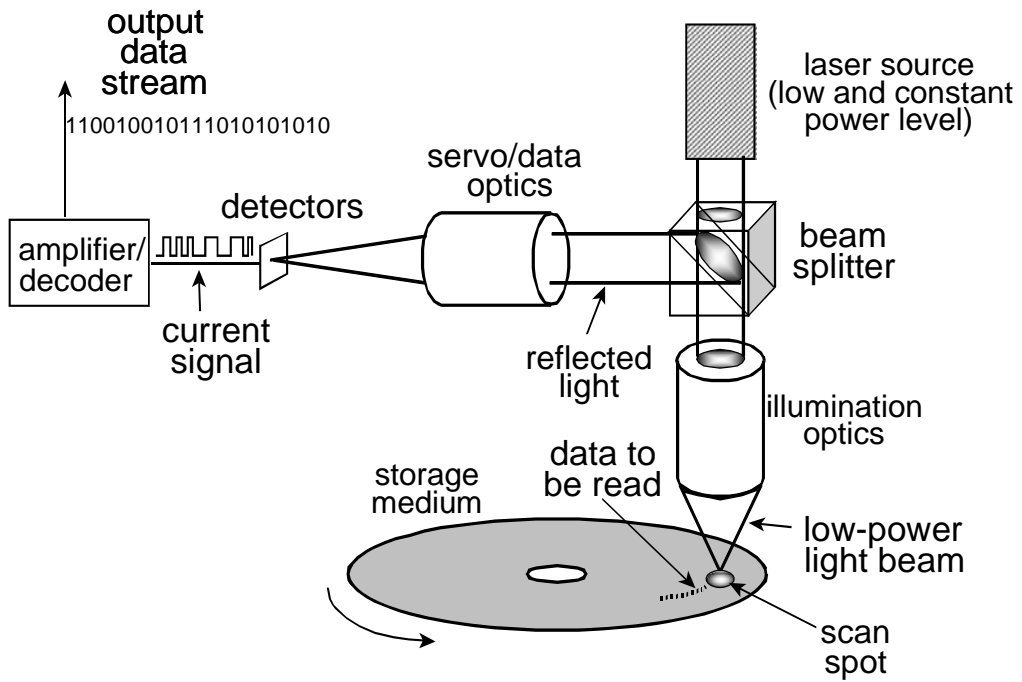


Figure 2.3 Optical retrieval. A constant, low power laser beam scans a data track to readout data from the disc. Reflected light, which is modulated by the data mark pattern, causes modulation in the reflected light. The reflected light is directed to servo and data detectors with a beam splitter, which convert the light modulation in a current signal that is then decoded.

2.1.2 Light source and optical beam spot

The capacity of an optical storage system depends on the size of the focused beam spot on a disc that is used to write and read information. Obviously, the smaller the spot size, the more information can be written and read. Due to diffraction effects caused by the wave nature of light, however, the focused spot can not be infinitely small. The size of the focused spot approximately follows the Airy pattern, if we assume that a coherent, collimated light illuminates the lens [Marchant 1990]. The full-width-at- $1/e^2$ (FW1/e²)

spot diameter is obtained using the Airy disk equation, appropriately scaled for a $1/e^2$ irradiance filling the stop of the lens,

$$s = \lambda / NA , \quad (2.1)$$

where λ is the wavelength of the light and NA is the numerical aperture of the system. For CD, $s = 1.73 \mu\text{m}$, and, for DVD, $s = 1.08 \mu\text{m}$. So, shorter wavelengths and larger NAs are, produce smaller spot sizes. As a result of reduced sizes of data marks, more data can be recorded on the same size disc. However, it is desirable to decrease the wavelength rather than to increase NA in order to increase data capacity, because the depth of focus is proportional to $\frac{\lambda}{(NA)^2}$ and sensitivities to the aberrations such as coma and spherical aberration increase with the third and fourth power of NA , respectively [Born and Wolf 1999]. In practice, λ is reduced and NA is increased for successive generations of optical discs. The wavelengths of LDs in CD and DVD systems are 780nm and 650nm, respectively. BD systems use shorter-wavelength (405nm) LDs.

Light sources used in optical data storage are semiconductor laser diodes, due to their compactness and low cost. They are also capable of direct modulation of electric current signals with no need of costly and bulky external modulators. They are required to emit a few milliwatts for read-only systems and several tens of milliwatts for recording systems. As far as their spectral behavior is concerned, spatial coherence and single transverse-mode operation is required, although several longitudinal modes are practically acceptable.

2.1.3 Storage media and various formats of optical data storage technology

An optical disc is composed of a substrate, a storage layer, a reflector, a protective lacquer and a label, as shown in Fig. 2.4. The laser beam is focused deep inside the disc after passing a transparent substrate that is 1.2 mm thick for CD, 0.6 mm thick for DVD and 0.1 mm thick for BD. The focused beam reads data marks on the storage layer that is coated with a reflecting material, such as aluminum, silver or gold. The reflector is coated with a lacquer for the purpose of protecting data on the storage layer. Finally, a label is printed onto the lacquer. It is noteworthy that the main role of the substrate is to minimize the adverse effects of dust, fingerprints and scratches on data readout or recording performance by keeping them out of focus.

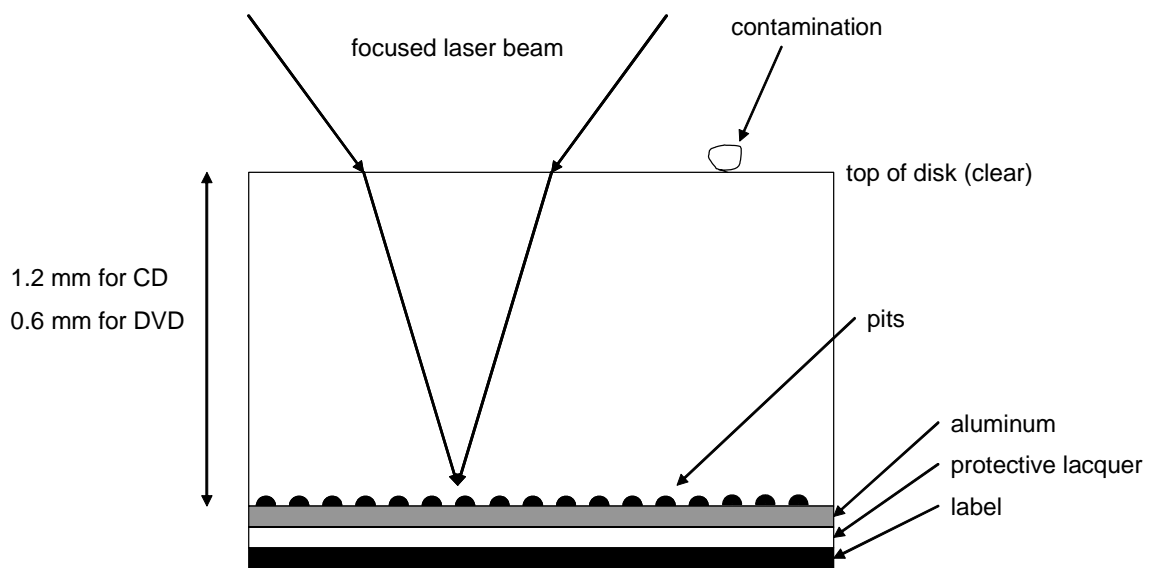


Figure 2.4 An optical disc is used so that the focusing laser light is passed through the clear side of the substrate and illuminates the data-mark pattern on the other side. The thickness of the cover layer is designed to reduce effects of contamination on the surface of the disc, like dust or fingerprints.

These types of commercially available optical discs are associated with the formats of optical storage technology:

- 1) CD- or DVD-ROM (read-only memory);
- 2) CD-, DVD- or DVD+R (recordable); and
- 3) CD-, DVD- or DVD+RW (rewritable).

Prerecorded discs in CD- or DVD-ROM format have a series of pits in spiral tracks on a flat storage layer. When the beam spot scans a pit, the focused light is scattered away, so that the amount of light collected by an objective lens is significantly reduced compared to when the spot is focused on a flat surface of the track between pits. By sensing the amount of the reflected light, data are retrieved. The diameter of the spot is larger than the width of the pits. A simple explanation for the reduction of the reflected light in the presence of pits is that the optical path difference between the portion of the spot over a pit and the portion of the spot over a flat area gives rise to destructive interference when the effective depth of the pit is a quarter of the laser wavelength. In practice, the pit depth is designed to provide good tracking signals as well as high data signal contrast, so the effective depth of the pit is commonly $3/16\lambda$.

CD-R discs use organic films, like dye-polymer or dye-monomer, as a storage medium. Due to the low thermal conductivity of the dye material, a tightly-focused high-power laser light increases its temperature rapidly and heats the material to the point that it flows to form a pit. The destructive recording process in CD-R discs prohibits users to erase and rewrite data marks. They can be used to write once and read many (WORM) times.

CD-RW products enable users to write, erase and rewrite data marks as many as 1000 times using phase-change technology. A high-power laser beam changes the state of the storage material into either a crystalline or amorphous state, opposite to the previous state of the material. Data marks formed under the beam spot have different reflectivity from the unexposed areas, so the readout optics can sense the reflectivity changes in the presence of the marks. A constant and intermediate-power laser beam returns the material state of data marks to a blank crystalline state in the erasure process. Then, new data patterns can be written on the medium. Because this phase-change process involves some mechanical deformation of the material, there is a limitation in the number of overwriting cycles due to stress fractures. In addition to their over-writable feature, CD-RW discs include a few dielectric thin-film layers around the storage layer. The layer thicknesses are carefully designed to tune the reflective properties for maximum signal contrast and to absorb the adequate amount of laser power for writing.

2.1.4 Focus and tracking servo systems

The size of a beam spot on a storage medium is very small. Its FW1/e² diameters in CD and DVD are about 1.7 μm and 1.0 μm, respectively. However, as the disc spins, the position of the beam spot moves in and out of focus as much as ±50 μm due to warping in discs or disc tilt when mounted in a drive. Also, it can wobble in the cross-track direction as much as ±100 μm when there are fabrication errors or disc eccentricities caused by mounting errors, thermal expansion of the substrate and so on. During operation, a focused beam spot can not be at the right place at all times without a

corrective mechanism. Therefore, an optical storage system must have a means to maintain the beam spot focused and centered on the track of the recording layer. In practice, the spot position is sensed by the same optical beam used for recording and reading. The position is controlled by feedback mechanisms combined with a voice coil actuator in which the objective lens is mounted. The actuator performs both focusing and track following by moving the objective lens in the axial and radial directions, respectively. The amount of its movement is determined from feedback error signals that are obtained with separate focus and tracking feedback sensors. Among many focus and track-following schemes, one popular focusing method (astigmatic) and two widely-used tracking methods (push-pull and three-spot) are explained in this section.

The astigmatic focus sensor used in many practical devices is shown in Fig. 2.5. The light reflected from the disc is directed toward the servo optics astigmatic lens, which generates a nearly circular spot on the detector when the disc is in focus and an elongated spot when the disc is out of focus. So, when the disc is in focus, the symmetric light spot on the detector plane produces a zero focus error signal, $FES = (A+C)-(B+D)$, because the four quadrants receive an equal amount of light. However, when the disc is out of focus, the convergent or divergent returning beam gives rise to an elongated spot on the quad-detector along the left or right diagonals. In this case, the FES is no longer zero and varies linearly with a small amount of defocus. The actuator moves the objective lens in the axial direction, according to the amplitude and sign of the FES in a closed-loop feedback servo, so that the beam is constantly kept in focus.

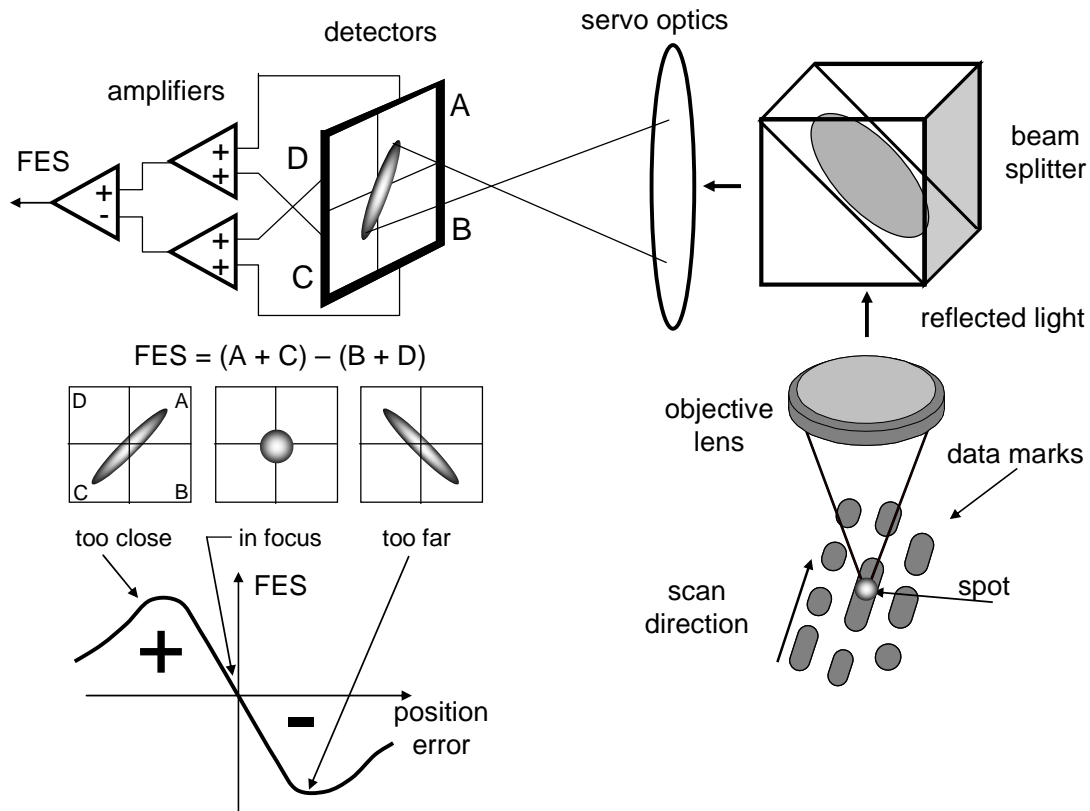


Figure 2.5 The astigmatic focusing technique uses a special lens in the servo optics before a quadrant-cell detector. The servo optics lens introduces a small amount of astigmatism into the beam along a diagonal direction on the detector. As the spinning disc goes into and out of focus, the astigmatism forces the light spot to change shape. A difference signal from the detector quadrants produces an FES that indicates the amount of defocus.

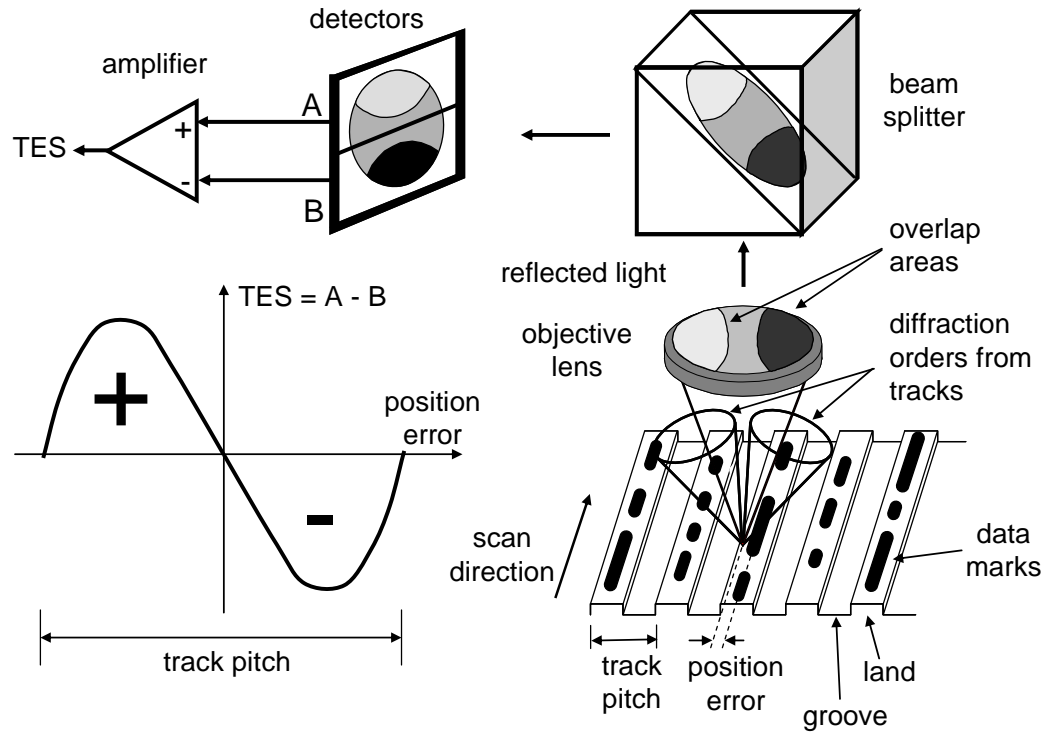


Figure 2.6 The push-pull tracking error signal (TES) is generated by using a split-cell servo detector and sensing the difference in light level between the cells. Since grooves of the disc diffract light like a grating, diffracted orders overlap and generate an interference pattern. As the laser spot moves off track, the relative phase change in the diffracted orders produces bright and dark patterns on the detector. The TES difference signal indicates the relative off-track location of the laser spot.

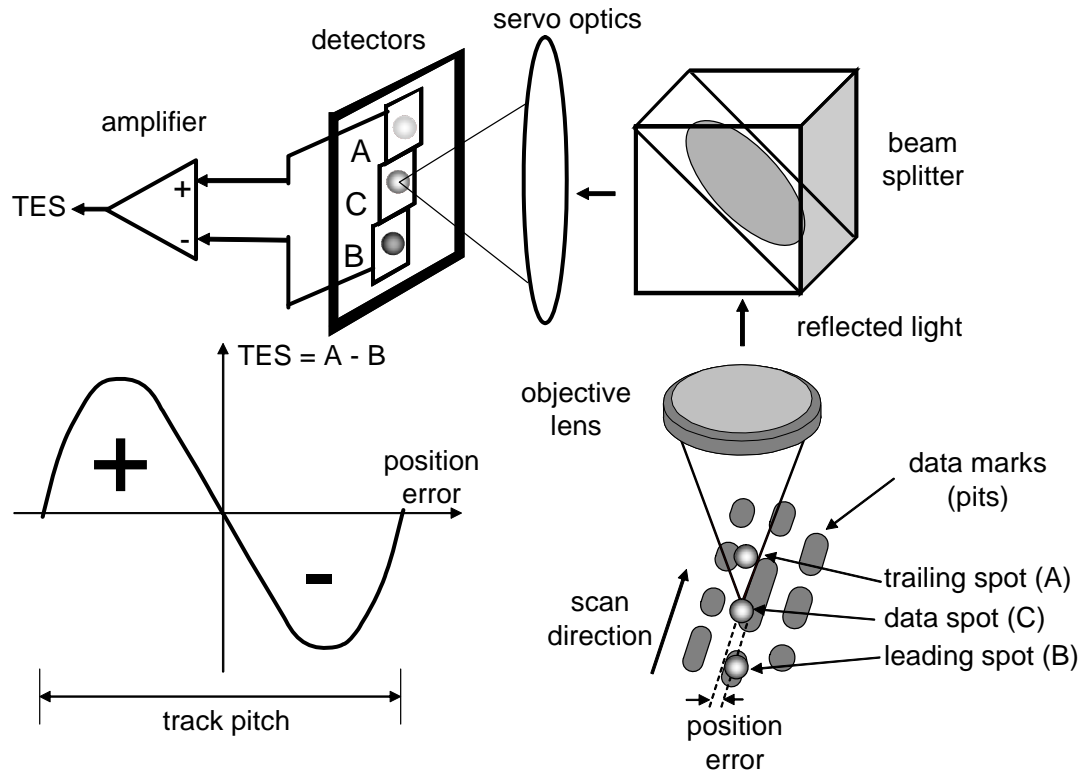


Figure 2.7 The three-spot tracking sensor uses two auxiliary laser spots that ride edges of the track as the disc spins. The spot are reimaged onto separate detector elements. If the data track is not centered, the amount of light reflected from each auxiliary spot changes. One detector spot becomes brighter, and the other dims. A difference signal produces a reliable TES.

The push-pull tracking method, as illustrated in Fig. 2.6, makes use of the grooves that exist on writable media, like CD-R and CD-RW, as a tracking reference for data recording. The grooves and lands comprise a grating structure and give rise to diffraction when the light is reflected from the recording layer. The phase of the diffracted orders varies with the position of the optical beam spot on a track, and their phase difference determines the brightness of each overlapped area on the exit pupil. When the focused spot is centered on the land, the phase of each diffracted order is equal, and the overlap areas are of equal brightness. The baseball-looking pattern is directed to a bi-cell detector and, in the centered case, produces a zero tracking error signal ($TES = A-B$). On the other hand, when the spot moves away from the center of the land, the phases of the diffraction orders change, and the brightnesses of the overlap areas become unbalanced. Therefore, the unbalanced baseball pattern on the detector gives rise to a non-zero TES. The TES is a linear function of the position error near the center of the track; otherwise, it is a sinusoidal function. The amount and the direction of the servo-loop-controlled lens movement depends on the amplitude and the sign of the TES.

In read-only media, such as CD and CD-ROM, the three-spot tracking method is widely used, since it can give a direct indication of the spot position on a track without need for a land-groove pattern. Figure 2.7 shows the schematic of this tracking sensor. The laser beam is divided into three beams through a weak phase grating positioned between the laser diode and the beam splitter. One beam is the central beam used to read data, while the other two beams are focused right before and after the central beam spot and are used to detect tracking errors. Due to the alignment of the grating with respect to

the track direction, the two secondary beam spots are slightly displaced from the central spot in opposite directions. With the central spot centered over a track, the secondary beams reflect the same amount of light, and the corresponding signals on detectors A and B are equal. Since the error signal for the servo loop is the difference of the detector signals, the TES becomes zero. If the central spot moves away from its desired position, the signal level from one of the secondary beams is increased, and the signal level from the other is decreased, resulting in a non-zero TES.

2.1.5 Performance

The performance of optical data storage devices is characterized by the three important parameters *capacity*, *data rate* and *access time*. The definitions of the parameters are given below.

- *Capacity* is the maximum amount of data that can be stored on a single disc and specified in terms of mega-bytes (MB) or giga-bytes (GB), where one byte is eight bits.
- *Data rate* is the number of bits per second that are recorded or retrieved from a device during transfer of a large data block and usually specified in terms of megabits-per-second (Mbps).
- *Access time* is the latency experienced between the moment a request is made to access data and the moment the data start flowing through the communication channel and is usually specified in terms of milliseconds.

In order for more data bits to be stored on a disc, the size of a focused beam spot should be as small as possible. A small spot size can be achieved by using a short-wavelength laser diode or a high- NA objective lens, as discussed in Section 2.1.2. Also, capacity can be increased by recording data on multiple layers or both sides of a disc.

One apparent way to increase data rate is to increase the disc rotation speed, although there exists mechanical limitations for the rotation speed. Another way is to use more than one laser beam at a time. Multiple beams generated with a diffraction grating can be used to read multiple tracks simultaneously, so that more data can be retrieved at a given time [Alon and Kosoburd 2002]. Further investigation into multiple beam systems are described in Section 2.2. Data rate is sometimes described as the data-rate speedup factor relative to a known standard, such as “1×” or “40×”. The 1× rate is the data rate, given in original manufacturer specifications, while 40× refers to a data rate forty times faster than the 1× rate.

The access time is determined by the mechanical latency due to the disc rotation and actuator seek time required to move to a particular track. The highest latency is the time it takes the disc to make one revolution. Reduction of latency requires spinning the disc faster.

2.2 Gaussian beams and Hermite-Gaussian beams

A common laser beam is governed by the well-known wave equation, and a set of Hermite-Gaussian functions is one of its solutions [Siegman 1986]. Hermite-Gaussian functions describe the physical properties of laser beams in a simple analytic form. In this

section, a Gaussian beam that is the lowest-order Hermite-Gaussian mode is reviewed, and then the fundamentals of Hermite-Gaussian beams are provided.

2.2.1 Gaussian beam

A Gaussian beam has a simple analytic form describing an ideal single-mode laser beam.

The transverse Gaussian irradiance with the beam waist located at $z = 0$ is expressed as

$$I(r, z) = \frac{2w_o^2}{\pi w^2(z)} e^{-2\frac{r^2}{w^2(z)}} , \quad (2.2)$$

where w_o is the beam waist radius, $w(z)$ is the beam radius at z (called beam width in the following) and r is the radial position in the transverse plane. The main parameters that determine the propagation property of a Gaussian beam are the beam waist radius w_o , the waist position, and the wavelength of the beam, λ . The beam width and the radius of curvature of the wavefront at any transverse plane can be calculated in terms of w_o and the ratio (z_R / z) , where $z_R = \pi w_o^2 / \lambda$ is referred to as the Rayleigh range. The beam width at z is

$$w(z) = w_o \sqrt{1 + \left(\frac{z}{z_R}\right)^2} , \quad (2.3)$$

and the radius of curvature at z is

$$R(z) = z \left[1 + \left(\frac{z_R}{z} \right)^2 \right] . \quad (2.5)$$

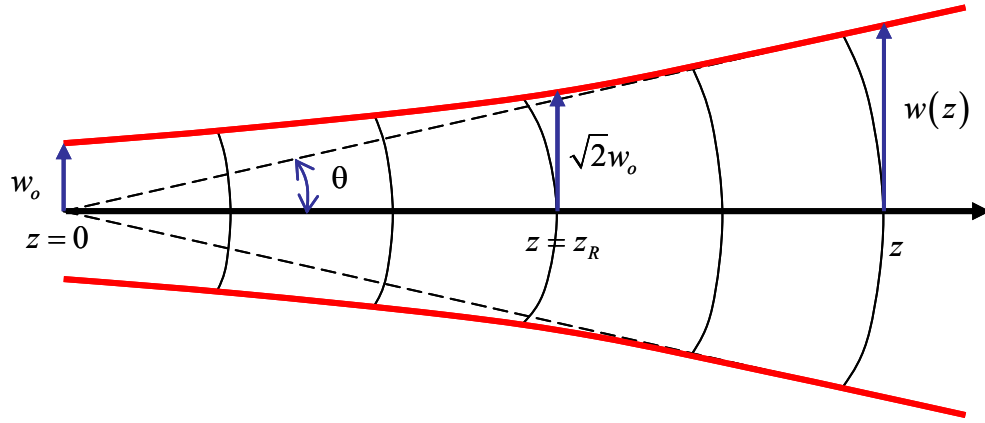


Figure 2.8 Evolution of a Gaussian beam

The evolution of a Gaussian beam along the propagation direction is illustrated in Fig 2.8. At the beam waist ($z = 0$), the beam has the smallest beam width and infinite radius of curvature (planar wavefront). As it propagates away from the waist, the beam width increases and the wavefront becomes more curved. At $z = z_R$, the beam width increases to $\sqrt{2}w_o$. This Rayleigh range provides an approximate boundary between “near-field” and “far-field” from the beam waist, and $2z_R$ is used as the collimated beam distance or the depth of focus [Siegman 1986]. Beyond the Rayleigh range, the far-field beam diverges at half-angle of $\theta = w(z)/z \approx \lambda/(\pi w_o)$ as if it is a spherical wave originating from a point source at $z = 0$. Due to diffraction, small w_o and large λ imply short Rayleigh range and a rapid Gaussian beam divergence from the waist. It is noteworthy that the Gaussian beam remains Gaussian when propagating in freespace or in an isotropic and homogeneous medium.

In focusing a Gaussian beam or imaging a Gaussian waist using a lens, there is a focal shift toward the lens. A lens formula for a Gaussian beam can help predicting the

waist location after the lens [Self 1983]. That is,

$$\frac{z'}{f} = 1 + \frac{\frac{z}{f} - 1}{\left(\frac{z}{f} - 1\right)^2 + \left(\frac{z_R}{f}\right)^2}, \quad (2.5)$$

where f is the lens focal length, and z and z' are the object and image distances from the lens, respectively. The object and image distances normalized by f are plotted for several values of a parameter z_R/f in Fig. 2.9.

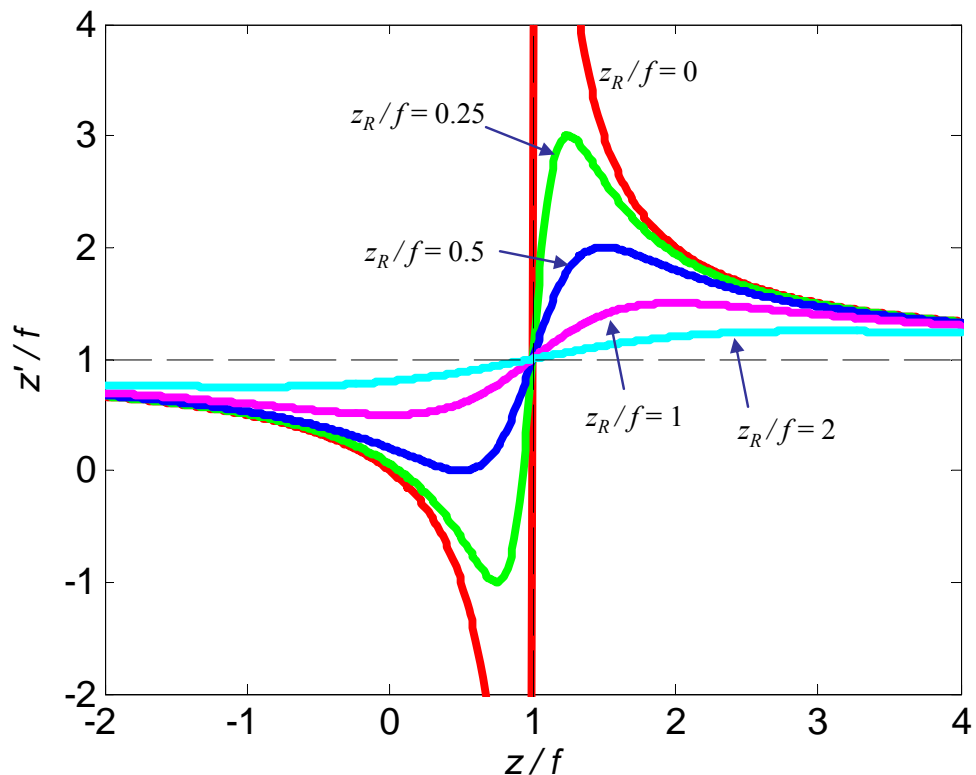


Figure 2.9 Plot of the lens formula for a lowest-order Gaussian beam. The object and image distances normalized by f are plotted for several values of a parameter ($z_R/f = 0, 0.25, 0.5, 1, 2$).

The distinguishing features of Gaussian beam imaging from the geometrical imaging are that:

- 1) The image waist location moves closer to the lens as the ratio z_R/f increases (except for the case where $z \neq f$) ;
- 2) The image waist is located at the back focal plane regardless of z_R/f when $z = f$; and
- 3) The maximum image distance is $\left(\frac{z'}{f}\right)_{max} = 1 + \frac{z_R}{2f}$ and occurs at $z = f + z_R$.

These features are especially useful in understanding the different behavior in two orthogonal axes of a transverse plane of an astigmatic Gaussian beam propagating through an optical system. Due to the different waist radii of an astigmatic beam, the radii of curvature and the Rayleigh ranges in x and y axes are different, resulting in different beam divergences in the two axes. Interestingly, when both waists of an astigmatic beam are located in the same plane and imaged by a lens, the emerging waists after the lens occur in different locations, according to Eq. (2.5). When the astigmatic beam passes through a second lens, the waist locations become dependent upon the position of the second lens with respect to the first lens, as well as the radii of the emerging waists after the first lens. This effect will be further discussed in Chapter 4.

2.2.2 Hermite-Gaussian beams

A Gaussian beam, previously discussed, is the lowest-order Hermite-Gaussian beam. In general, Hermite-Gaussian functions can be used to illustrate the physical properties of

both a single-mode laser and a multi-transverse-mode laser.

Assuming the Hermite-Gaussian functions are separable in x and y axes, the Hermite-Gaussian beam is expressed as

$$E(x, y, z) = E_0 \frac{w_o}{w(z)} H_p\left(\frac{\sqrt{2}x}{w(z)}\right) H_q\left(\frac{\sqrt{2}y}{w(z)}\right) e^{-\frac{x^2+y^2}{w^2(z)}} e^{-jk\frac{x^2+y^2}{2R(z)}} e^{-j[kz-(1+m+n)\tan^{-1}\left(\frac{z}{z_R}\right)]}, \quad (2.6)$$

where w_o , $w(z)$, $R(z)$ and z_R are the same as for the lowest-order Gaussian mode,

and $k = \frac{2\pi}{\lambda}$ is a wave number. H_p and H_q are the Hermite polynomials of order p and q ,

which follow from the recursion relation,

$$H_{p+1}(x) = 2x H_p(x) - 2m H_{p-1}(x), \quad (2.7)$$

and, similarly, for q . Some Hermite polynomials with low order are provided in Table 2.2.

The first exponential term in Eq. (2.6) is related to the transverse field amplitude, the second exponential shows the transverse phase and the last exponential describes the

Table 2.2 Several low-order Hermite polynomials

Order, p	Hermite polynomial, $H_p(x)$
0	1
1	$2x$
2	$4x^2 - 2$
3	$8x^3 - 12x$
4	$16x^4 - 48x^2 + 12$

phase evolution along the propagation direction. Since all modes share the same $R(z)$, the wavefront curvature propagates in the same manner. However, the longitudinal phase varies with increasing mode number, which implies that higher-order modes advance lower-order modes in phase.

The transverse irradiance is expressed as

$$I(x, y, z) = I_0 \frac{w_o^2}{w^2(z)} H_p^2 \left(\frac{\sqrt{2}x}{w(z)} \right) H_q^2 \left(\frac{\sqrt{2}y}{w(z)} \right) e^{-2\frac{x^2+y^2}{w^2(z)}} . \quad (2.8)$$

Several Hermite-Gaussian modes are simulated and their transverse irradiances are presented in grayscale in Fig. 2.10(a). In comparison, the lasing transverse modes from a CO₂ laser that appears in the literature are shown in Fig. 2.10(b) [Kogelnik 1967]. Transverse modes of the CO₂ laser are in good agreement with the simulated Hermite-Gaussian modes.

Equations (2.6) and (2.8) can be used for a Hermite-Gaussian beam with the same waist radii in x and y axes. When the radii are different for an astigmatic beam, the Hermite-Gaussian beam irradiance is expressed as

$$I(x, y, z) = I_0 \frac{w_{ox} w_{oy}}{w_x(z) w_y(z)} H_p^2 \left(\frac{\sqrt{2}x}{w_x(z)} \right) H_q^2 \left(\frac{\sqrt{2}y}{w_y(z)} \right) e^{-2\left[\frac{x^2}{w_x^2(z)} + \frac{y^2}{w_y^2(z)} \right]} , \quad (2.9)$$

where w_{ox} , w_{oy} are the beam waist radii in x and y axes, and $w_x(z)$, $w_y(z)$ are the beam widths in x and y axes.

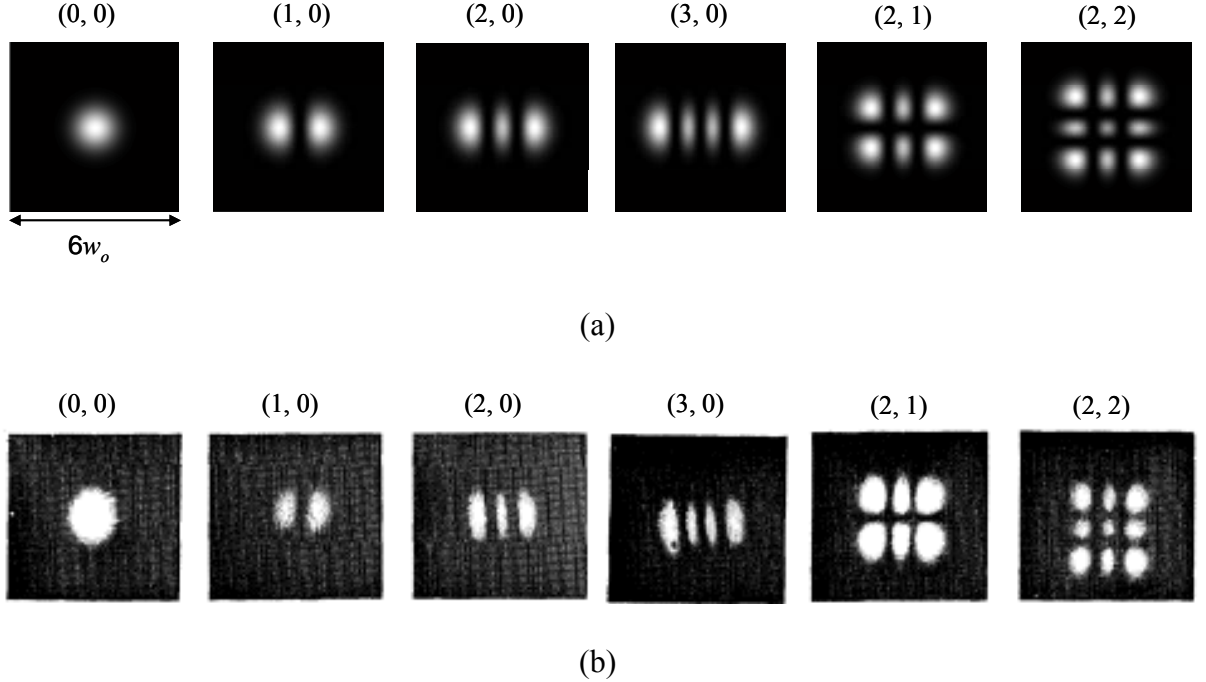


Figure 2.10 (a) Simulated 2-D Hermite-Gaussian modes and (b) transverse modes of a CO₂ laser observed in [Kogelnik 1967]. In (a), transverse irradiances simulated over the $6w_o \times 6w_o$ area. The mode numbers (p, q) are presented on top of the corresponding modes.

2.3 High-power laser diode (HPLD)

2.3.1 Introduction

An LD is composed of an active layer, surrounding cladding and substrate layers, as schematically drawn in Fig. 2.11(a). Electric current applied to the stripe electrode flows through the active layer to the substrate to ground. The injected current generates a population inversion of carrier densities within the active layer underneath the stripe, resulting in optical gain. Light amplification occurs in the active layer as stimulated photons are reflected back and forth off the two cleaved facets, which form a cavity.

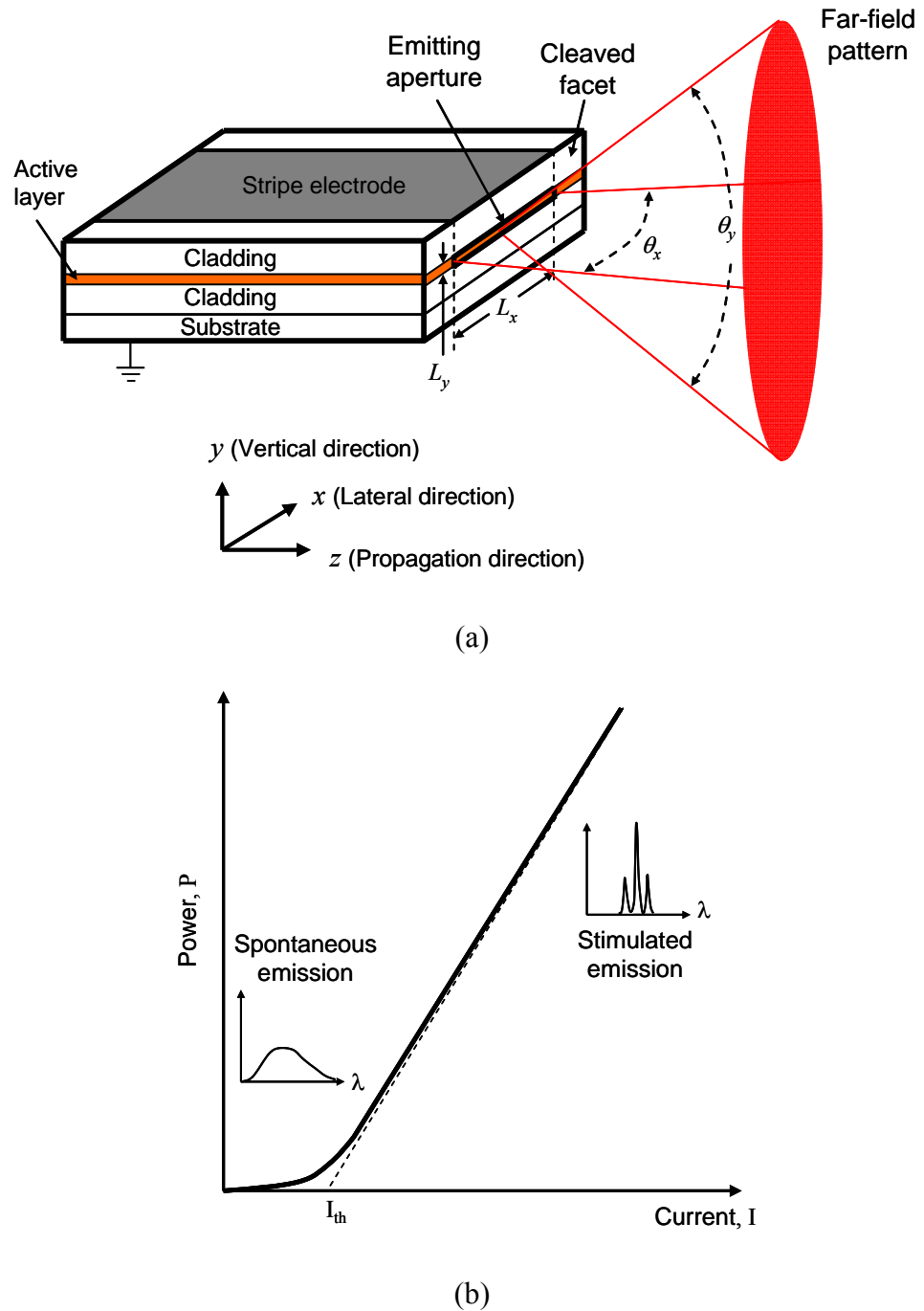


Figure 2.11 (a) Geometry of an LD and the emerging beam and (b) optical power vs. injection (P - I) curve along with spectra below and above the threshold current I_{th} .

Beam confinement in the y axis (perpendicular to the active layer) is achieved by the refractive index step of the active layer and the cladding layers. The lateral confinement in the x axis (parallel to the active layer) is provided by either gain-guiding or index-guiding. In gain-guided LDs, optical gain is strong beneath the stripe and decreases significantly near the stripe edges, so that the optical field remains in the region underneath the stripe. Index-guided LDs use index variation in the x axis to provide the lateral beam confinement, whose active layer outside of the stripe is selectively etched and filled with a lower-index material.

The output optical power from an LD is schematically drawn as a function of the injection current in Fig. 2.11(b). Below the threshold current I_{th} , there is no lasing and the spectrum of the output beam is broad due to spontaneous emission. At $I > I_{th}$, the output power increases linearly with the current and lasing takes place with dominant modes appearing in the spectrum.

An HPLD is an LD that produces high optical power from its wide emitting aperture. The output power ranges from 100mW to several Watts, and the typical emitting aperture dimensions are $50 \sim 300\mu\text{m}$ in the lateral (x) direction and about $1\mu\text{m}$ in the vertical (y) direction.

There are increasing demands for higher optical power in many applications, including material processing and solid-state laser pumping. The maximum output power of an HPLD is limited by catastrophic optical mirror damage (COMD) on the LD facets [Moser 1991, Moser and Latta 1992]. The most common approach to produce high power without COMD is to reduce the irradiance inside the cavity by broadening the current-

supplying stripe width, which is limited up to 300 μm due to electrical and optical reasons [Bachmann 2004]. In return for high output power, such a wide-aperture cavity supports a number of lateral modes in the xz plane parallel to the active layer, which increases the far-field divergence angle and deteriorates spatial coherence of the output beam [Chang-Hasnain *et al.* 1989, Mailhot *et al.* 2000]. In some applications, such as solid state laser pumping, the degradation in spatial coherence is unacceptable. The structure of an HPLD can be modified to support only a single transverse mode by using an unstable resonator [Salzman *et al.* 1985, Mittelstein *et al.* 1985], or a tapered resonator [Kintzer *et al.* 1993]. External reflectors, such as a diffraction grating [Harvey and Myatt 1991, Pan *et al.* 1998], a phase conjugate mirror [MacCormack and Feinberg 1993, Løbel *et al.* 1998], or an anamorphic external cavity [Mailhot *et al.* 2000] are also employed to improve the spectral and/or spatial coherence. Also, use of a non-absorbing mirror at the LD output facet increases the threshold irradiance for COMD, such that higher exitant radiance can be provided from the same aperture dimensions [Lammert *et al.* 2006]. In applications where the cost per Watt of optical power is important, e.g., material processing, a monolithic laser diode bar comprising a number of HPLDs is used to produce over 100 Watts [Diehl 2000, Li 2000]. Because of significant heat produced during high-power operations, individual emitters are isolated optically and electrically from each other, and heat sinks play an important role in reliability of lifetime of the devices. For output power in the kilo-Watt range, a stack of laser diode bars is used [Li 2000].

2.3.2 Basic optical characteristics of HPLD beam

The HPLD beam emerges from a wide emitting aperture with the dimension of $L_x \times L_y$, as described in Fig. 2.11(a). The output beam has a single transverse mode in the vertical (y) direction due to the thin active layer ($L_y < 100\text{nm}$), while it has multiple transverse modes in the lateral (x) direction due to the large stripe width L_x . The presence of multiple lateral modes of an HPLD is demonstrated in literature [Chang-Hasnain *et al.*, 1989, Mailhot *et al.* 2000]. Figures 2.12(a), (b) and (c) present the HPLD lateral modes that Mailhot and his colleagues spectrally resolved using a grating spectrometer with resolution of 0.01nm . Figure 2.12(a) exhibits the spectrum of the output beam when the HPLD is operated at $I/I_{\text{th}} = 1.08$. The longitudinal modes are separated by 0.22nm and the lateral modes contained in each longitudinal mode are manifested by small spikes, some of which are indicated by numbers 0 – 3. As shown in Fig. 2.12(b), there are several longitudinal modes, each of which contains multiple lateral modes. Figure 2.12(c) shows the lateral modes belonging to one longitudinal mode at different injection current levels ($I/I_{\text{th}} = 1, 1.03, 1.17$ and 1.6). The number of lateral modes increases with the applied current, and it was observed that eleven lateral modes are lasing at the same time at $I/I_{\text{th}} = 1.6$.

The HPLD output beam at the facet is called a “near-field” pattern, and typical near-field lateral irradiance patterns of an HPLD are presented in Fig. 2.13(a) [Mailhot *et al.* 2000]. At near-threshold current, the irradiance profile is single-lobed, but the profile becomes approximately a top-hat in shape and exhibits multiple ripples at $I/I_{\text{th}} = 1.58$. The ripples indicate lasing of higher-order lateral modes.

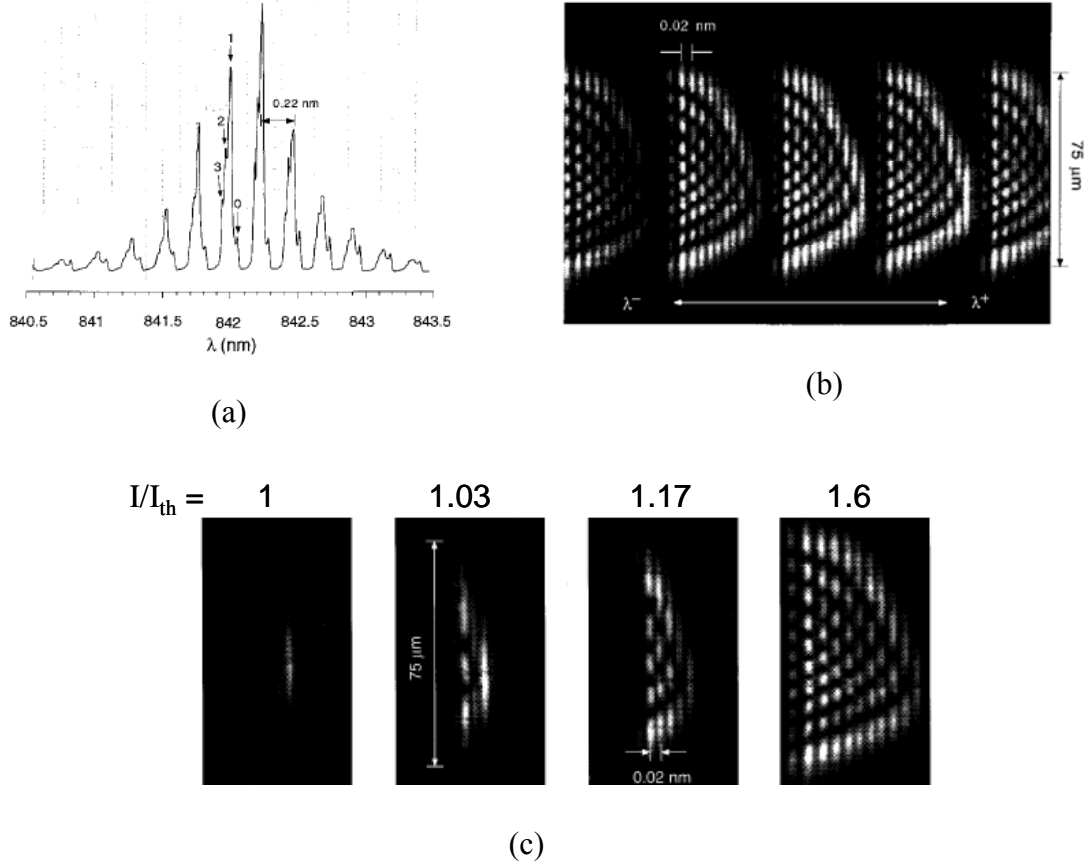


Figure 2.12 (a) Spectrum of HPLD output beam ($I/I_{\text{th}} = 1.08$), (b) image of multiple lasing modes from the HPLD operating at $I/I_{\text{th}} = 1.56$ and (c) images of lateral modes belonging to one longitudinal mode when the HPLD is operated at $I/I_{\text{th}} = 1, 1.03, 1.17$ and 1.6 [Mailhot *et al.* 2000].

Due to diffraction from the emitting aperture, the output beam in the far-field diverges fast in the vertical (y) direction (so called “fast axis”) and slow in the lateral (x) direction (also called “slow axis”), as shown in Fig. 2.11(a). The angle of divergence is usually expressed in terms of full width at its half maximum irradiance (FWHM) or FW1/e^2 . The far-field intensity distribution along the slow axis is provided in Fig. 2.13(b) [Mailhot *et al.* 2000]. As the current increases, the far-field intensity changes from a

smooth single-lobed profile to the approximate top-hat profile with multiple peaks, which is a consequence of the transition from a single-mode operation near the lasing threshold to a multi-mode operation above threshold current.

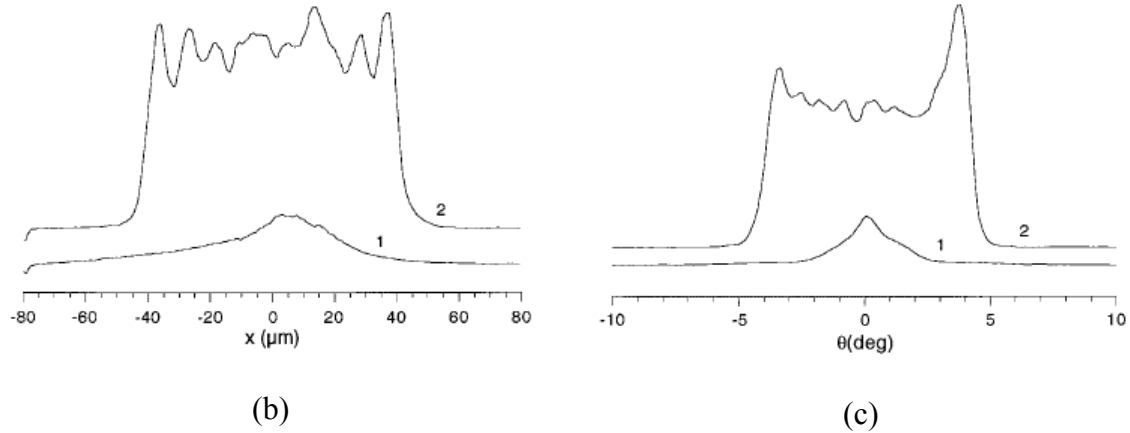


Figure 2.13 (a) Near-field irradiance profile and (b) far-field intensity profile of the HPLD output beam in the lateral (x) direction. Numbers 1 and 2 next to the curves indicate the injection current levels of $I/I_{\text{th}} = 1.02$ and 1.58, respectively [Mailhot *et al.* 2000].

Another important aspect of an HPLD beam is astigmatism. There are two different types of astigmatism in a LD: *inherent* astigmatism and *systematic* astigmatism. It was demonstrated by Cook and Nash that *inherent* astigmatism originates from the different guiding mechanisms in the directions perpendicular and parallel to the active layer [Cook and Nash 1975]. Carrier diffusion out of the stripe region gives rise to parabolic gain and refractive index profiles in a gain-guided LD, as illustrated in Fig. 2.14(a). Therefore, the output phase in the lateral (x) direction (parallel to the active layer) is cylindrical, as shown in Fig. 2.14(b), making the beam look like it originates from a point source inside the LD cavity. On the other hand, the phase in the y direction

perpendicular to the active layer (vertical direction) is nearly planar, due to strong index guiding. Therefore, the output beam has different locations for the virtual source points in the lateral (x) and vertical (y) directions. The amount of inherent astigmatism varies with different LDs and decreases with increasing current [Champagne 1995, Chernyshov *et al.* 2002].

Another type of astigmatism is *systematic* astigmatism, which results from different beam waist diameters at the output facet. Propagation through a rotationally symmetric optical system can produce systematic astigmatism if the beam has different beam widths. This systematic astigmatism in a narrow-stripe LD is negligible, due to small beam widths (typically less than $5\mu\text{m} \times 0.5\mu\text{m}$) at its facet in the lateral and vertical directions. Assuming the emitted light from such LD is a Gaussian beam, the ratios of z_R/f for both directions are negligibly small when a lens with focal length of a few mm is used to collect the light. However, it is significant in an HPLD, because of the considerable lateral beam width. For instance, typical x and y beam widths of the lowest-order modes for a HPLD are $26\mu\text{m} \times 0.5\mu\text{m}$ at the facet, which gives rise to z_R/f ratios of 0.58 and 0.0002, respectively, when a collector lens with a focal length of 4.5mm is used.

Depending on the optical system where the HPLD is used, the systematic astigmatism varies and may be a nontrivial value. Also, this significant systematic astigmatism in an HPLD beam can affect the accuracy of commonly used astigmatism measurement methods [Photon Inc. Application Note 1992, Sun 1997] if inappropriate arrangement of the measurement system is used. These measurements are made to

estimate and correct inherent astigmatism, but they may pick up systematic astigmatism unique to the measurement system, which leads to a significant error in measured inherent astigmatism.

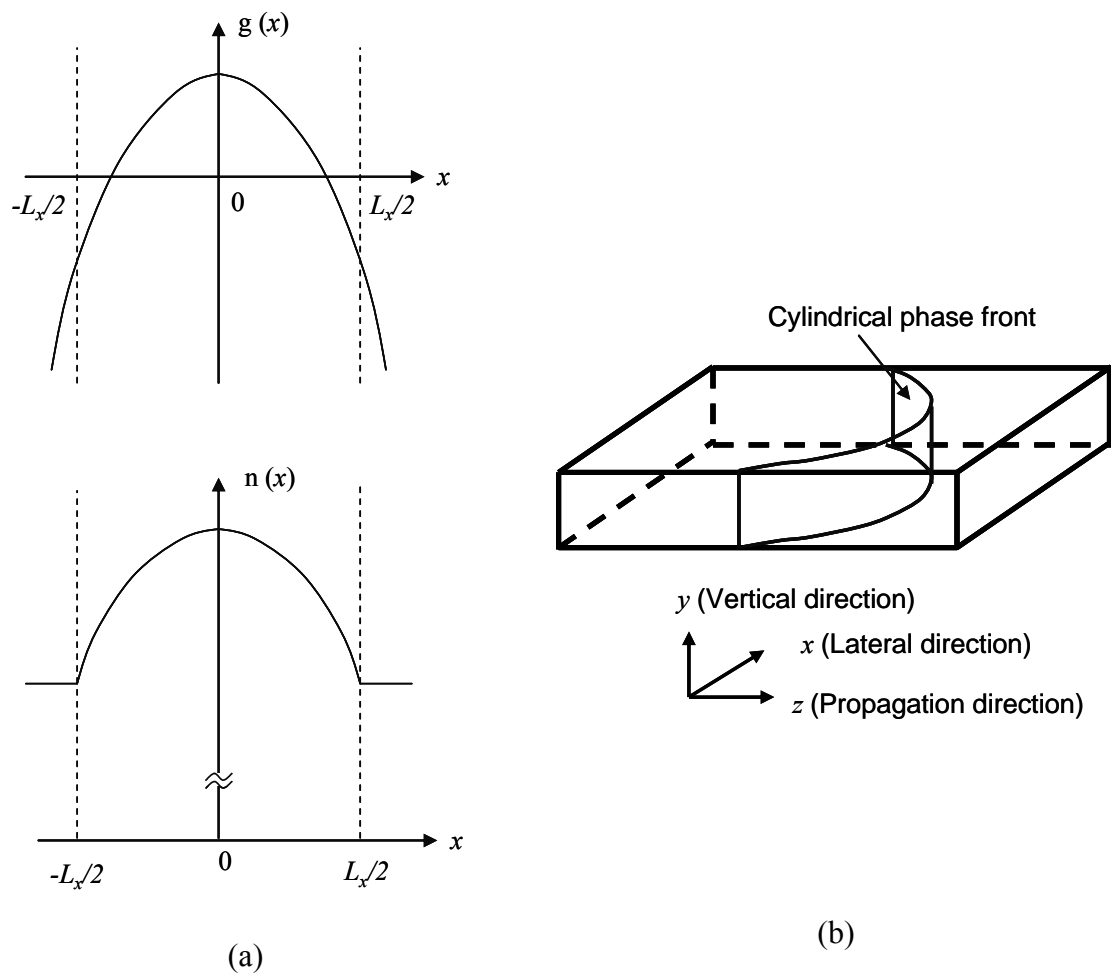


Figure 2.14 (a) Parabolic gain and refractive index profiles in the x direction parallel to the active layer. (b) Phase front propagating within an active layer. This phase front is planar in vertical (y) direction and cylindrical in the lateral direction. The emerging beam from an LD looks like it originates from a point source at the facet in the vertical (y) direction but from a point source inside the LD cavity in the lateral (x) direction, which implies inherent astigmatism.

2.3.3 Modeling methods of an optical system using a laser beam

When designing an optical system using a laser beam, the designer has several options for simulation of the system: simple paraxial raytracing, raytracing programs, Gaussian beam optics or more general physical optics propagation method. Depending on the system complexity and the desired accuracy of the model, the designer must decide which method to use. The following paragraphs introduce these methods. Chapter 4 discusses choosing a method appropriate for the ODD system.

Paraxial raytracing is based on Snell's law of refraction with some assumptions to make numerical calculation easy [Kingslake 1978, Smith 2000]. Only rays with small angles and heights, that is, paraxial to the optical axis, are considered. As the ray angles are small, the trigonometric functions in Snell's law can be replaced with ray angles. From the small height assumption, the curvature of surface can be ignored, and, instead, a flat surface with an equivalent power can be used. These simplifications allow optical system modeling to be accomplished quickly. Although paraxial raytracing is easy to implement and provides the fundamental information on an optical system, including the effective focal length, F/# and ideal locations and sizes of images and pupils, it does not take aberrations or diffraction effects into consideration. Therefore, its use is limited to aberration-free and diffraction-free systems or in an initial stage of optical system design.

More rigorous raytracing is employed in most commercial raytracing programs such as CODE V® (Optical Research Associates Inc.), OSLO® (Lambda Research Corp.) and ZEMAX® (Focus Software, Inc.). They can provide various system characteristics, including aberrations and point and optical transfer functions of the modeled optical

system, and enable modeling of more general surfaces or elements with different shapes and properties. Most of these programs are designed to trace rays through sequentially defined surfaces, and, therefore, they are called “sequential raytracing” codes. On the other hand, a non-sequential raytracing method is used in illumination software, such as ASAP® (Brault Research Organization), LightTools® (Optical Research Associates, Inc.), TracePro® (Lambda Research Corp.) and ZEMAX® (Focus Software, Inc.), which traces a number of rays in a non-sequential manner, where the rays emerging from a light source interact with any surface or element in any order and may even strike the same surface;element multiple times. It is especially useful in modeling of optical elements and systems with more general and complex geometry, as well as analyzing stray light, scattering and illumination in both imaging and non-imaging systems.

Another modeling method uses the similarity of the transverse field distribution of a laser beam to a Gaussian function, as described in Section 2.2. Also, for propagation of an arbitrary real laser beam, a beam propagation factor M^2 (also known as a “beam quality factor”) can be used as a measure of how the real laser beam propagates in comparison to the ideal lowest-order Gaussian beam [Siegman 1990]. The M^2 factor is defined as the ratio of far-field divergence angles of real and ideal laser beams. That is,

$$M^2 = \frac{\theta_r}{\theta_o} = \frac{\pi\omega_o\theta_r}{\lambda} , \quad (2.10)$$

where the ideal Gaussian beam divergence angle is $\theta_o = \frac{\lambda}{\pi\omega_o}$ and the real laser beam divergence angle is θ_r . The M^2 factor has a minimum value of unity for the ideal lowest-

order Gaussian beam and a value greater than one for a real laser beam. When the M^2 factor is greater than one, the beam is called “ M^2 times diffraction-limited”. The measured M^2 factor can be used in the generalized ABCD matrix to simulate an optical system using a laser beam [Bélanger 1991].

When more thorough study of electric field in an optical system is required, physical optics modeling methods based on Maxwell's equation should be used. There is a variety of physical optics modeling software. An exemplary simulation engine is OPTISCAN[®], a Matlab-based optical simulation tool that is capable of simulating many optical phenomena like scalar and vector diffraction, thin-film interactions, and Babinet decomposition [Milster 2003].

3 BASIC REQUIREMENTS OF OPTICAL DATA DESTRUCTION (ODD) SYSTEM

This chapter discusses the crucial components for ODD systems and how each component is selected among many candidates. The first section reviews the available light sources and their pros and cons for use in ODD systems. The second part is devoted to focus sensors that are necessary to maintain the optical beam onto the data layer of a disc during destruction operation. Influence of a high-power beam on detector performance and the compatibility of focus sensors with a line beam are also discussed. To overcome problems associated with a high-power line beam, a novel focus sensing scheme using a diffractive optical element is proposed.

3.1 Light source

An important issue in developing such optical data destruction systems is to choose an appropriate light source. Some of the candidates include intense white light sources such as halogen tungsten and high-intensity discharge lamps, CO₂ lasers, Nd:YAG lasers, and high power laser diodes. A system using an intense focused beam from a 300-Watt halogen tungsten lamp destroyed data marks on CD-R discs with cyanine and azo dye materials, but data marks on phthalocyanine-dye CD-R discs were still visible after intense-beam exposure and the data mark contrast was enhanced [Akhavan and Milster 1999]. CO₂ lasers are attractive due to the availability of high power at low cost. A

preliminary destruction experiment is conducted on a CD-R disc using a focused beam from a 10-Watt CO₂ laser. Data marks on the dye layer remain clearly visible, as shown in Fig. 3.1(a), although polycarbonate is melted and bubbles are formed on the plastic surface, as shown in Figs. 3.1(b) and (c). Because of high absorption of the polycarbonate used as optical disc substrates at the wavelength of a CO₂ laser beam ($\lambda = 10.6\mu\text{m}$), light energy from a CO₂ laser is rapidly absorbed into polycarbonate substrates and has little influence on the data layer of a disc. On the other hand, Nd:YAG lasers (532nm and 1064nm) and HPLDs (808nm~980nm) provide high power at wavelengths that are transmissive through PC.

In an ODD system, a HPLD is chosen as a light source because of its compactness, low cost, and high wall-plug efficiency over Nd:YAG lasers. The 808nm wavelength of LD is selected based on optical power, cost and absorption of dye materials used in CD-R discs and of metal used in reflective layers.

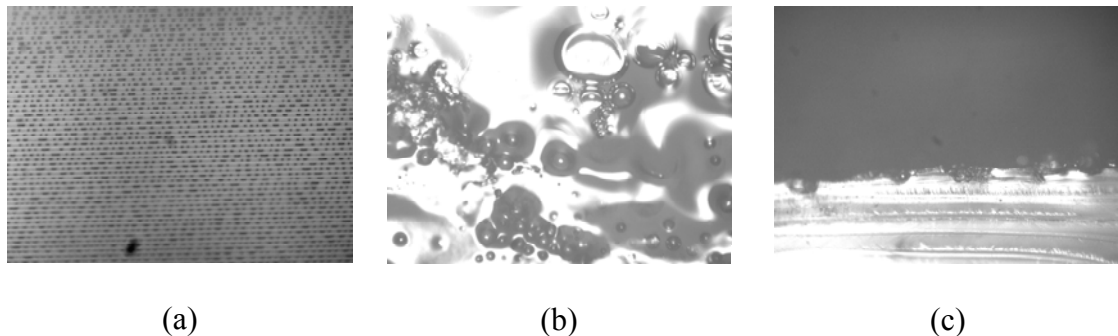


Figure 3.1 Images of a phthalocyanine CD-R disc exposed to a focused CO₂ laser beam. (a) Undamaged data marks on the data layer (imaged by a 100 \times microscope objective), and (b) top-view and (c) side-view of melted and bubbled polycarbonate (imaged by a 10 \times microscope objective).

3.2 Focus sensor

Like optical data storage systems, an ODD system needs a means to sustain the laser beam focused on the data layer as a disc rotates, because the position of the focused beam moves in and out of focus as much as $\pm 50\mu\text{m}$ and the depth of focus of a laser diode beam entering a disc is less than $10\mu\text{m}$. For example, with $\lambda = 808\text{nm}$ and $NA = 0.5$, the depth of focus is $1.6\mu\text{m}$, which is much smaller than $100\mu\text{m}$, the axial movement range of a disc. Thus, a focus sensor and a focus-compensating mechanism are necessary in an ODD system.

A few problems arise in ODD focus sensing if a conventional focus sensor [Cohen 1987], such as knife-edge, astigmatic, or wax-wane is used in an ODD system. The first problem relates to detected energy levels. Since optical media including dye materials and metal reflectors have high reflectivity at available HPLD wavelengths ($808\sim 980\text{nm}$) and conventional focus sensors are designed to use a significant fraction of the reflected light, the high level of light energy focused onto a photodiode can deteriorate its performance. There are studies showing that high energy beam applied to a silicon photodiode gives rise to morphological damage and electrical degradation, such as leakage current and decrease in responsivity [Giuliani and Marquardt 1974, Kruer *et al.* 1976, Watkins *et al.* 1990, Arora and Dawar 1996]. In addition, a neutral density filter is not applicable due to distortion in the transmitted beam caused by light absorption and resulting temperature increase in the filter.

A second problem relates to the focus sensor function. Some focus sensors such as astigmatic sensor are designed to use a nearly point light source, but a HPLD emits a very

astigmatic beam from the rectangular output aperture that produces an effective line source. Therefore, it is inappropriate to use a conventional focus sensor in an ODD system.

To overcome the problems related to an intense line beam, the focus sensor using a diffractive optical element (DOE) is proposed. Only the two weak +3rd order diffraction beams generated from two grating segments comprising the DOE are used for focus sensing. It is also compatible with both a point source and a line source. Further discussions on the DOE focus sensor are provided in Chapter 5.

For the purpose of simulating the HPLD beam through the ODD system, the beam is represented by the rays emanating from an extended line source with finite divergence angles, which is the limited-divergence raytracing (LDRT) method described in Chapter 4. The divergence angles and the aperture dimensions of the HPLD can be used as input parameters for the simulation. For the simulation of the ODD system, a number of rays emitted with the top-hat angular distribution (full angles of 10° and 38°) from a rectangular object (200 × 1 μm) are used.

3.3 Package dimensions

It is desirable to have a small-form factor when ODD systems are commercialized, so that one can be placed and used on a desk in an office. The ODD system needs to be comparable in size to commercial optical pickup heads, since the basic optical geometries of both systems are similar. A concern for reducing the size of the ODD system is the bulky heat sink and fan used to dissipate heat from the HPLD. One solution is to separate

the HPLD and the heat sink from the pickup head and only move the pickup with the HPLD position fixed. For this solution, the HPLD beam should be collimated and delivered to the pickup head with minimum light loss. Another solution is to pulse the laser rather than operate in the continuous mode to reduce the HPLD-generated heat. The pulse width and the repetition rate as well as the operation condition including the speeds of a rotary motor and a linear stage need to be carefully chosen so that the undestroyed data mark area is small enough to ensure complete destruction of data on the disc. Also, the focus servo should be guaranteed to work with pulsed light. The two proposed solutions may be used in conjunction.

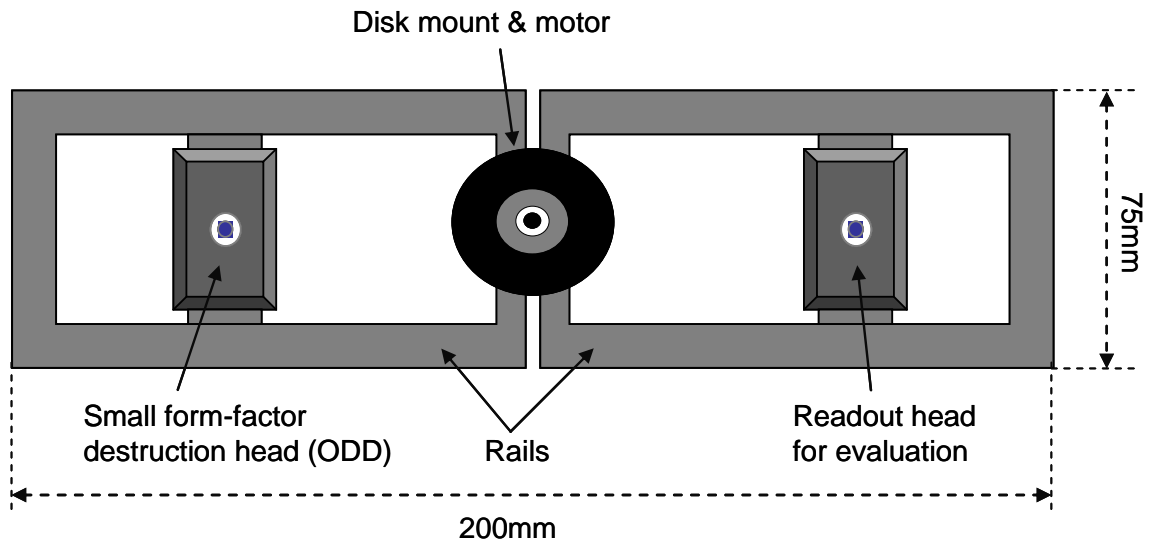


Figure 3.2 Schematic of a small-form factor ODD device with an evaluation head. The proposed dimensions of the entire device are 200mm × 150mm in the disc plane and 100mm in the device height.

A schematic drawing of a small-form factor ODD device is presented in Fig. 3.2. The packing dimensions of the entire device are 200mm × 150mm in the disc plane and

100mm in the device height. Notice that a readout head is included in the device for the purpose of evaluating its performance after destruction operation.

3.4 Objective lens and actuator

An objective lens determines the size of a focused beam on a disc. For higher beam irradiance on a disc, a high-NA objective lens is used. It should be designed to compensate the aberration through the disc substrate and to have enough working distance between the lens and the top of the substrate to search the focus. Also, a single-element molded aspheric lens is preferred to an objective lens with multiple spherical elements. As far as lens material is concerned, it is desirable to use a glass lens than a plastic lens, since the lens heating may arise during high-power destruction operation. In general, glass has lower coefficient of thermal expansion (CTE) than any type of plastic. The CTEs for fused silica and Bk7 are $0.55 \times 10^{-6}/K$ and $7.5 \times 10^{-6}/K$, while the CTE for plastic is greater than $25 \times 10^{-6}/K$. Furthermore, the weight of the objective lens should not be too great to sacrifice the focus servo performance.

In fact, the lens mass has influence on the resonance frequencies of the actuator. The actuator operation frequency should be selected away from the resonant frequencies due to the focus servo failure. Also, the actuator needs to have the moving range large enough to find focus quickly. A range of $\pm 1\text{mm}$ is desired for the ODD systems. A necessary function in the actuator is the focus search mode, which is used when the disc is initially placed on the system or the focus is lost during operation. The actuator is translated its whole moving range back and forth at a frequency of 1 Hz. From the

generated FES, the system quickly finds the best focus and determines the distance to move the lens.

3.5 Detector

The first consideration for a detector is the sensitivity at the source wavelength. For near-infrared HPLDs selected, a Silicon PiN photodiode is suitable. Other factors influencing the detector performance are noise and rise and fall time. But, the quality of photodiodes used in commercial optical pickup head would suffice for ODD systems.

The geometry and dimensions of the detector depend on the focus servo technique. For the current development of ODD systems using the DOE focus sensor, a quad-cell photodiode is necessary to generate a differential focus error signal. Also, the dimensions of the active area need to be carefully chosen to work with a elongated line beam from a HPLD. The active area dimension in the HPLD lateral direction (slow axis) should be large enough to receive significant amount of the returned light, while the cell widths in the HPLD vertical direction (fast axis) should be narrow enough to prevent the other diffraction order beams from affecting the servo performance.

3.6 Servo electronics

The servo electronics calculate the FES from the detector signals and send the signal to the voice coil actuator to move the objective lens in the direction to reduce the focus error. Figure 3.3 shows the diagram of the closed-loop control system for a DOE focus servo.

This is a generic control system for a differential focus servo. Four detector signals (A, B, C, D) produced from the returned light are fed to the servo electronics. After going through several operational amplifiers for calculations, an FES is generated and compared to the desired focus position, which is, in general, an offset. The signal is amplified and compared to the previous actuator position. This comparison gives rise to the proper position of the lens and corresponding amount of voltage that is applied to the actuator coil. The actuator with the objective lens mounted on is moved in the axial direction to compensate the focus error. By repeating this procedure in a closed feedback loop, the focus error is minimized.

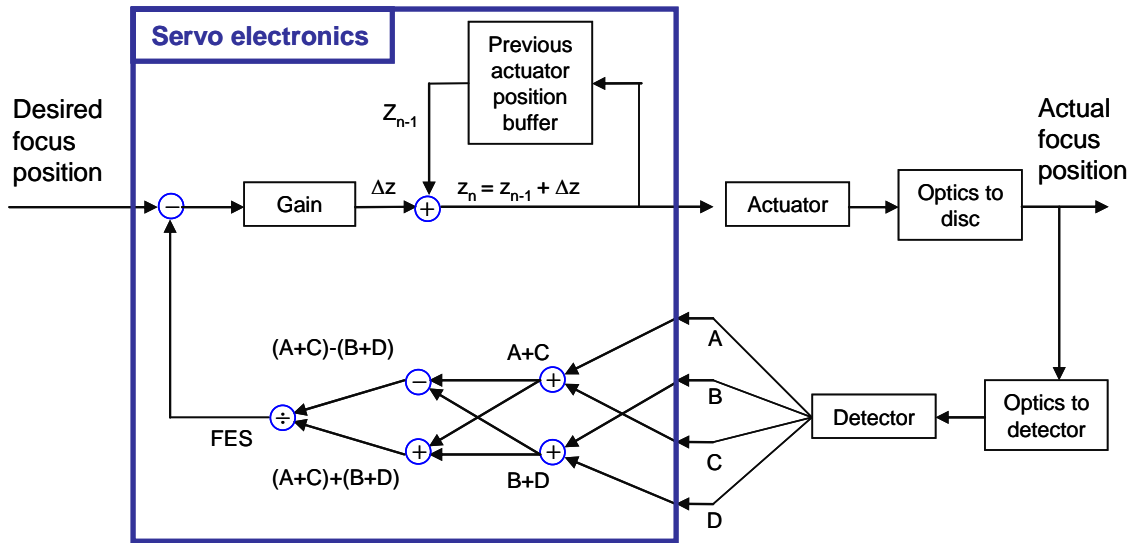


Figure 3.3 Diagram of a closed-loop control system for a DOE focus servo.

4 INVESTIGATION INTO HPLD BEAMS AND METHODS OF MODELING

OPTICAL SYSTEM USING HPLD

Although there have been separate reports showing spectrally-resolved lateral modes of an HPLD and a change in spatial coherence with specific types of semiconductor lasers, as described in Section 2.3, there has been little study on propagation behavior of HPLD beams in optical systems. In this chapter, thorough investigation on optical properties such as near-field and far-field patterns, spectrally-resolved lateral modes and corresponding optical spectrum and spatial coherence is made using a commercially available HPLD (High Power Devices Inc. HPD-1010, $\lambda = 808\text{nm}$, $P_{\text{out}} = 1\text{W}$, $D_x \times D_y: 100 \times 1\mu\text{m}$). In particular, quantitative relation between lateral modes and spatial coherence of an HPLD beam is drawn from the observed spectrally-resolved lateral modes and mutual intensities that are calculated from the observed interferograms with varying separations at different current levels. The consequent information on the HPLD beam is used to model such beam in a simple two-lens system. The modeling methods used for the comparison study include Gaussian beam propagation, incoherent superposition of multiple Hermite-Gaussian modes, and limited-divergence raytracing (LDRT). The results obtained from the modeling methods are compared to the experimental real HPLD beam in the two-lens.

4.1 Lateral modes of HPLD

The near-field irradiance and the far-field intensity along the x axis (lateral direction) from the commercially available HPLD are measured at $I/I_{th} = 1.29$. The near-field irradiance profile shown in Fig. 4.1(a) is obtained by processing a grayscale image of the beam at the output facet that is captured using a $3\times$ microscope objective and a CCD camera (Pulnix TM62-EX, 758×581 pixels, pixel size: $11 \times 11\mu\text{m}$). The far-field intensity distribution in Fig. 4.1(b) is measured using a photodetector at a distance as the HPLD mounted on a rotary stage is rotated at steps of 0.1° . The lateral near-field irradiance is nearly top-hat in shape with six peaks, and the far-field angular intensity in the x axis is practically top-hat, except some ripples. The multiple peaks and ripples in the distributions originate not from a single 5th order (six lobes) lateral mode, but from multiple lateral modes, which is shown in the following discussion.

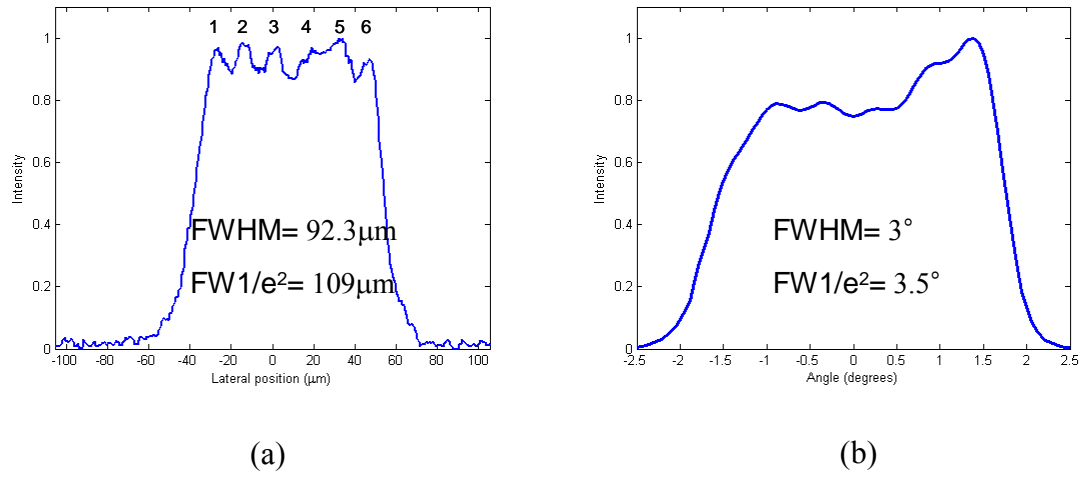


Figure 4.1 Images of near-field irradiances and far-field intensity of the HPLD beam at $I/I_{th} = 1.29$. Multiple peaks in the distributions are indicative of lasing of higher-order lateral modes.

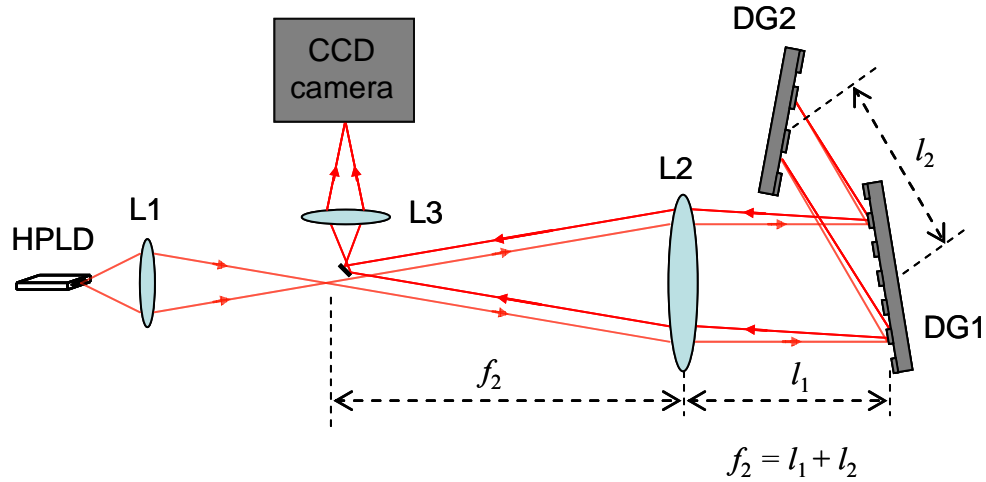


Figure 4.2 Layout of a double-pass monochromator setup for observing the spectrally-resolved HPLD beam. f_2 is the focal length of L2 and the sum of the distances between L2 and DG1 and between DG1 and DG2 is set to be equal to f_2 . The periods of DG1 and DG2 are $0.83\mu\text{m}$ and $1.67\mu\text{m}$, respectively.

To verify the presence of the lateral modes and their influence on beam propagation characteristics, the laser beam is spectrally-resolved in a double-pass monochromator setup, as shown in Fig. 4.2. The near-field HPLD beam magnified by lens L1 ($40\times$ microscope objective) is nearly collimated in the fast axis by L2 (Acromatic doublet with focal length= 400mm) and directed to two reflection gratings (DG1 and DG2) with periods of $0.83\mu\text{m}$ and $1.67\mu\text{m}$, respectively. The beam diffracted off DG2 returns at a small angle, and the beam double-passes L2 and DG1. The -1st order diffraction from DG1 and DG2 are used. The spectrally-resolved near-field beam is imaged by L3 onto the CCD camera (Pulnix TM62-EX). The small tilt of DG2 gives rise to a 4mm off-axis shift of the double-passed beam at the focal plane of L2, and the resulting coma calculated in a raytracing program is less than 0.6 wave for the 4mm shift,

due to the low F-number of L2 ($F/10$). The asymmetric aberration that might be caused by the small tilt of DG2 is indiscernible in the CCD images of the spectrally-resolved lateral modes. Also, the temperature of the LD is maintained at 25°C throughout the measurement using a thermoelectric cooler (TEC). Figures 4.3(a), (b) and (c) present the content of lateral modes in the HPLD beam and their spectra at different current levels ($I/I_{\text{th}} = 1.06, 1.29$ and 1.61). The spectra of the HPLD beam are obtained using an optical spectrum analyzer (HP 70950A). The span of the spectrum plots is 3nm , and a resolution setting of 0.08nm is used. At just above threshold ($I/I_{\text{th}} = 1.06$), three low-order lateral modes are observed. The lowest-order mode is separated from the 1^{st} and 2^{nd} order modes, since they belong to different longitudinal modes. At a raised current level ($I/I_{\text{th}} = 1.29$), seven lateral modes are observed, and the highest-order mode is the 5^{th} order. The near-field irradiance distribution in Fig. 4.1(a) is a superposition of the lateral modes in Fig. 4.3(b), and the six peaks of the near-field pattern result from the 5^{th} order mode with six lobes. At a higher current level ($I/I_{\text{th}} = 1.61$), more than 15 lateral modes are observed with some of the modes nearly overlapping in space. This overlapping of modes implies that lateral modes belonging to different longitudinal modes have nearly the same wavelength. Furthermore, the content of the lasing modes at high current levels is not constant. Instead, it varies frequently with time. It is observed that this frequent lateral mode hopping is aggravated when even a small amount of the optical beam is fed back to the cavity due to reflection or scattering from any elements. These higher-order lasing modes cause the output beam divergence in the slow axis to be many times diffraction limited.

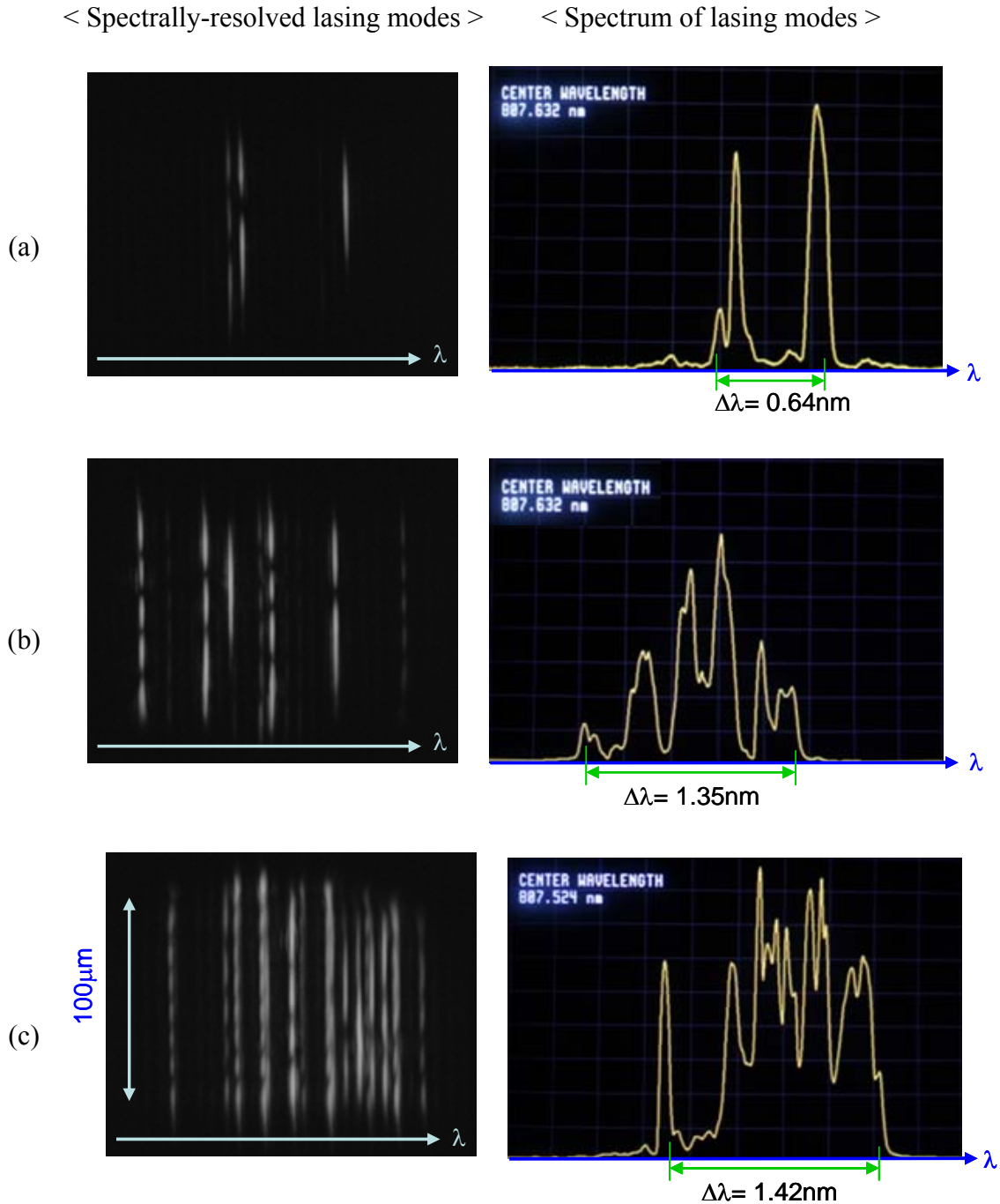


Figure 4.3 Images of near-field irradiances of spectrally-resolved HPLD lasing modes ($P_{\text{out}} = 1\text{W}$) and the corresponding spectra measured in an optical spectrum analyzer at the injection current of (a) $I/I_{\text{th}} = 1.06$, (b) $I/I_{\text{th}} = 1.29$ and (c) $I/I_{\text{th}} = 1.61$.

4.2 Coherence of HPLD beam

The content of the transverse modes in a laser beam defines its spatial coherence. The transverse modes of the laser beam are mutually uncorrelated, and each mode at the output facet is fully spatially coherent, provided there is no frequency degeneracy [Wolf and Agarwal 1984]. Since the vertical mode number q is always zero due to a thin active layer of an HPLD, frequency degeneracy is prohibited. Although each individual mode is coherent, the coherence of a multimode beam is essentially partially coherent. It is known that spatial coherence of the LD output beam is degraded with increasing number of lateral modes [Chang-Hasnain *et al.* 1989, Mailhot *et al.* 2000]. In this section, a Young's double slit interferometer (YDSI) experiment is performed to understand the coherence property of an HPLD beam with respect to lateral modes. The information necessary to gain further insight to the spatial coherence property of the HPLD beam is the mutual intensity, which is obtained using the interferogram images acquired from the YDSI experiment. In the following paragraphs, optical coherence theory is briefly reviewed, and the experimental procedure and the calculation method for the mutual intensity are described.

Coherence of fields between r_1 and r_2 with a time difference of τ is measured by the mutual coherence function Γ . That is,

$$\Gamma_{12} = \langle U(r_1, t + \tau) U^*(r_2, t) \rangle , \quad (4.1)$$

where U and U^* are the optical field and its complex conjugate, and the angle brackets refer to time-averaging. The total irradiance of the fields at r_1 and r_2 of the observation plane is

$$I(r_1, r_2, \tau) = I_1 + I_2 + 2\sqrt{I_1 I_2} \operatorname{Re}[\gamma_{12}(\tau)] = I_1 + I_2 + 2\sqrt{I_1 I_2} |\gamma_{12}(\tau)| \cos[\alpha_{12}(\tau)], \quad (4.2)$$

where I_1 and I_2 are field irradiances at r_1 and r_2 , $\gamma_{12}(\tau) = \frac{\Gamma_{12}(\tau)}{\sqrt{\Gamma_{11}(0)\Gamma_{22}(0)}}$ is the normalized mutual coherence function and $\alpha_{12}(\tau) = \arg[\gamma_{12}(\tau)]$. If a source is quasimonochromatic, the spatial coherence is represented by the normalized mutual intensity μ_{12} . That is,

$$\mu_{12} = |\gamma_{12}(0)| = \left| \frac{J_{12}}{\sqrt{\Gamma_{11}(0)\Gamma_{22}(0)}} \right|, \quad (4.3)$$

where $J_{12} = \Gamma_{12}(0)$ is the mutual intensity. Note that mutual intensity is independent of location in the observation plane.

The fringe visibility V is defined as

$$V = \frac{I_{\max} - I_{\min}}{I_{\max} + I_{\min}}, \quad (4.4)$$

where I_{\max} and I_{\min} are local maximum and minimum of the fringe modulation and measured locally. From Eqs. (4.2) - (4.4), the visibility becomes

$$V = \frac{2\sqrt{I_1 I_2}}{I_1 + I_2} \mu_{12}. \quad (4.5)$$

The normalized mutual intensity is expressed in terms of V, I_1 and I_2 as follows. That is,

$$\mu_{12} = \frac{I_1 + I_2}{2\sqrt{I_1 I_2}} V. \quad (4.6)$$

Given an interferogram image and two irradiance images with each slit blocked, V, I_1 and I_2 is calculated to generate the mutual intensity.

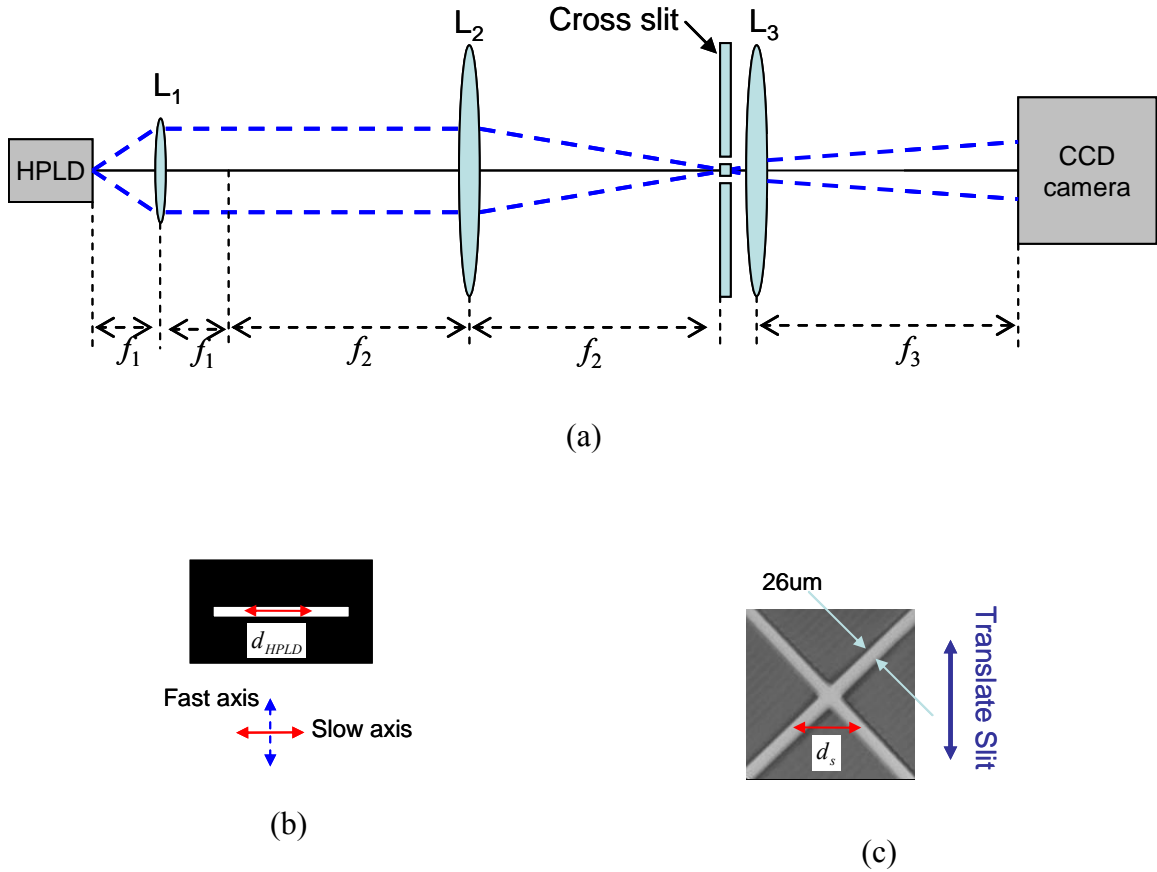


Figure 4.4 Coherence measurement of HPLD beam. (a) Experiment setup, (b) separation at HPLD output aperture and (c) the central portion of the cross slit with slit widths of $26\mu\text{m}$.

The setup for the YDSI experiment is illustrated in Fig. 4.4(a). A HPLD beam is imaged onto a cross slit by lenses L_1 ($f_1 = 4.52\text{mm}$) and L_2 ($f_2 = 400\text{mm}$) and forms an elongated line beam with dimensions of $8.85\text{mm} \times 0.2\text{mm}$ at the slit. The cross slit, shown in Fig. 4.4(b) is lithographically fabricated on a chrome mask, and the slit width is $26\mu\text{m}$ and the angle between slits is 90° . The cross slit lets two points (separated by d_s) of the imaged HPLD beam pass through and interfere, and the interferogram images are

captured using a CCD camera. As the slit separation d_s is varied by translating the cross slit in steps of 100 μm in the direction perpendicular to the elongated direction of the line beam, the spatial coherence is observed as a function of separations between two points at the HPLD aperture, d_{HPLD} . d_{HPLD} is related to the slit separation d_s by the imaging lens magnification $M = 88.5$. That is, $d_{\text{HPLD}} = d_s / M$. To observe the change in the spatial coherence of the HPLD beam with increasing lateral mode number, the interferograms are obtained at different LD current levels. The interferogram images and the irradiance profile across the fringes at $I/I_{\text{th}} = 1.06, 1.29$, and 1.61 are provided in Figs. 4.5, 4.6, and 4.7, respectively. The distances in the images are d_{HPLD} . The observed interferogram patterns from the cross slit are unusual in that there are crossed beams as well as the fringe pattern and that there is a bright line beam at the center of the fringe pattern. The former originates from the two diffraction patterns from each slit. The first zero irradiance location of the sinc diffraction pattern from the rectangular slit aperture is 12.4mm from the center of the fringe pattern, which are well outside of the CCD area ($10.25 \times 8.5\text{mm}$). The latter is not a fringe but the beam transmitted through the chrome-coated area of the mask. One reason for this curious line beam is that significantly more light illuminates the masked area than the slit area. Despite the high optical density (OD) of the chrome mask ($OD = 3$), and with the assumptions of uniform power distribution over a geometrical beam, a simple calculation of relative powers of light transmitted through the chrome mask and through the slits shows that the through-chrome power is 12% of the through-slit power. The remaining difference in power is explained by the fact that the light through the slits is diffracted into a larger area at the CCD, but the

transmitted light is focused, resulting in a higher irradiance. As expected, the fringe visibility drops quickly as d_{HPLD} increases. However, it does not completely disappear, even for $d_{\text{HPLD}} > 30\mu\text{m}$ at $I/I_{\text{th}} = 1.61$.

In addition to the interferogram images, separate slit-only irradiance images are recorded by the CCD and a computer at each given slit separation and current level, to obtain information on the amounts of light reaching to the observation position from each slit, which are I_1 and I_2 . One slit is blocked by a knife-edge, and the diffraction pattern through the other slit is recorded, and vice versa.

To provide more quantitative information to the spatial coherence property of the HPLD beam, the mutual intensity, the effects observed due to temporal is calculated. Over the range of optical path length difference (OPD) tested in the YDSI experiment, the effects observed due to temporal coherence are negligible, because the OPD is considerably smaller than the coherence length of the source, which is approximately 33mm for $d_s = 4\text{mm}$ and a rectangular power spectrum with a wavelength span of 2nm. The visibility at the observation plane is determined from the local fringe modulations of the interferograms in Figs. 4.5, 4.6 and 4.7. I_1 and I_2 are obtained from the separate slit-only irradiance images. The normalized mutual intensity is obtained using Eq. (4.6) and presented in Fig. 4.8 as a function of the separation at the HPLD aperture for different current levels. The main observations from Fig. 4.8 are that the mutual intensity decreases sharply as the separation at the HPLD increases and diminishes with increasing current level. μ_{12} reaches minimum values at $d_{\text{HPLD}} = 20.34\mu\text{m}$, $13.56\mu\text{m}$ and $11.3\mu\text{m}$ for $I/I_{\text{th}} = 1.06$, 1.29 and 1.61 , respectively. After passing the minimum values, μ_{12} increases

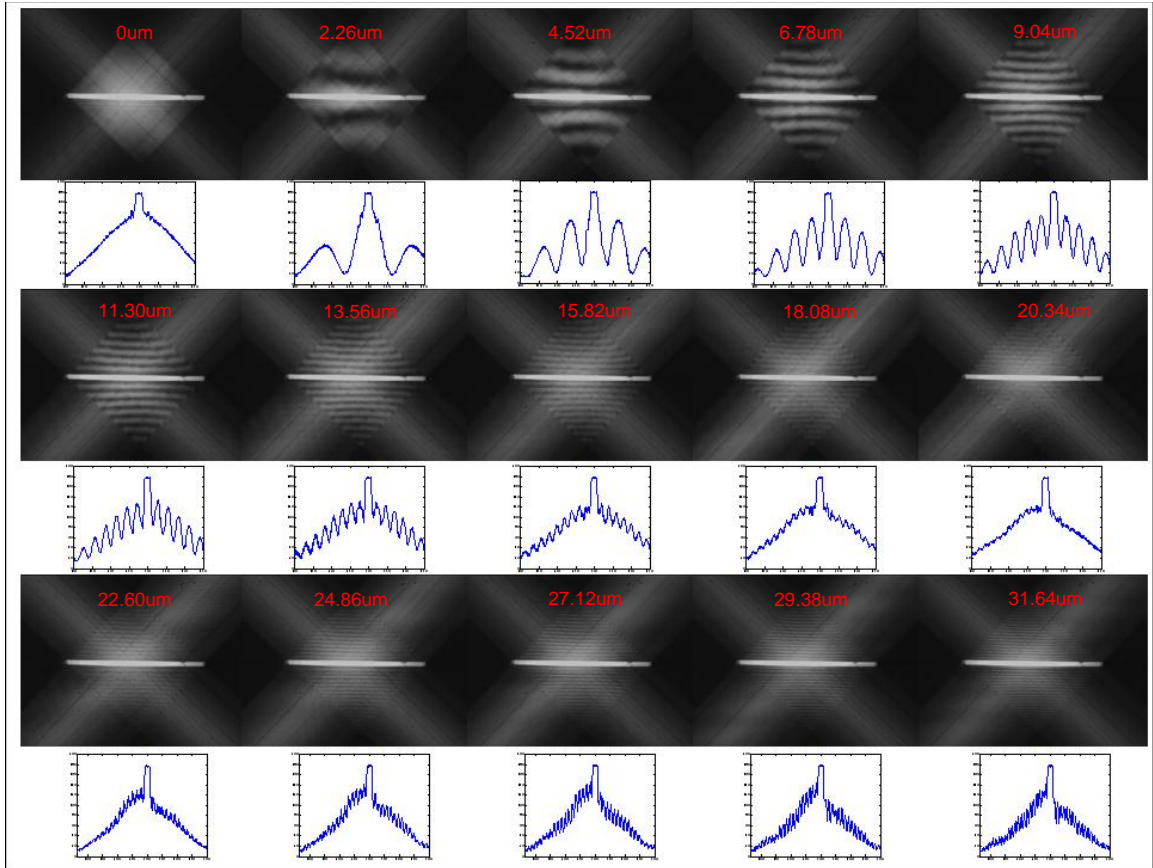


Figure 4.5 Interferogram fringes from the YDSI experiment. The HPLD is operated at $I/I_{th}=1.06$. The numbers in the images are the separation of the two points at the HPLD.

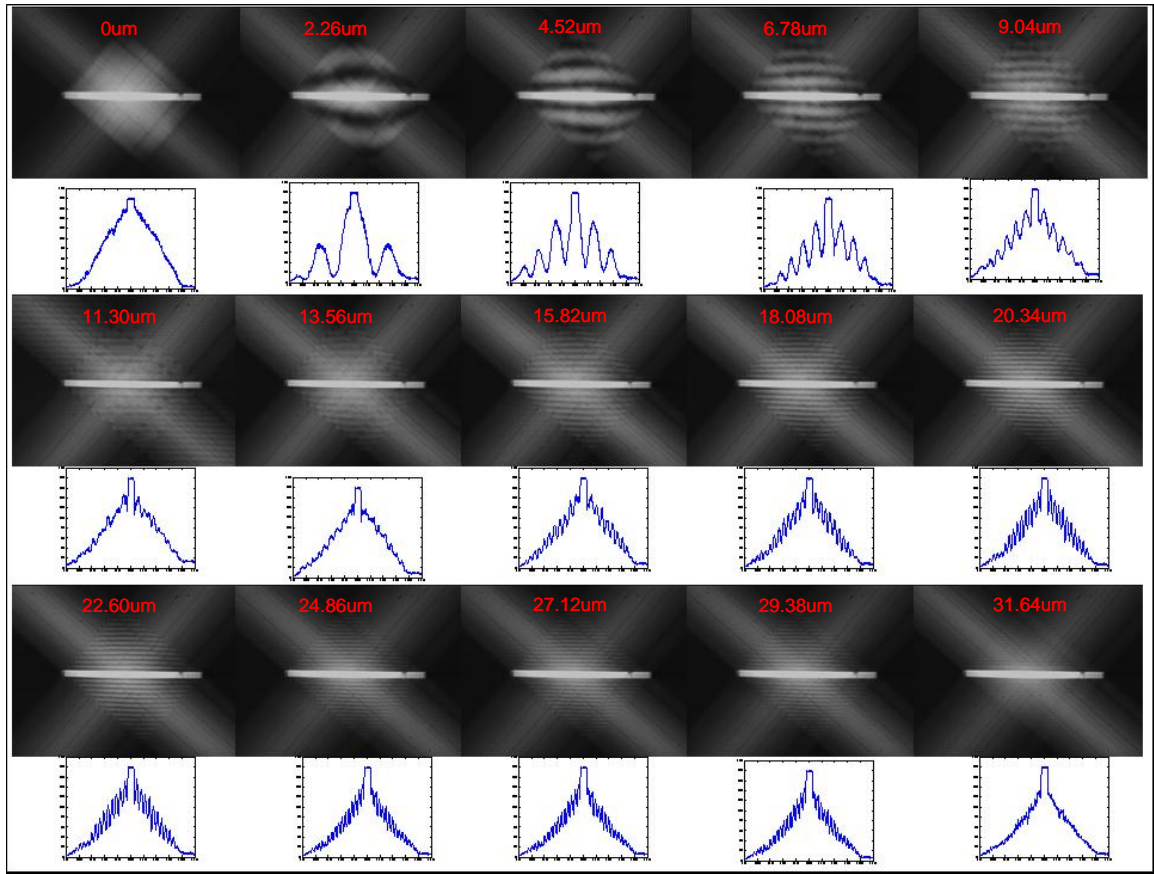


Figure 4.6 Interferogram fringes from the YDSI experiment. The HPLD is operated at $I/I_{th}=1.29$. The numbers in the images are the separation of the two points at the HPLD.

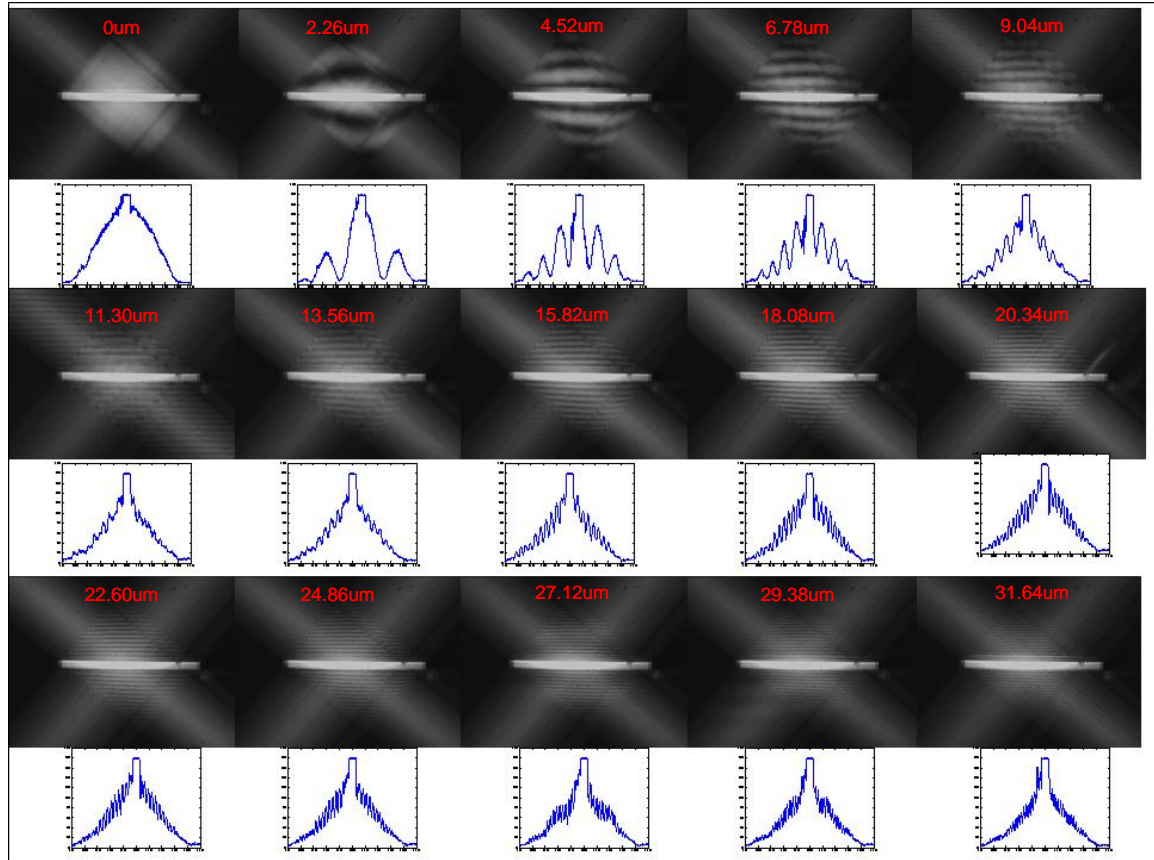


Figure 4.7 Interferogram fringes from the YDSI experiment. The HPLD is operated at $I/I_{th}=1.61$. The numbers in the images are the separation of the two points at the HPLD.

to 0.35 and oscillates. In this oscillating regime, there are some d_{HPLD} values where μ_{12} is greater for $I/I_{\text{th}}=1.61$ than for $I/I_{\text{th}}=1.06$, which implies that the width of the mutual intensity is not always smaller for a beam with more lateral modes. It is dependent upon the locations of the two points at the HPLD facet. However, in general, a HPLD beam well above the threshold has low spatial coherence ($\mu_{12} < 0.35$) for separations greater than 10 μm .

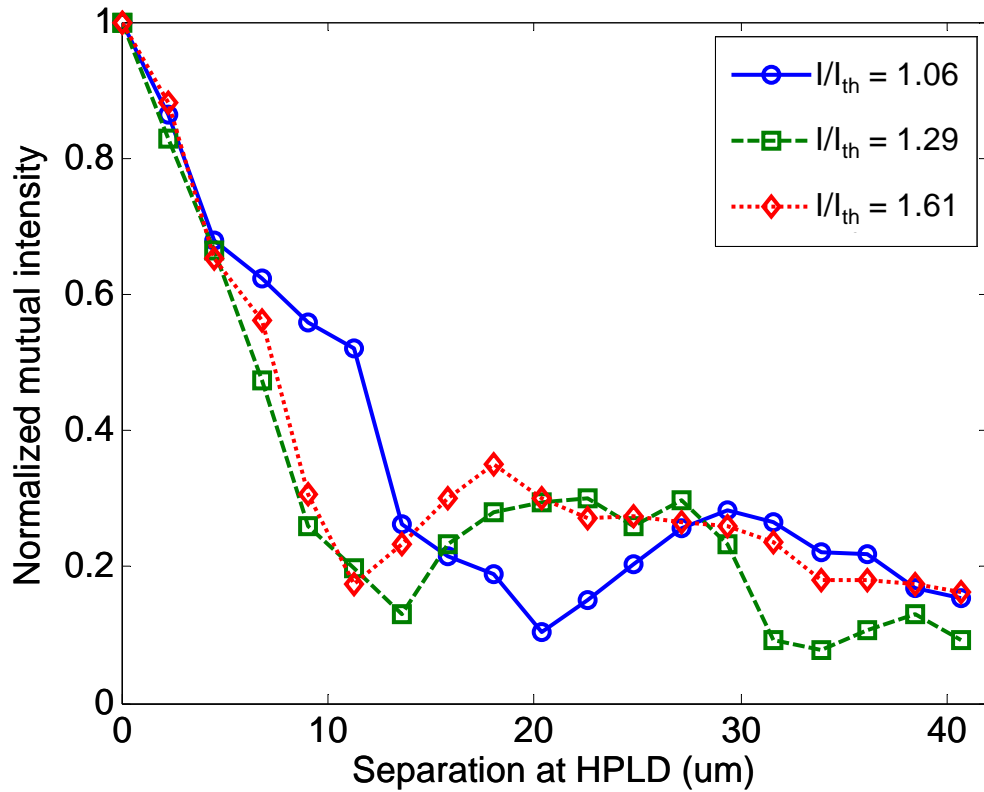


Figure 4.8 Normalized mutual intensity, μ_{12} , as a function of separation at the HPLD aperture at different current levels ($I/I_{\text{th}}=1.06, 1.29, 1.61$).

4.3 Modeling of an optical system using HPLD

Among various modeling methods of optical systems, as described in Section 2.3, a geometrical optics model using the LDRT method is presented as a good candidate for modeling an optical system using a HPLD. Since it is simple to implement, it enables modeling of complex optical systems involving obscuration and large aberrations and requires a minimum number of measurements for calibration. For the purpose of comparison, propagation behaviors of a Gaussian beam and a multimode Hermite-Gaussian beam through the optical system are also discussed.

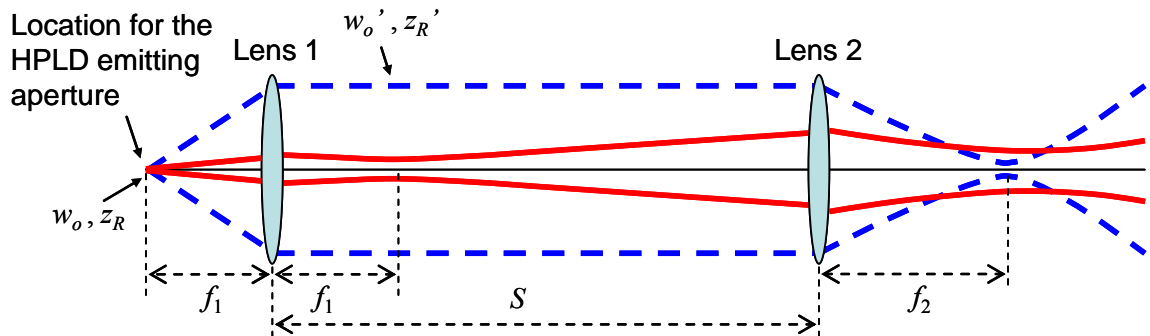


Figure 4.9 A simple two-lens setup where Lens 1 geometrically collimates the beam emitted from an HPLD and Lens 2 focuses the incident beam. The solid and dashed lines imply the slow-axis and fast-axis beams, respectively, which are presented on the same plane.

A simple two-lens setup shown in Fig. 4.9 is of interest, since such a two-lens arrangement is used in the prototype ODD system. The emitting aperture of a HPLD is located at the front focal plane of Lens 1 so that the diverging output beam is geometrically collimated, and after propagating a distance S the beam is focused by Lens 2. The approximate beam width curves of the HPLD beam in the slow and fast axes are

plotted on the same plane. The solid and dotted lines indicate the slow- and fast-axis beam widths, respectively.

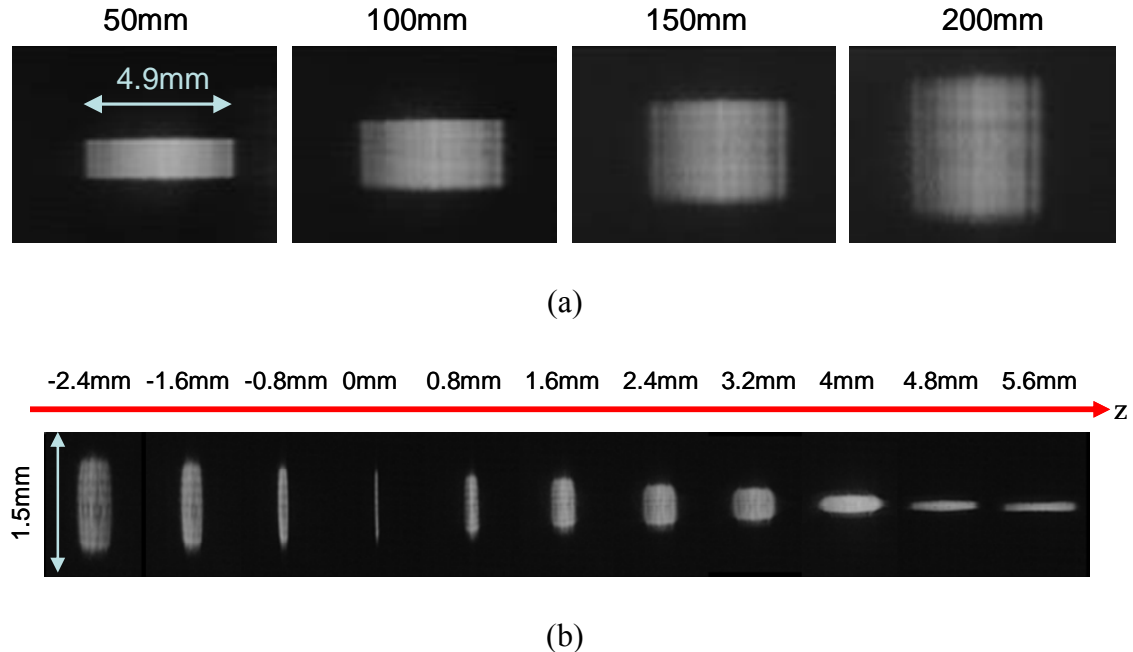


Figure 4.10 Experimental measurements. (a) Transverse irradiance images of an HPLD beam collimated in the fast axis observed at different distances from Lens 1. The vertical (slow-axis) width increases, but the beam remains collimated in the horizontal (fast-axis) direction. (b) Transverse irradiance images of the HPLD beam being focused by Lens 2 through its back focal plane. The minimum beam radii occur at the back focal plane in the horizontal (fast-axis) direction and at around 5.6mm after the back focal plane in the vertical (slow-axis) direction due to the systematic astigmatism of the HPLD beam. All the images are observed at $I/I_{th} = 1.29$.

The HPLD described in Section 4.1 is used and operated at $I/I_{th} = 1.29$ for this experiment. Figure 4.10(a) shows the experimentally measured transverse images of the HPLD beam at different axial positions after collimated by Lens 1 ($f_1 = 4.52\text{mm}$). An interesting observation is that the beam is collimated in the fast axis but diverges in the

slow axis as it propagates away from Lens 1. Figure 4.10(b) presents the transverse images of the HPLD beam through the focus of Lens 2 ($f_2 = 25.8\text{mm}$) when the separation between the lenses S is 151.6mm. The beam in the fast axis is focused at the geometrical focal plane of Lens 2. In the slow axis, the minimum beam width occurs at $\Delta z = 5.6\text{mm}$, which is far after the fast-axis beam is focused. This through-focus behavior exhibits the propagation property of an astigmatic beam, as discussed in Section 2.2.

Firstly, the propagation of a lowest-order Hermite-Gaussian beam with waist radii of $32\mu\text{m} \times 0.5\mu\text{m}$ at the facet is considered. The beam widths of the lowest-order mode observed in Fig. 4.3(b) are analyzed, where $I/I_{\text{th}} = 1.29$. The beam waists (w_o , w_o') and Rayleigh ranges (z_R , z_R') at the HPLD facet and at the back focal plane of Lens 1 that determine Gaussian beam propagation characteristics are summarized in Table 4.1. The Gaussian beam forms the second waists in both fast and slow axes at the back focal plane of Lens 1. The beam has significantly different Rayleigh ranges in fast and slow axes due to differences in beam waist radii at the LD facet. The Rayleigh ranges after Lens 1 are

Table 4.1 Beam waists and Rayleigh ranges in the slow and fast axes. ($f_1 = 4.52\text{mm}$ and $f_2 = 25.8\text{mm}$ are used for focal lengths of Lens 1 and Lens 2)

	HPLD facet			Back focal plane of Lens 1		
	w_o	z_R	z_R/f_1	w_o'	z_R'	z_R'/f_2
Slow axis	$32\mu\text{m}$	3.98 mm	0.88	0.036 mm	5.13 mm	0.2
Fast axis	$0.5\mu\text{m}$	$1\mu\text{m}$	0.0002	2.3 mm	21 m	815

21 meters in the fast axis and 5.1mm in the slow axis. Therefore, while the fast-axis beam remains collimated, the slow-axis beam diverges relatively rapidly after the second waist. The distance between the second waist and Lens 2, $z_2 = S - f_1$, now becomes the object distance for imaging by Lens 2. The ratio z_R / f_2 of the fast-axis beam is nearly infinite, so that the waist after Lens 2 occurs at the geometrical focal plane of Lens 2 regardless of z_2 . In the slow axis, on the other hand, the waist location after Lens 2 varies considerably with z_2 due to the small ratio ($z_R / f_2 = 0.2$). The slow-axis waist location z_2' with respect to Lens 2 is normalized by f_2 and plotted as a function of z_2 / f_2 in Fig. 4.11(a). The slow-axis waist after Lens 2 occurs at the geometrical focal plane of Lens 2 when $z_2 = f_2$, which is closer toward Lens 2 when $z_2 < f_2$ and farther from Lens 2 when $z_2 > f_2$. These three ranges of the slow-axis waist location z_2' can also be presented in terms of S . That is,

- (I) $z_2' < f_2$ if $S < f_1 + f_2$,
- (II) $z_2' = f_2$ if $S = f_1 + f_2$ and
- (III) $z_2' > f_2$ if $S > f_1 + f_2$.

Figures 4.11(b), (c) and (d) show the axial profiles of the beam widths in the fast and slow axes through the two-lens system for the three cases: $z_2 / f_2 = 0.06, 1$ and 5.7 , or, equivalently, $S / (f_1 + f_2) = 0.2, 1$ and 5 . The lenses are drawn by vertical arrows. It is important to note that the systematic astigmatism is nontrivial in Figs. 4.11(b) and (d) although no inherent astigmatism is applied to the Gaussian beam at the HPLD emitting aperture location in this simulation. The systematic astigmatism is zero in Fig. 4.11(c), since the beam waists in both axes take place in the same location after Lens 2 for $z_2 = f_2$.

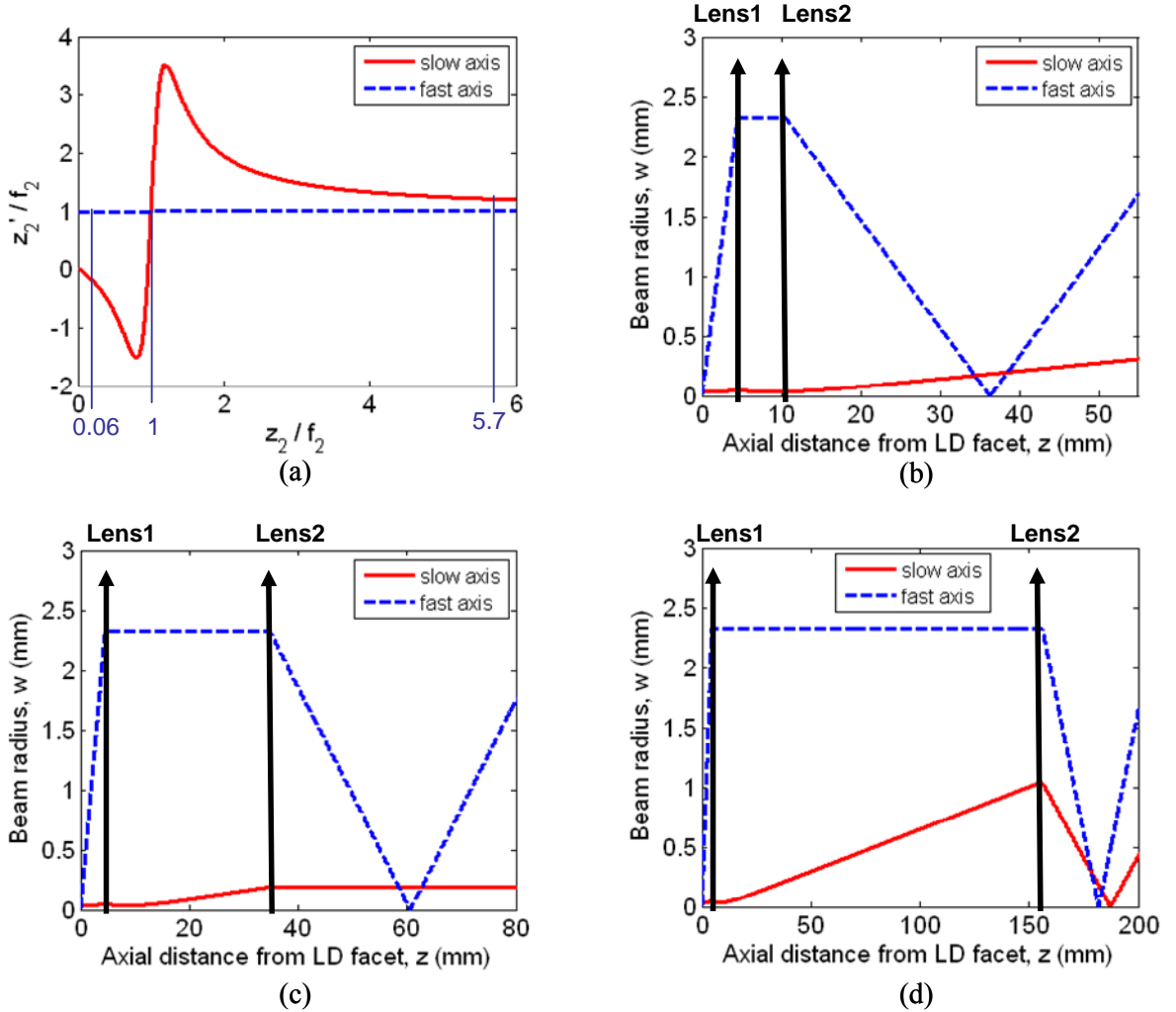


Figure 4.11 (a) Normalized Gaussian beam waist location after Lens 2 as a function of the normalized beam waist location before Lens 2. The waist location in the slow axis varies significantly as z_2 or the separation between Lens 1 and Lens 2, S , changes. (b), (c), (d) Axial profiles of the beam widths in the fast axis (dashed line) and the slow axis (solid line) through the two-lens system for the three cases: $S / (f_1 + f_2) = 0.2, 1, 5$, respectively. The systematic astigmatism is nontrivial in (b) and (d) when no inherent astigmatism at the HPLD facet is assumed for this simulation.

This Gaussian beam simulation presents the propagation behavior similar to the observed real HPLD lowest-order-mode propagation through the two-lens system, in that the slow-axis beam diverges after collimation by Lens 1 and that the slow-axis waist after Lens 2 depends strongly on the lens separation S . However, there is a significant discrepancy in the slow-axis beam widths of the Gaussian beam and the HPLD beam, when the HPLD beam has higher-order lateral modes at $I/I_{th} > 1$.

Instead of using only the lowest-order mode, a set of higher-order Hermite-Gaussian modes can be used as a light source model for a HPLD beam, since the real HPLD beam has multiple lateral modes. Six Hermite-Gaussian modes ($p = 0, 1, 2, 3, 4, 5$) with the lateral beam waist radius of the lowest-order mode being $32\mu\text{m}$ are used for the slow axis to match the spectrally resolved modes at $I/I_{th} = 1.29$. The Gaussian beam with the vertical waist radius of $0.5\mu\text{m}$ is used for the fast axis. The beam waist radii are then used in Eq. (2.9) to simulate the propagation of such Hermite-Gaussian modes. The cross-correlations among the lateral modes are ignored, since the intermodal beat frequency of the lateral modes of a HPLD beam is on the order of GHz, which is much a higher frequency than the detector frame rate or the frequency of photochemical or photothermal interaction used in optical data recording or destruction. Therefore, the irradiances of individual modes can be incoherently summed to predict the propagation characteristics of this multimode beam. Equal weighting factors of individual modes are used for this simulation due to the difficulty of measurement, especially at high-power operation. Figure 4.12 shows the transverse irradiance images of incoherent superposition of the multimode beam at various axial locations through the back focal plane of Lens 2,

along with the images of the lowest-order mode and the 5th order mode. Although the lowest-order and the 5th order modes exhibit the astigmatic nature of the HPLD beam, their beam widths and irradiance distributions are different from those of the real HPLD beam shown in Fig. 4.10(b). On the other hand, the through-focus behavior of the beam with incoherently summed six Hermite-Gaussian modes in Fig. 4.12(c) is similar to that of the real HPLD beam. The periodic ripples in the slow axis are present, as in the real

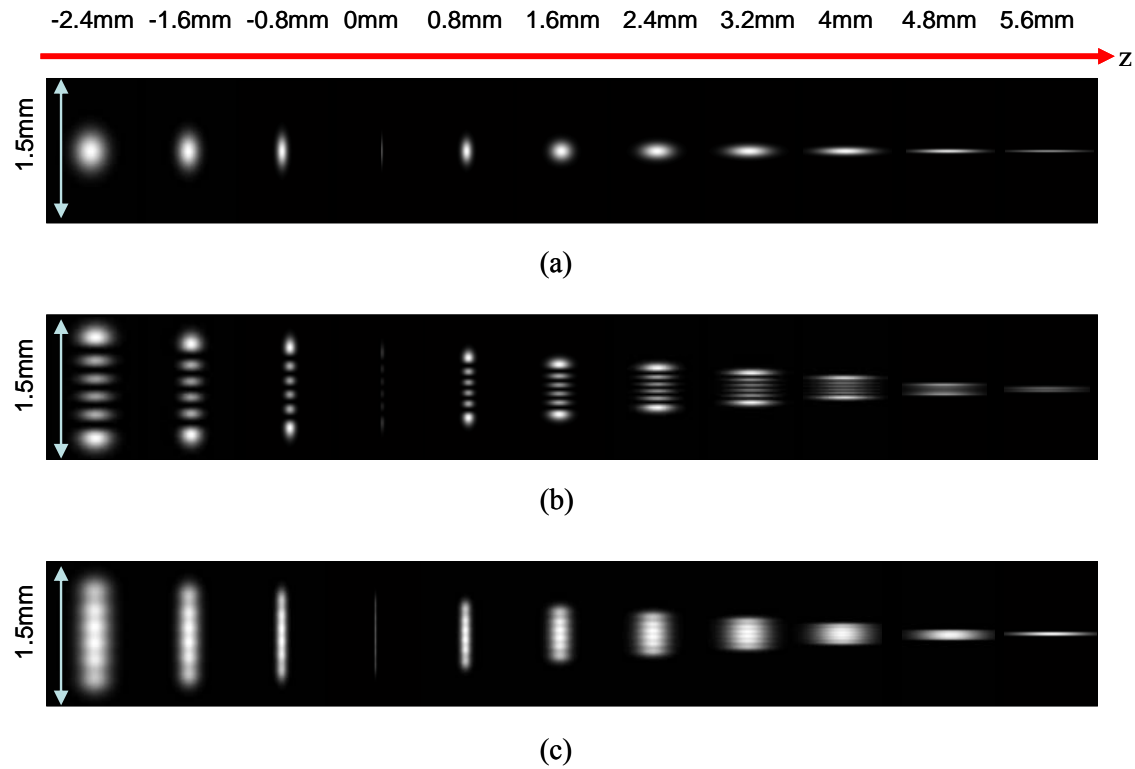


Figure 4.12 Simulated transverse irradiance images of (a) the lowest-order mode ($p = 0$) and (b) the 5th order mode ($p = 5$) through the back focal plane of Lens 2. (c) Through-focus transverse simulated irradiance images of an incoherent superposition of six low-order modes ($p = 0, 1, 2, 3, 4, 5$) with equal power weight factors.

HPLD beam, due to the higher-order mode content. The FW $1/e^2$ of the incoherent sum of six Hermite-Gaussian modes at the focal plane of Lens 2 is 0.876mm, which is considerably greater than the measured HPLD FW $1/e^2$ of 0.622mm. This difference is because the lateral modes of the real HPLD beam are not exactly Hermite-Gaussian modes. Champagne and his colleagues showed by numerical calculation of lateral modes of broad area lasers that the modes are non-Hermite-Gaussian beam but limited by the width of the current injection stripe [Champagne *et al.* 1995]. As shown in Fig. 4.13(a), this is confirmed by the slow-axis irradiance profiles of the real HPLD lateral modes observed in Fig. 4.3(b). For comparison, the theoretical Hermite-Gaussian modes are presented in Fig. 4.13(b). Since the FW $1/e^2$ of the lowest-order HPLD mode is 64 μm , half of the width is used as the beam waist radius of the Hermite-Gaussian modes. With the beam waist radius of 32 μm , the higher-order Hermite-Gaussian modes extend farther outside the emitting aperture width of 100 μm , while most higher-order HPLD mode power remains within the aperture width. Also, the HPLD modes are slightly asymmetrical. This shape difference demonstrates that the lateral modes of the HPLD beam are non-Hermite-Gaussian modes, which explains the difference in the FW $1/e^2$ of the HPLD beam and the incoherent sum of six lateral modes.

In addition to the discrepancy in the beam widths from those of the real HPLD beam, the Gaussian beam and Hermite-Gaussian beam propagation methods require accurate measurements of the beam waist of the lowest-order HPLD mode and power weighting factors of individual modes to use in the Gaussian and Hermite-Gaussian beam simulations. However, the mode content and their weighting factors fluctuate with time

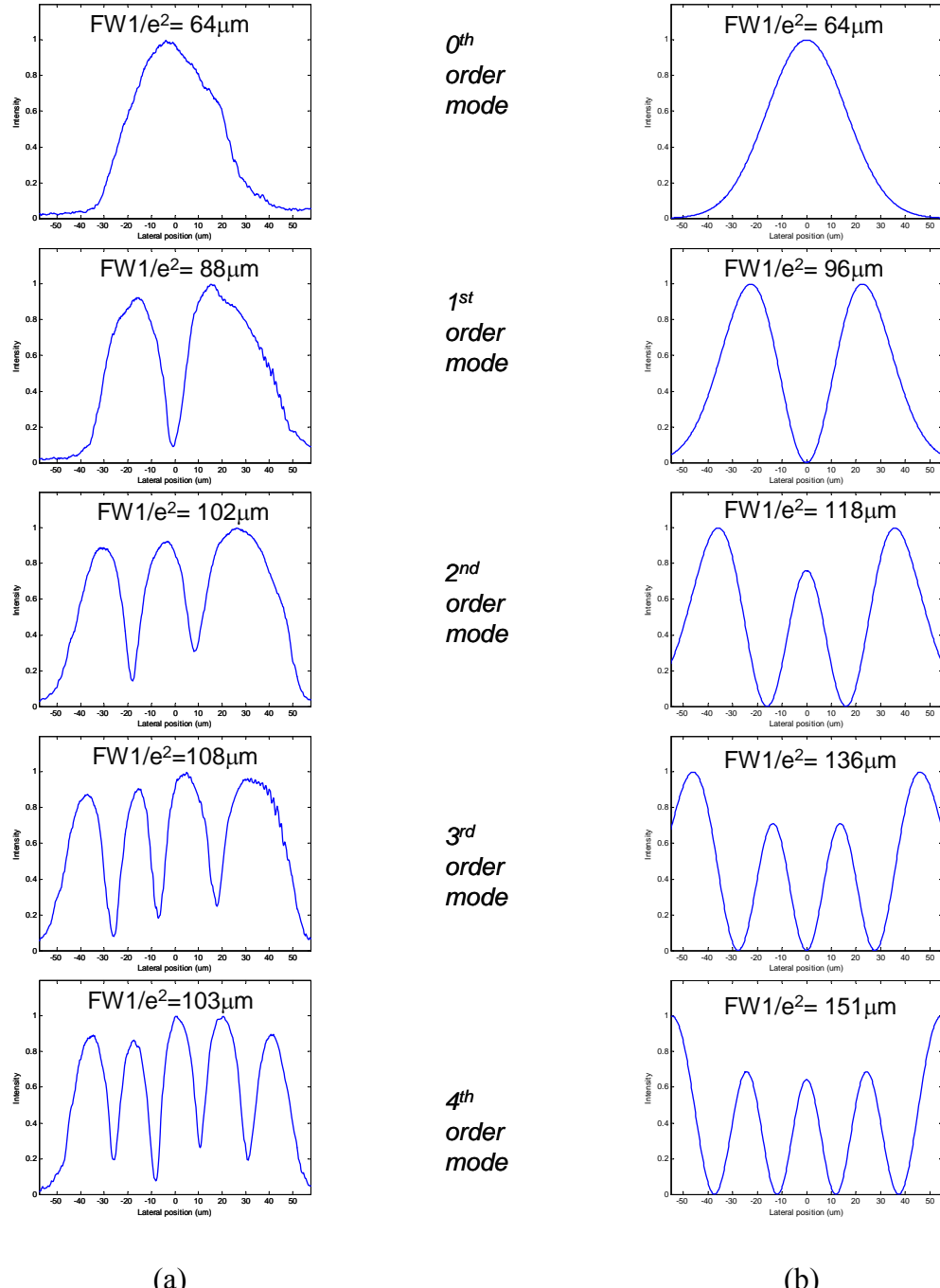


Figure 4.13 Slow-axis irradiance profiles of the HPLD lateral modes at the LD facet observed in Fig. 2.13(a) when $I/I_{th} = 1.29$ and the corresponding Hermite-Gaussian modes with $w_0 = 32\mu\text{m}$. The irradiances are normalized and the spans of the abscissas are the same in all the plots.

during high-power operation, which can be attributed to mode competition, optical feedback, or any minor change in injection current or temperature. Therefore, a more practical approach is necessary for designing optical systems using HPLDs.

In the following paragraph, a LDRT model using a commercial raytracing software (ZEMAX[®]) is used to simulate the propagation of a HPLD beam in the two-lens system.

To use the LDRT method, it is necessary to set up a proper light source model. The emitting aperture dimensions and the measured far-field divergence angles of the HPLD are used for the source model. Rays are emitted from random positions within a rectangular area whose dimensions are $100\mu\text{m} \times 1\mu\text{m}$, which are the HPLD emitting aperture dimensions from the HPLD specification sheet. The angular distribution of the rays emanating from the source is uniform along the fast and slow axes, and the measured FWHM ($3 \times 25.6^\circ$) or FW1/e² ($3.5 \times 54^\circ$) are used as the full widths of the uniform ray angular distribution. The transverse ray distribution in the far-field is elliptical. Such source model is employed in the LDRT model along with the aforementioned two-lens system. The 100,000 rays from the rectangular source are traced, and the powers carried by rays that arrive in the transverse planes are incoherently summed. The through-focus beam transverse irradiances are shown in Figs. 4.14(a) and (b) when the measured FWHM and FW1/e² are used, respectively. The through-focus behavior in the slow axis is similar in the two simulations, while the fast-axis behavior is different, because of the larger difference in the fast-axis beam divergence angles (25.6° and 56°). In both simulations, the slow-axis FW1/e² beam width at the focal plane is 0.58mm, which is

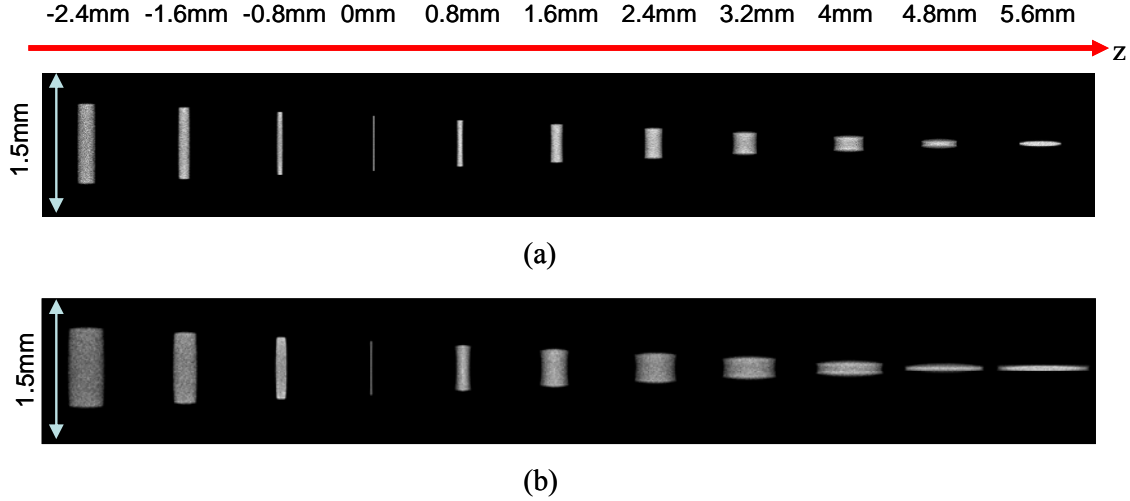


Figure 4.14 Through-focus transverse beam irradiances when the measured (a) FWHM ($3 \times 25.6^\circ$) and (b) FW1/e² ($3.5 \times 54^\circ$) of the far-field HPLD beam are used as the full widths of the ray angular distribution.

42μm smaller than the focused real HPLD beam (0.622mm). The width difference is expected, because the FW1/e² of the real HPLD near-field irradiance extends outside the 100μm HPLD aperture width, as shown in Fig. 4.1(a). When compared to the real HPLD beam, the simulation using the FW1/e² source angular distribution shows better agreement than the simulation using the FWHM. This good agreement is predicted from the mutual intensity measurement. The FW1/e² divergence angle of 3.5° used in the LDRT corresponds to a beam with a width of 13.2μm at the HPLD aperture using the diffraction relation $D \sim \frac{\lambda}{FW1/e^2}$, while the width of mutual intensity measured in the YDSI experiment at the same current level ($I/I_{th} = 1.29$) is 13.56μm. Therefore, the setting in the LDRT model of limiting the angular divergence to the measured FW1/e² is consistent with a set of single-mode beams with their widths equivalent to the mutual

intensity width.

Another observation is that there are no ripples in the raytraced beam irradiance profiles, since the lateral mode content of the real HPLD beam is not taken into consideration for the source model in the LDRT method. However, the multiple peaks with low modulation has little importance in applications like optical data destruction, where data marks are not instantly destroyed but gradually destroyed due to increased temperature.

Figure 4.15 provides the through-focus beam images obtained experimentally from the real HPLD beam and from the different simulation methods. Given the low modulation ripples are of little consequence in the simulation, the simulation method using incoherent superposition of multiple Hermite-Gaussian modes and the LDRT method using the measured FW $1/e^2$ divergence angles provides the closest through-focus behavior as the real HPLD beam. These two simulation methods are compared in Table 4.2, in the aspects of required prior measurements and computing power as well as suitable applications. For the simulation of HPLD beams in ODD systems, the LDRT method is preferred due to several reasons. Firstly, the ODD system is complex in that a DOE is used and influence of several diffracted orders to the FES signal should be modeled. Secondly, the beam is truncated by an aperture stop and more severely in the reflected beam when the disc goes out of focus. Thirdly, the lateral beam width should be accurately predicted to determine the adequate velocities of disc rotation and linear motor translation. It is necessary to prevent the destruction line beam from leaving any data mark area unexposed or from exposing the same area twice, which may result in burning.

Finally, far-field angles is easier to measure than lowest-order beam width, the lateral mode content and power weighting factors among the modes. It is an important consideration in the system manufacturing point of view, since a number of HPLDs needs to be measured and qualified to see if they meet the tolerance specifications.

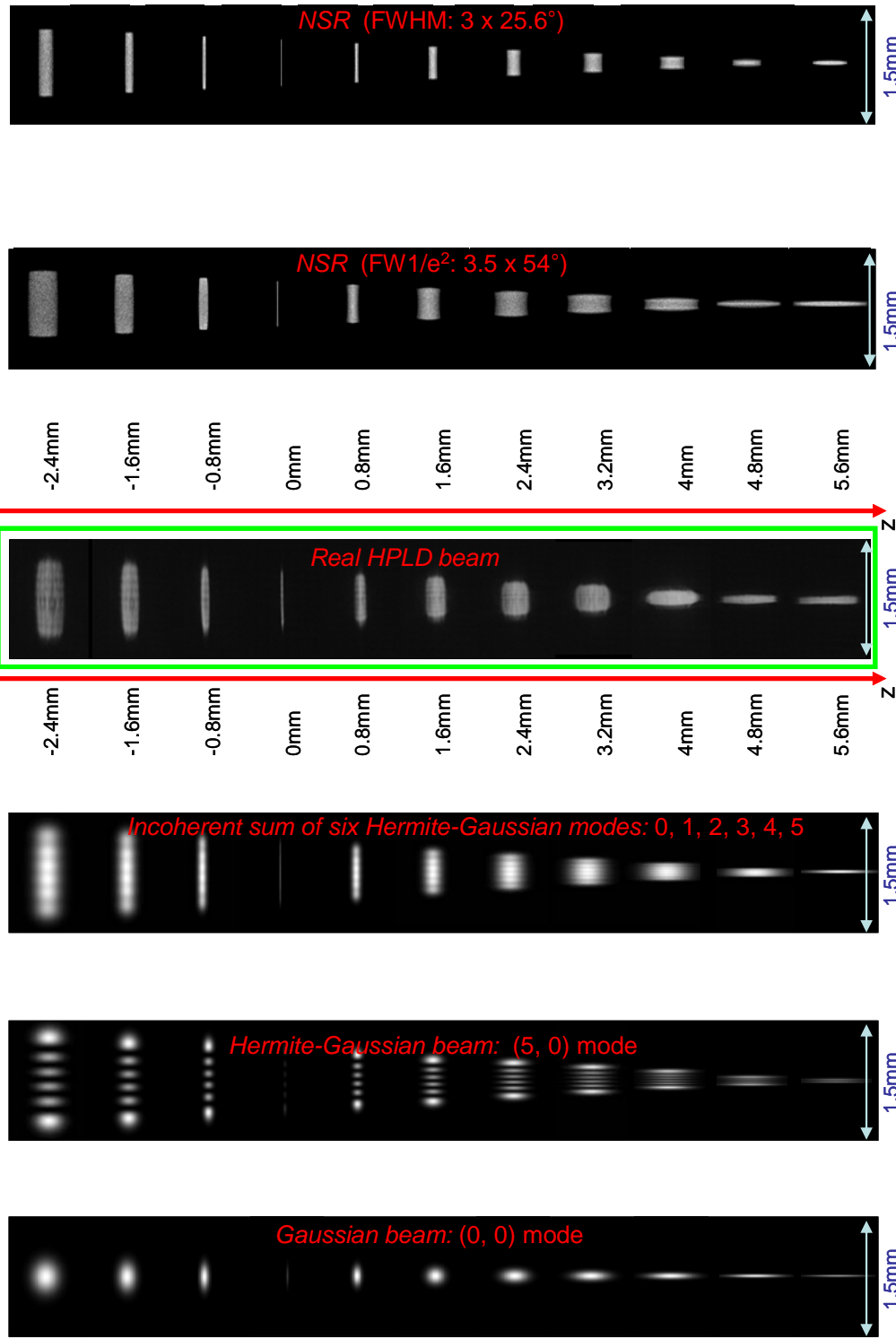


Figure 4.15 Summary of through-focus transverse beam irradiances from the real HPLD beam and from different simulation methods, presented in Figs. 4.10, 4.12, and 4.14. All the images are in the same scale.

Table 4.2 Comparison of Hermite-Gaussian propagation method and LDRT method.

	Incoherent superposition of Hermite-Gaussian modes	LDRT
Prior knowledge	<ul style="list-style-type: none"> • lowest-order mode beam width • number of lasing lateral modes <ul style="list-style-type: none"> • power weighting factors 	Far-field divergence 75angles
Computation power	Low (because Hermite-Gaussian beams are in analytical forms)	High (a number of rays should be launched)
Suitable applications	Optical systems where simulating accurate irradiance profiles is important	Highly aberrated or complex optical systems
Simulation results of HPLD beam	Larger lateral beam width (because the real HPLD beam is non-Hermite-Gaussian)	Lateral beam width close to the real HPLD beam width
	Ripples shown in the irradiance profiles.	No ripples related to lateral modes

5 DESIGN AND CONSTRUCTION OF THE ODD SYSTEM

This chapter provides details on optical and mechanical designs of an ODD system along with its basic functionality and optical characteristics. After some practical issues with temperature and alignment are discussed, the constructed prototype ODD system is presented.

5.1 Basic function and optical configuration

The basic function of an ODD system is to completely destroy physical data marks on optical media, making data irretrievable by any means. The ODD system exposes data marks to a focused high-power laser beam through the clear plastic substrate of a disc. Since physical destruction of data marks occurs inside the disc with the original structure of the disc maintained, no debris or hazardous fumes are produced during the destruction operation.

A schematic of the ODD system is presented in Fig. 5.1. The ODD system uses a single-emitter HPLD ($\lambda = 809\text{nm}$, $P_{\text{out}} = 4\text{W}$, output aperture $200 \times 1\mu\text{m}$). The diverging beam from the HPLD is collimated by a collimating lens ($f_{\text{col}} = 4.52\text{mm}$, $NA_{\text{col}} = 0.55$). The laser beam propagates through a polarizing beam splitter (PBS), because the HPLD is placed so that the emitted beam is *p*-polarized at the interface of the PBS. The *p*-polarized laser beam becomes circularly-polarized by passing through a quarter-wave plate in which the optic axis is rotated by 45° with respect to the polarization axis of the

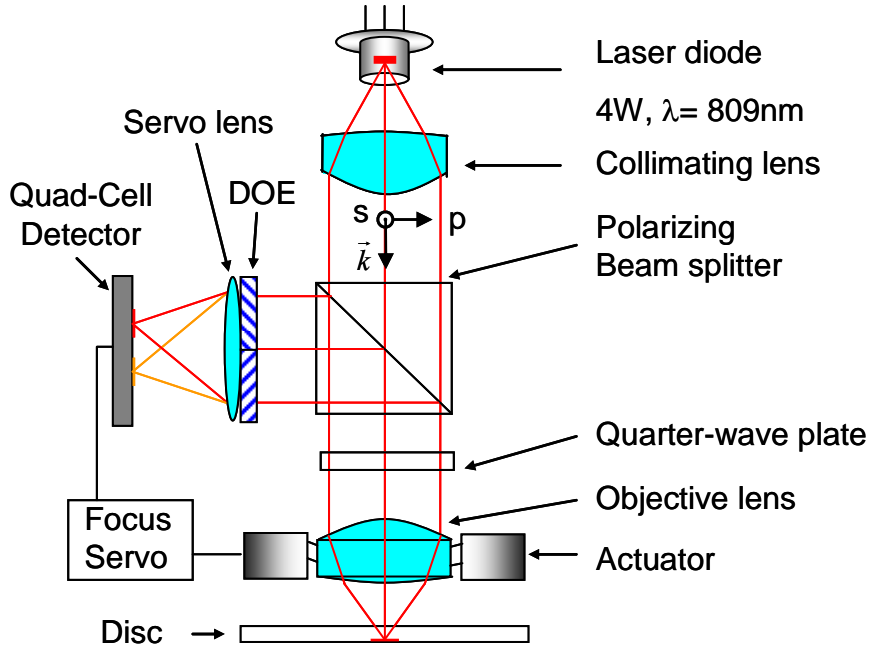


Figure 5.1 A schematic of an optical data destruction system. The beam from a high power laser diode is collimated, passes through various optics and focused on the data layer of a disk. The focus-lock is achieved with a DOE focus sensor and a closed-loop feedback servo.

incident beam. The beam is then focused onto a disc by an objective lens ($f_{obj} = 4.6\text{mm}$, $NA_{obj} = 0.41$). The focused beam on the data layer of the disc is almost a line, since the system images the wide laser output aperture onto the data layer. By situating the focused line beam in the radial direction across disc tracks, it is possible to expose a number of tracks (~ 100 tracks) at a time and minimize the total time required for destruction of a whole disc. Some of the light energy is absorbed in the data layer and the reflective layer, destroying data marks and surrounding area. The unabsorbed light reflects from the disc, passes through the objective lens and the quarter-wave plate and becomes *s*-polarized. The *s*-polarized light is directed by the PBS to a focus sensor. It is notable that the

combination of the PBS and the quarter-wave plate allows the light to be efficiently used for destruction and prevents the reflected beam from getting into the laser cavity, which might cause mode hopping and decrease in the HPLD lifetime. The focus sensor is comprised of a DOE, a servo lens ($f_{servo} = 25.8\text{mm}$, $NA_{servo} = 0.12$) and a quad-cell photodiode, as discussed in Chapter 3. The DOE is designed and the lens is selected to focus the two third-order diffraction beams onto the quad-cell detector and to have other orders away from the detector. The detector signals from the four cells are fed back to the servo electronics, which determine the level of the focus error and the corresponding axial translation distance of the objective lens to bring the lens focus to the data layer of the disc. The axial lens movement is made at a frequency of a few kHz by a voice coil actuator on which the objective lens is mounted. By the closed-loop feedback of the focus servo, the laser beam is kept focused as the disc spins.

5.2 Optical characteristics

The ODD system can be divided into two subsystems. The first subsystem images the laser diode output aperture onto the data layer of a disc. The other subsystem relays the image of the first subsystem on the data layer to the detector. The first-order magnifications of the imaging subsystem and the relay subsystem are 1 and 5.6, respectively. The design focused beam size in the radial direction of the disc (slow axis of LD) is $200\mu\text{m}$ and is calculated by the multiplication of the width of the LD aperture and the first-order magnification of the imaging subsystem. On the other hand, due to diffraction effects, the beam size in the disc tangential direction (fast axis of LD) is

$2.4\mu\text{m}$, which is obtained from Eq. (2.1) using $\lambda = 809\text{nm}$ and $NA_{obj} = 0.41$.

The real HPLD beam dimensions at the disc are measured at $I/I_{th} = 1.2$. The beam widths are obtained by processing a grayscale image of the focused beam. The measured FWHM dimensions of the focused beam on a CD data layer are $160\mu\text{m}$ in the disc radial direction and $2.5\mu\text{m}$ in the tangential direction. The beam width in the disc radial direction is smaller than the beam size obtained from the first-order calculation, partly because the width is measured at the half-maximum irradiance level. Another cause may be that the lateral modes of the LD in the slow axis do not fill the full LD output aperture at the low current level. The fast-axis beam width in the tangential direction is slightly larger than the Airy disk diameter, which might originate from aberrations in the optical system.

5.3 Thermal and mechanical considerations

There are some practical issues associated with building an ODD system. The first consideration is to keep the temperature of the HPLD low during high-power operation. Unless the excessive heat generated by the HPLD is removed quickly, the optical power decreases significantly and the lifetime of the device shortens. Therefore, a cooling system is necessary for an ODD system to deliver a designed amount of optical power for destruction and to prevent early system failure. In the prototype ODD system, the HPLD temperature is actively monitored and maintained at a room temperature (25°C). The HPLD is mounted on an aluminum block using thermally conductive epoxy, and a

thermistor is placed near the HPLD to sense the temperature. A thermoelectric cooler (TEC) element is attached to the base block, and a copper heat-sink and a fan are placed on the other side of the TEC to chill the temperature rapidly. Silicon-based compound is used on both sides of the TEC to facilitate fast heat transfer. If any increase in temperature around the HPLD is sensed by the thermal resistor, the temperature controller applies corresponding amount of voltage across the TEC element to transfer heat from on the HPLD side to the heat sink side. The transferred heat on the heat-sink is then efficiently and rapidly dissipated with the fan.

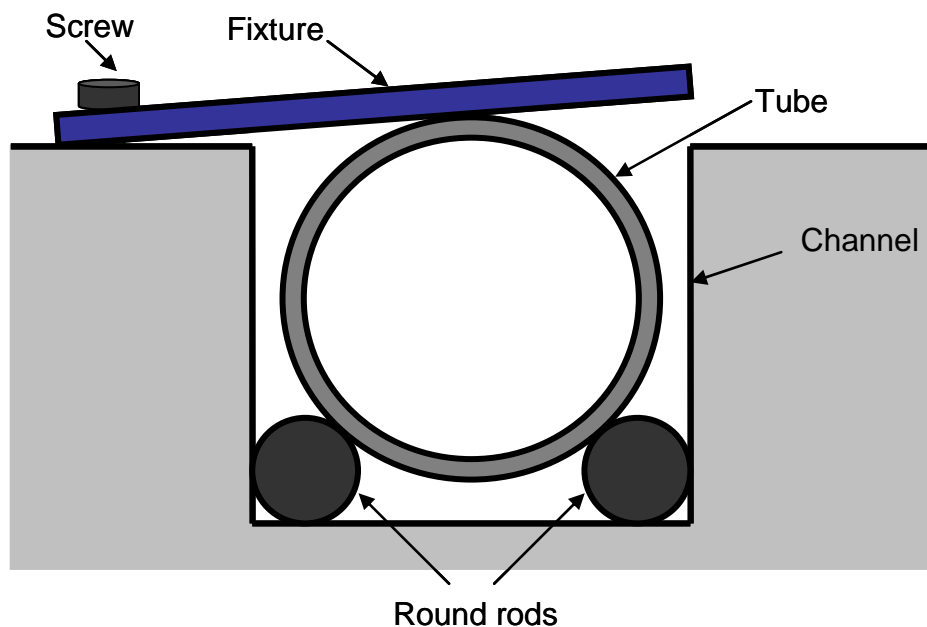


Figure 5.2 Mechanical alignment method. A tube with an optical element mounted is placed on top of two round steel rods and is secured by a fixture.

The second issue is the mechanical design associated with alignment and assembly of the ODD system. In the prototype ODD system, the simple and accurate mechanical alignment method illustrated in Fig. 5.2 is employed. Optical elements including lenses and the DOE are mounted on tubes with outer and inner diameters of 7.5mm and 6.2mm, respectively. The tubes are placed on the two round steel rods with a diameter of $3.2\text{mm} \pm 0.013\text{mm}$ at the corners of the channel that is made on the aluminum base along the beam paths. A fixture and a screw are used to secure the tubes. The round rods are used to enhance the positioning accuracy of the optical elements. Figure 5.3 shows the mechanical drawing of the prototype ODD system.

5.4 Construction of ODD system

An alignment telescope is used for the fine alignment of the optical elements that are already mounted on the tubes when the prototype ODD system is constructed. Figure 5.4 shows the constructed ODD system along with a disc. While the ODD system is stationary, a rotary motor and a linear stepper stage are used to spin and radially translate the disc, respectively.

The two motors as well as the LD and the TEC are controlled using the LabVIEW[®] software. The control panel of the program is shown in Fig. 5.5. The graphical representation of the ODD control program is provided in Appendix II. The input parameters in the control panel are the radial position of the beam on the disc and speeds of the linear motor and the rotary motors. The time for one rotation and RPM are displayed. The “run” button starts and stops the motion of the motors.

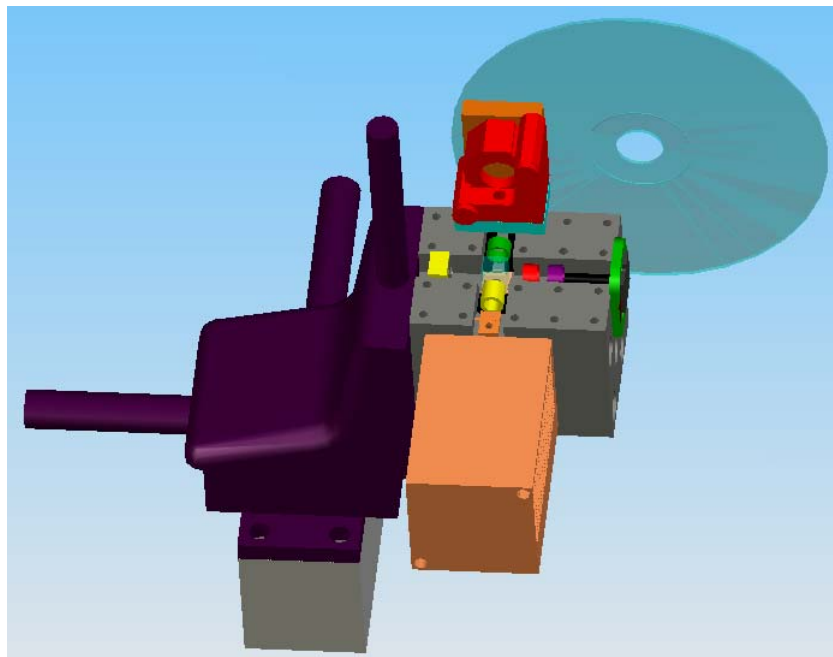


Figure 5.3 Mechanical drawing of a prototype ODD system.

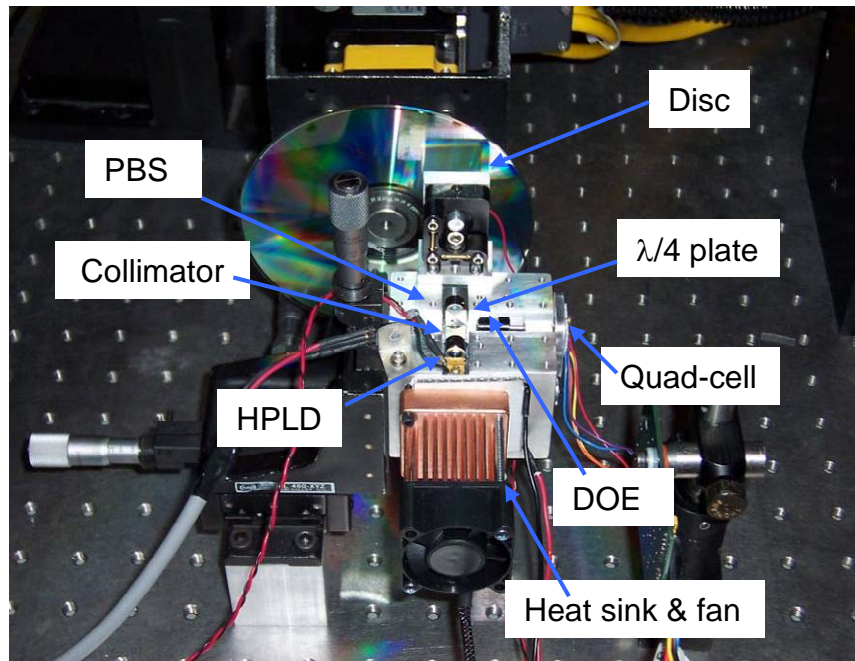


Figure 5.4 Constructed prototype ODD system.

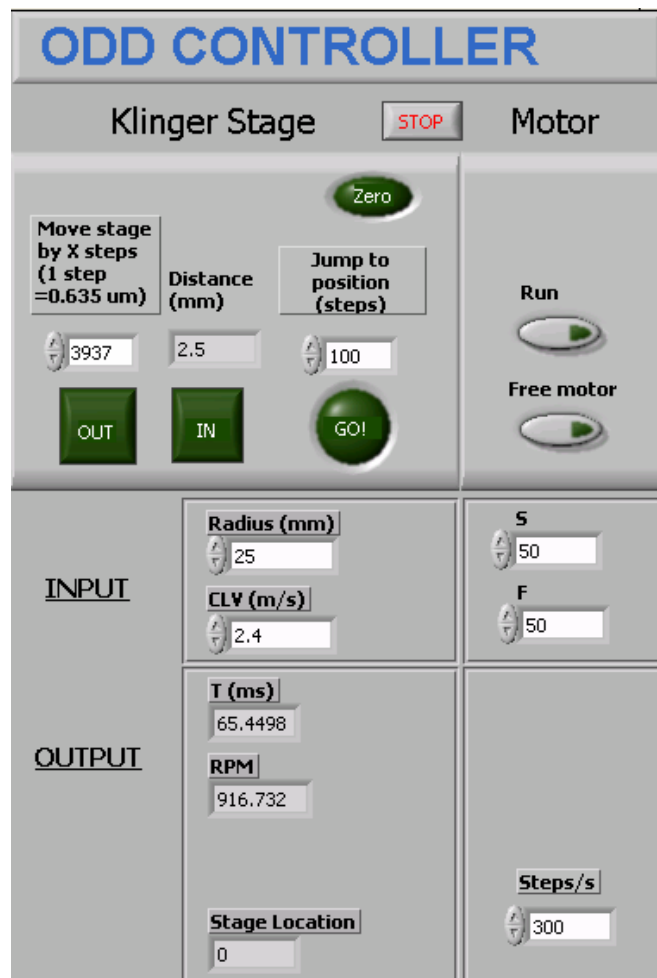


Figure 5.5 Control panel in LabVIEW program.

6 DOE FOCUS SERVO

In this chapter, a focus sensing technique using a diffractive optical element (DOE) is introduced. The DOE focus servo is useful in applications where focus sensing from an intense, broad-stripe laser beam is required. It solves two problems with known servos. Firstly, the DOE focus sensor prevents the photodetector from morphological damage and electrical degradation, resulting from an intense beam entering the detector of conventional focus servos. Also, the DOE focus sensor enables focus sensing with the elongated line beam emerging from an HPLD, which is impossible with some kinds of conventional focus sensors, like an astigmatic focus sensor. The DOE focus servo allows an ODD system to use only a small percentage ($< 2.5\%$) of the incident light energy for focus sensing.

After a short introduction to DOEs, generation of the DOE focus error signal (FES) is illustrated. Details on design of the DOE focus sensor and fabrication of the DOE for focus sensing are provided in Sections 6.3 and 6.4. Also, FES signals are simulated as a function of defocus at the disc using the LDRT method, and the DOE focus servo characteristics are evaluated from the simulated FES signals. An analysis on errors and tolerance is performed as well.

6.1 Basics of DOEs

A DOE is an optical component that utilizes diffraction of the incident light. The

diffraction originates from spatial variation of the transmittance (amplitude DOEs) or the thickness or refractive index of the component and the resulting change in optical path lengths of the incident wavefront (phase DOEs). A few simple examples include gratings and Fresnel zone plates [Born and Wolf 1999].

The diffraction efficiencies of a binary amplitude DOE and a binary phase DOE, for example, can be presented in analytic forms when the period of spatial variation is larger than the wavelength of the light, which ensures validity of the scalar diffraction calculation [Born and Wolf 1999]. For a binary amplitude DOE, the diffraction efficiency (DE) is

$$DE = \left[\frac{\sin(m\pi a)}{m\pi} \right]^2 , \quad (6.1)$$

where m is the diffraction order, and a is the duty cycle of the grating. For a binary phase DOE, the DE is

$$DE = \begin{cases} 4a^2 \cos^2 \left(\frac{\pi}{\lambda} OPD \right) & m = 0 \\ 4 \sin^2 \left(\frac{\pi}{\lambda} OPD \right) \left[\frac{\sin(m\pi a)}{m\pi} \right]^2 & m \neq 0 \end{cases} , \quad (6.2)$$

where OPD is defined as the difference of optical path lengths ($OPLs$) from the DOE and expressed as $OPD = OPL_2 - OPL_1 = (n_2 - n_1)t$, where n_1, n_2 are the refractive indices of incident and exiting media and t is the thickness of the periodic features in the DOE.

DOEs play crucial roles in various applications, such as laser beam shaping, beam sampling, optical tweezers, photolithography, X-ray imaging and aberration correction [Brenner and Jahns 2004]. The wide use of DOEs in various fields is due to their

capability of integrating many different optical functions into a single element, as well as being lightweight and having small volume.

6.2 Conceptual operation of DOE focus sensor

The DOE focus sensor uses a quad-cell detector to receive the light reflected from the disc. A focus error signal (FES) is determined by the difference of the two sums of the signals from two detector cells in the diagonal positions divided by the sum of all four signals. That is, the normalized FES is

$$FES = \frac{(A+C)-(B+D)}{A+B+C+D} , \quad (6.3)$$

where A, B, C and D are the signals out of each detector cell. This normalization makes the FES independent of disc reflectance and LD power variations and, thus, enables the servo to work during both low and high power operations.

The mechanism of the DOE focus servo is fundamentally the same as the knife-edge focus servo (also called as Foucault focusing method). The knife-edge method uses a sharp-edged element like a real knife to obscure the half of the return beam [Bouwhuis and Braat 1978]. As illustrated in Fig. 6.1, the FES, the difference of the two detector signals, becomes zero when the disc is in the focal plane of the objective lens. The FES becomes positive and negative depending on the relative position of disc with respect to the objective lens. The DOE focusing method works in a very similar manner, except that it uses two sets of knife-edge signals for differential calculation of the FES. This differential knife-edge principle makes the DOE focus servo more tolerant to the

positioning errors during fabrication process and more insensitive to the discrepancy in diffraction efficiencies of the two gratings in the DOE.

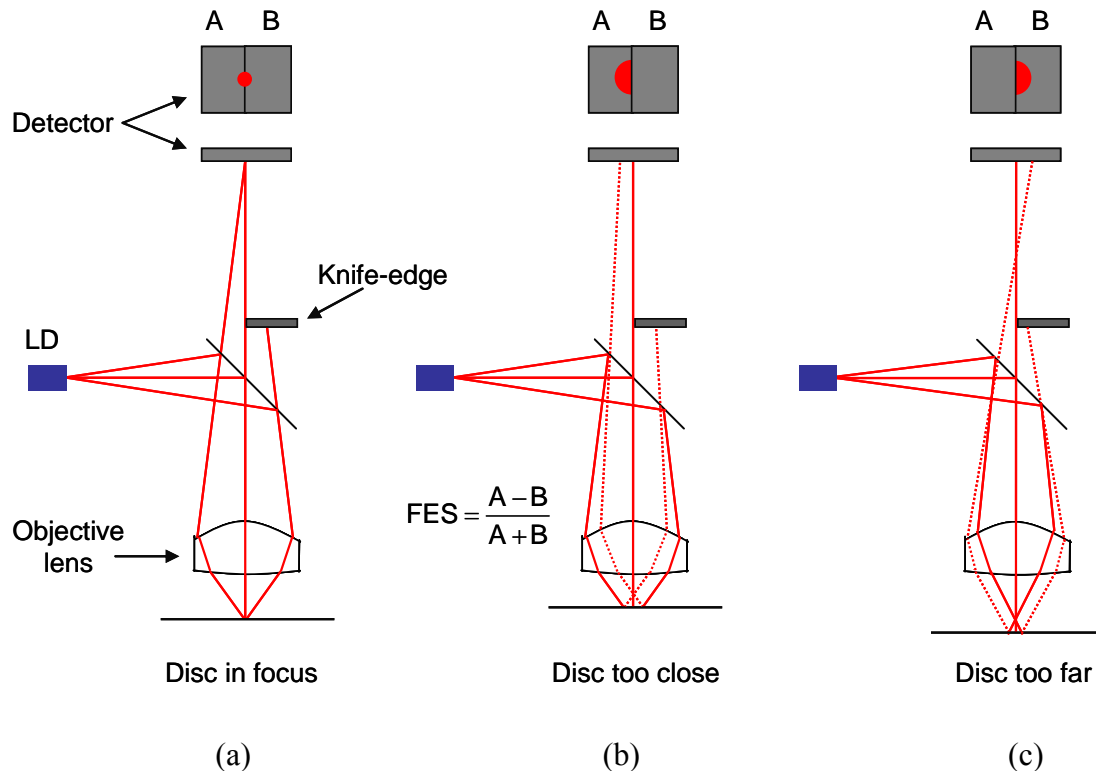


Figure 6.1 Knife-edge focusing method. (a) disc in focus ($FES= 0$), (b) disc too close to the objective lens ($FES> 0$) and (c) disc too far from the lens ($FES< 0$).

Figure 6.2 illustrates the mechanism of the DOE focusing method. With the data layer of a disc at the objective lens focal plane, the reflected beam is recollimated and directed to the focus sensor. The incident beam onto the DOE is diffracted, and the $+3^{\text{rd}}$ order beams are focused at the interface between detector cells A/B, and C/D, generating a zero FES. When the disc is too close to the objective lens, the 3^{rd} order beams are out of

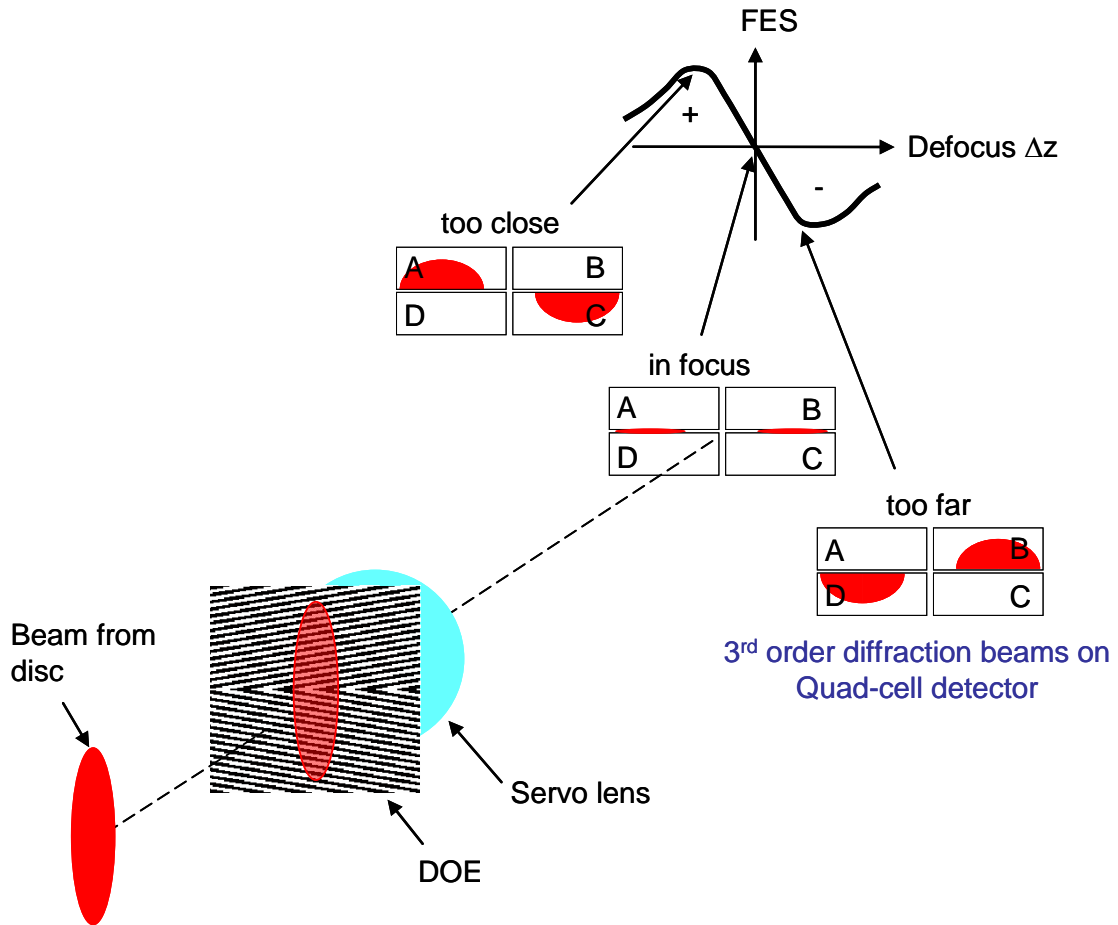


Figure 6.2 Mechanism of focus error signal generation. The reflected beam from a disc is incident on the DOE comprised of two slanted gratings, which produce two diffracted patterns. Only +3rd order beams fall on the quad-cell detector. Depending on the direction of defocus at the disc, the error signal becomes either positive or negative.

focus (converging) at the detector and generate a positive FES. In contrast, when the disc is too far from the objective lens, the defocused (diverging) 3rd order beams at the detector produce a negative FES.

The FES calculated in a servo electronic circuit is used to actuate to a voice coil that moves the objective lens in the axial direction. By repeating FES calculations and

corresponding lens movements in a closed-feedback loop, the 3rd order beams are kept focused on the detector during disc rotation, and focus errors are minimized. The zero FES ensures that the high power line beam is tightly focused on a data layer of the disc during the data destruction operation.

6.3 Design of DOE focus sensor

The DOE for the ODD system is comprised of two binary amplitude gratings slanted at angles with the same period, as drawn in Fig. 6.3(a). Grating I in the upper half slants with $+\theta_g$, and Grating II in the lower half slants with $-\theta_g$. In designing this DOE, the lens focal length, the grating period and the angle between the gratings are important design parameters, as well as the detector dimensions and the focus beam size at the detector. The values for the various design parameters should be carefully chosen to make sure that the focus sensor works properly. Throughout this design procedure, the full widths of the geometrical beam, calculated by the nominal HPLD aperture dimensions multiplied by magnifications of the imaging subsystem and the relay subsystem, are used as the size of the focused beam at the detector plane when the disc is in focus and denoted as W_x and W_y .

Figure 6.3(b) illustrates the diffraction pattern from Grating II at the quad-cell detector. The optical axis of the system is along the z -axis, and the location of the center of the m^{th} order beam (x_m, y_m) is governed by the servo lens focal length f_{servo} , the grating angle θ_g and the grating equation,

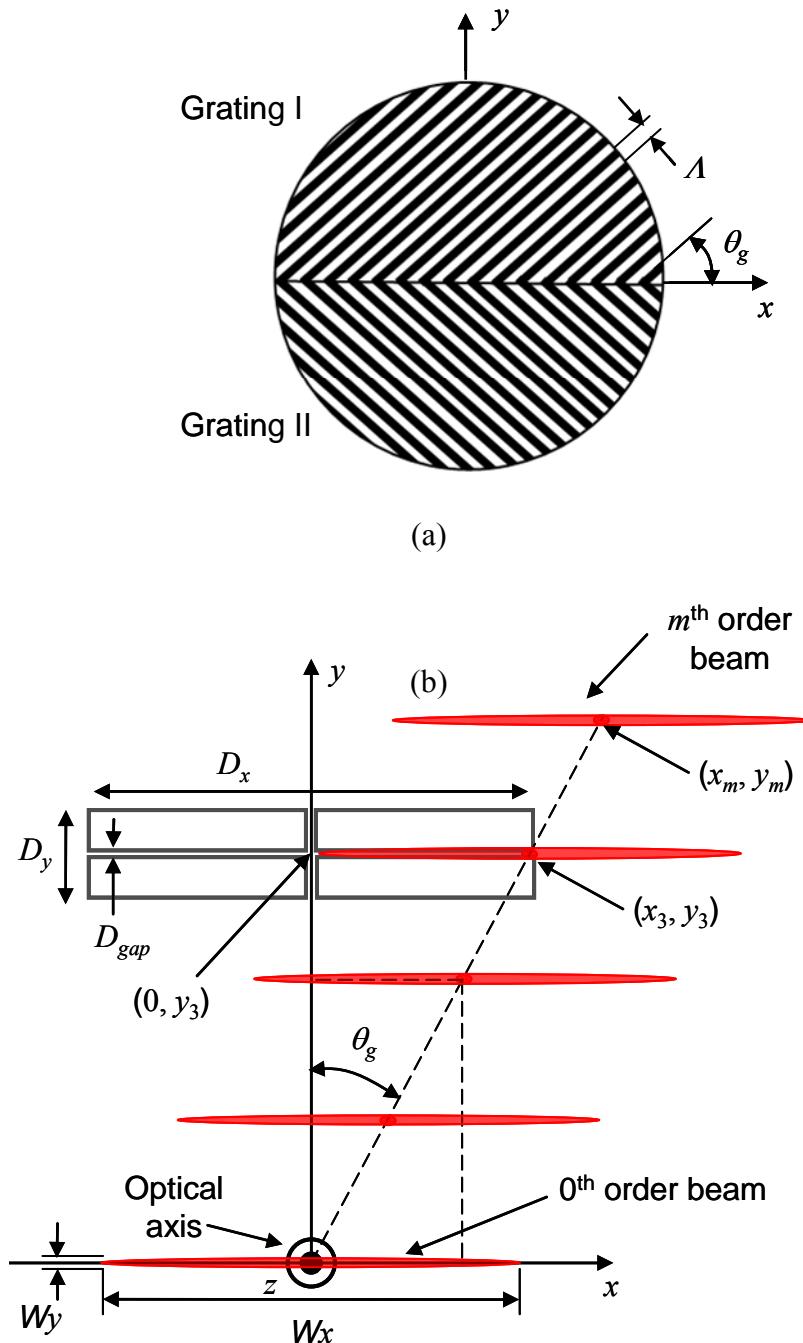


Figure 6.3 (a) Geometry of the DOE comprising two slanted gratings and (b) diffracted beams from Grating II as observed at the detector. Λ is the grating period, θ_g is the grating angle, the z -axis is the optical axis, and (D_x, D_y) are the dimensions of the quad-cell active area.

$$\sin \theta_m = m \frac{\lambda}{A} , \quad (6.4)$$

where λ is the wavelength of the light, A is the grating period, m is the grating diffraction order, and θ_m is the diffraction angle of the m^{th} order beam. Therefore, the center location of order m is

$$(x_m, y_m) = (f_{\text{servo}} \tan \theta_m \sin \theta_g, f_{\text{servo}} \tan \theta_m \cos \theta_g) . \quad (6.5)$$

The focused beam sizes at the detector are (W_x, W_y) with the disc in focus, and the quad-cell detector is centered at $(0, y_3)$ with the dimensions (D_x, D_y) .

Firstly, the center location of the $+3^{\text{rd}}$ order x_3 should be within the following range in order to avoid the two $+3^{\text{rd}}$ order beams from overlapping and to have the beam fall on the detector. The range for x_3 is

$$\frac{W_x}{2} < x_3 < \frac{D_x + W_x}{2} . \quad (6.6)$$

Secondly, it should be guaranteed that the $+3^{\text{rd}}$ orders used for focus sensing are not intervened by the adjacent $+2^{\text{nd}}$ and $+4^{\text{th}}$ order beams. The separation of the $+2^{\text{nd}}$ order from the $+3^{\text{rd}}$ order should be greater than $D_y/2$, which also ensures that the $+4^{\text{th}}$ order is separated the same distance from the $+3^{\text{rd}}$ order. That is,

$$|y_3 - y_2| > c D_y / 2 , \quad (6.7)$$

where c is a constant that scales the order separation and should be, at least, greater than one. At $c=1$, the $+2^{\text{nd}}$ and $+4^{\text{th}}$ orders lie on the bottom and top edges of the detector, respectively, and they are placed further away from the detector edges when $c>1$. Since the defocus at the disc significantly increases the beam width in the y direction, it is

recommended to have a value greater than two for c to avoid the influence of neighboring order beams when the disc is not in focus.

Thirdly, the F-number of the lens ($F/\#$) should be large enough for the focused beam width W_y to overfill the gap between detector cells D_{gap} . Since the y -axis beam width W_y is determined by the Airy disk diameter, this restriction becomes

$$W_y = 2.44\lambda(F/\#) > D_{gap} \quad . \quad (6.8)$$

This overfilling is required to prevent a slightly defocused beam from residing within the gap, producing a dead zone in the focus error signal that is insensitive to focus error [Marchant 1990].

Finally, the tradeoffs between the order separation and the difficulty of DOE fabrication need to be taken into consideration. Smaller Λ produces further separated orders, but the difficulty and cost of DOE fabrication is increased.

Due to the large number of free parameters, some of the design parameters are preselected based on availability of components, such as the quad-cell detector and the lens used in the focus sensor. Quad-cell detectors with proper dimensions have limited availability. A quadcell with an active area of 1.2×0.6 mm and an element gap of $10\mu\text{m}$ is chosen (Hamamatsu Corp. S6058). Since the diameter of the beam incident on the servo lens is approximately 4.1mm, $F/\# > 5.1$ and $f_{servo} > 20.5$ mm from Eq. (6.8). A plano-convex lens with focal length of 25.8mm ($F/\#=6.1$) is chosen (Melles-Griot 01LPX037). The $F/\#$ of 6.1 produces $W_y = 12\mu\text{m}$, which is slightly greater than the cell gap. The x -axis beam width W_x is 1.12mm, as calculated from the first-order magnifications and the LD output aperture width.

Replacing θ_m in Eq. (6.5) with $\theta_m = \sin^{-1}\left(m\frac{\lambda}{\Lambda}\right)$ from Eq. (6.4) yields

$$x_3 = f_{servo} \tan\left\{\sin^{-1}\left(m\frac{\lambda}{\Lambda}\right)\right\} \sin \theta_g \quad (6.9)$$

From Eqs. (6.6) and (6.9) with $m= 3$, the range for the grating angle θ_g as a function of Λ is obtained. That is,

$$\sin^{-1}\left(\frac{D_x}{2f_{servo} \tan\left\{\sin^{-1}(3\lambda/\Lambda)\right\}}\right) < \theta_g < \sin^{-1}\left(\frac{D_x + W_x}{2f_{servo} \tan\left\{\sin^{-1}(3\lambda/\Lambda)\right\}}\right) \quad (6.10)$$

This inequality is illustrated in Fig. 6.4(a) with the parameters $(D_x, D_y) = (1.2\text{mm}, 0.6\text{mm})$, $(W_x, W_y) = (1.12\text{mm}, 0.012\text{mm})$ and $f_{servo} = 25.8\text{mm}$. The shaded area represents the combination of Λ and θ_g satisfying Eq. (6.10).

Combining Eqs. (6.5) and (6.7) gives rise to

$$f_{servo} \cos \theta_g (\tan \theta_3 - \tan \theta_2) > c D_y / 2 \quad . \quad (6.11)$$

Manipulation of Eqs. (6.4) and (6.11) yields the inequality

$$\theta_g < \cos^{-1}\left(\frac{c D_y / 2}{f_{servo} [\tan\{\sin^{-1}(3\lambda/\Lambda)\} - \tan\{\sin^{-1}(2\lambda/\Lambda)\}]}\right) \quad . \quad (6.12)$$

Figure 6.4(b) shows the curves for $c= 1, 2, 3$ and 4 on top of Fig. 6.4(a), when the two sides in Eq. (6.11) are equal. The values for θ_g and Λ that satisfy Eqs. (6.10) and (6.11) are in the overlapped area between the shaded area and the area under the curve for a given c . It is recommended having $c > 2$, since defocus at the disc significantly increases the y -axis beam width at the detector. For the DOE used in the prototype ODD system, $\theta_g = 21^\circ$ and $\Lambda = 30.5\mu\text{m}$ are chosen with $c = 2.12$ to reduce the fabrication difficulty and

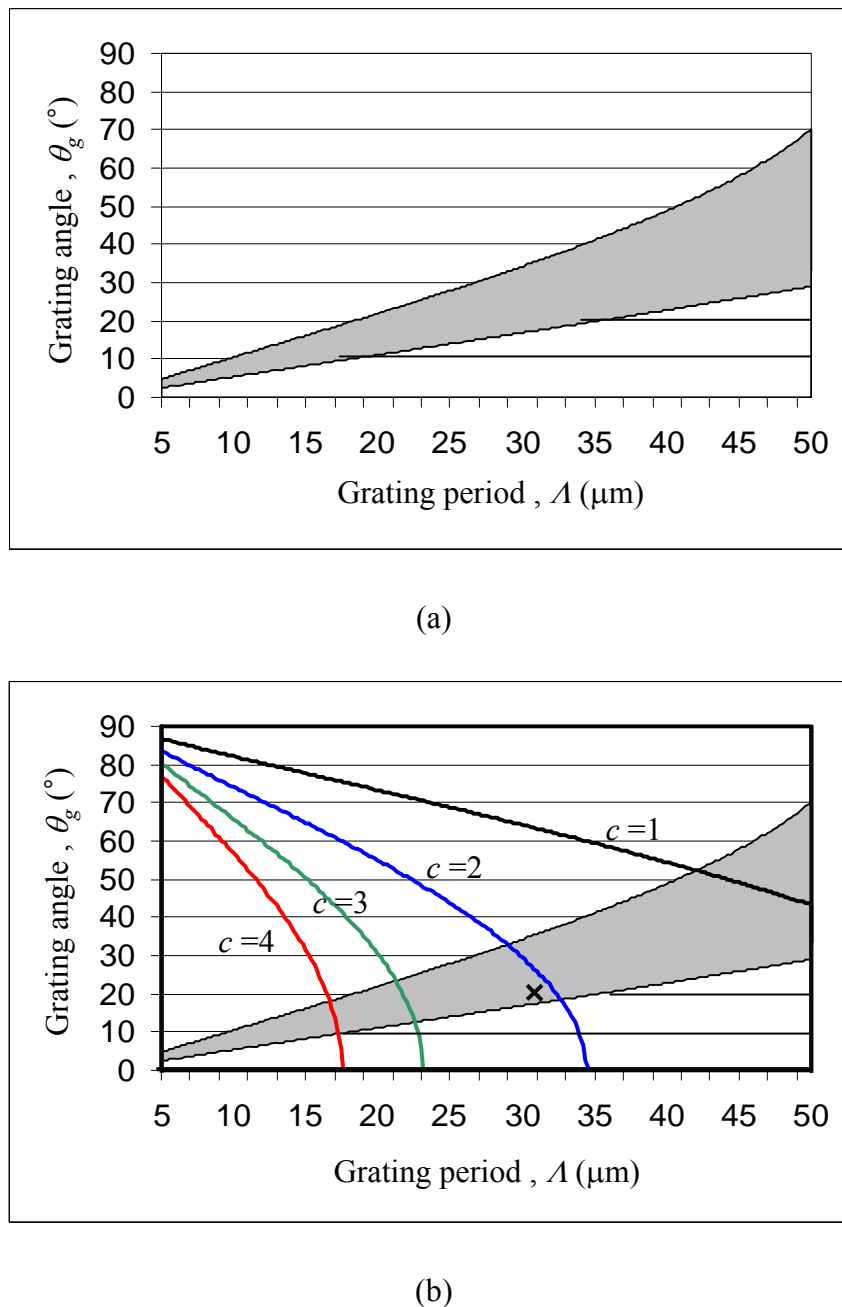


Figure 6.4 (a) The region of DOE design parameters (Λ, θ_g) that separate the two +3rd order beams in the x -axis are shaded, and (b) the curves for several c values that separate the +3rd orders from the other orders in the y -axis are overlapped with the shaded region in (a). The “x” mark in (b) indicates the selected parameters for the DOE for the prototype ODD system. See Section 6.3 for more details.

cost. The selected parameters are indicated by the “x” mark in Fig. 6.4(a) and summarized in Table 6.1.

Table 6.1 Selected design parameters for the DOE focus sensor.

Servo lens	f_{servo}	25.8 mm
Quad-detector	D_x	1.2 mm
	D_y	0.6 mm
DOE	θ_g	21 °
	Λ	30.5 μm
	a	0.5
Separation-scaling factor	c	2.12

In addition to having c greater than 2, the influence of the adjacent +2nd and +4th order beams is minimized by having 50% duty cycle of the gratings. Theoretically, the efficiencies into even diffraction orders are zero for 50% duty cycle binary gratings, as calculated from Eq. (5.2) with $a= 0.5$.

6.4 Fabrication of the DOE

6.4.1 Fabrication tool and procedure

A maskless lithography tool (MLT) that uses an Argon ion laser ($P_{\text{out}}= 4\text{W}$, $\lambda=351, 364, 380\text{nm}$) [Tamkin 2003] is used to fabricate the DOE for the ODD system. The UV beam is modulated by an acousto-optic deflector and focused onto a substrate that is coated

with UV-sensitive photoresist (PR). A single pulse duration corresponds to the pixel registration size of $2.1\mu\text{m}$. Scanning for writing a 2D pattern is achieved using a multi-faceted mirror (fast-scan) and a linear stage (slow-scan).

The pattern with two slanted gratings is designed using the parameters selected in Table 6.1. An 8-bit bitmap file containing the pattern information is used as input to the tool as a writing prescription. Then, the laser writer tool exposes the binary pattern onto a glass substrate coated with chrome and PR. By developing the exposed PR and etching out the chrome, the designed binary amplitude DOE is fabricated.

6.4.2 Problem with a single-step fabrication and solutions

Although the maskless lithographic method is advantageous in that no mask is needed for fabrication, a problem arises due to the digital representation of the pattern. The pixelation in a designed pattern is visible whenever the grating direction is different from the laser fast-scan or slow-scan directions, as in the slanted gratings of the DOE. As shown in Figs. 6.5(a) and (b), the pixelation in the designed DOE is transferred to the fabricated DOE. The stair-like line-edges in the microscope image of the fabricated DOE manifest the transferred pixelation. The pixelation produces unwanted diffraction patterns and scattering, causing a false focus error signal when used in the ODD system.

Two approaches are attempted to remove the pixilation effect. The first approach is to rotate the designed DOE pattern by the grating angle, θ_g as shown in Fig. 6.6(a). One grating is written in line with the fast-scan direction, and the other is at an angle with

the fast-scan direction but writing at the steep angle ($\theta = 2\theta_g$) might smoothen out the pixelation. Figures 6.6(b) and (c) show the fabricated gratings. Pixelation is completely eliminated in Grating I, but higher frequency wobbles are observed in Grating II. When illuminated with a laser beam, a few set of unwanted diffraction patterns are produced from Grating II. Unfortunately, some of the diffracted beams fall inside the active area of the quad-cell detector. Therefore, this approach does not solve the pixelation problem.

The other approach is contact-printing by using two masks and exposing the substrate twice. Firstly, the two bitmap files with each grating and two alignment marks are prepared to make two masks, as shown in Fig. 6.7(a). Each of the mask patterns is written on separate chrome substrates with the grating lines in the fast-scan direction of the MLT so that the two masks have straight line-edges with no high-frequency wobbles. After developing PR and etching chrome, the two binary amplitude masks are ready to be used to make the DOE. The chrome substrate for the DOE is placed behind Mask I for Grating I and exposed to uniform UV light ($\lambda=364\text{nm}$) through the mask. The pattern on Mask I is transferred to the DOE substrate after developing and etching. The DOE substrate has the pattern of Grating I and the alignment marks. The PR in the unexposed areas of the DOE substrate is undeveloped after the first fabrication step and used for contact-printing the pattern of Grating II onto the substrate. Mask II and the DOE substrate are aligned using the alignment marks under a microscope and glued together. Then exposure to UV light and the developing and etching processes transfer Grating II on the DOE substrate. The two alignment marks printed on the DOE substrate after the second exposure are shown in Fig. 6.7(b). Figure 6.7(c) presents the image of the

fabricated DOE along with the microscopic images of the regions near the grating boundary. The edges of grating lines are straight with no high frequency wobbles, and no unwanted diffraction patterns are observed when illuminated by a collimate HeNe laser beam, as shown in Fig. 6.8. The light that passes Gratings I and II generates the diffraction patterns I and II, respectively.

The quad-cell photodiode is aligned such that the two +3rd order diffraction beams from each grating are used for focus sensing. The diffraction efficiencies of each grating in the fabricated DOE are provided in Table 6.2. The two gratings have efficiencies close to the theoretical efficiencies. The slight difference in the diffraction efficiencies is of little concern due to the differential calculation of the focus error signal.

Table 6.2 Measured efficiencies of diffraction orders from the gratings in the fabricated DOE and theoretical diffraction efficiencies from an ideal binary amplitude grating.

	Measured Efficiency (%)		Theoretical Efficiency (%)
Diffraction Order	Grating I	Grating II	Ideal grating
0	20	17.4	25
1	10	10.4	10.1
2	0.4	0.4	0
3	1.1	1.2	1.1
4	0.3	0.3	0

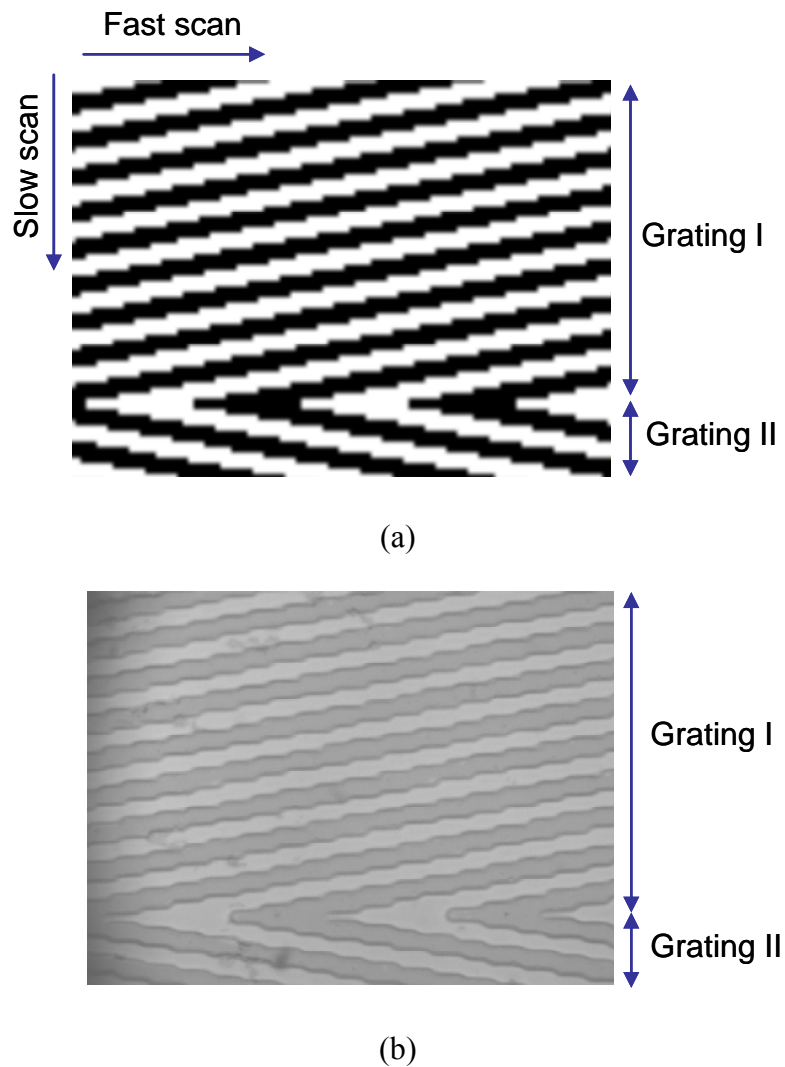


Figure 6.5 (a) Designed DOE in a bitmap representation and (b) microscopic image of the fabricated DOE on a glass substrate. Pixelation in the designed DOE is apparently transferred to the fabricated DOE. Pixelation results from the bit-wise representation of the pattern and generates unwanted diffraction patterns.

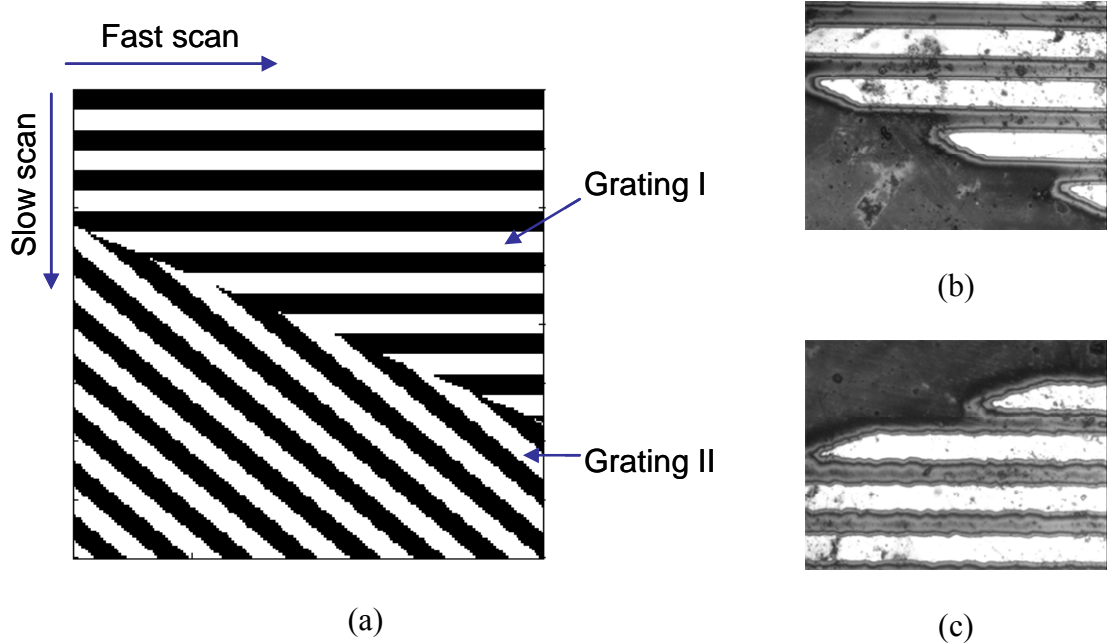


Figure 6.6 The first approach to solve the pixelation problem. (a) The designed DOE pattern is rotated by the grating angle so that Grating I is written along the laser fast-scan direction and Grating II is written at a steep angle of twice the grating angle. Images of the fabricated Grating I (b) and Grating II (c). Pixelation is completely removed from Grating I, but not from Grating II (c).

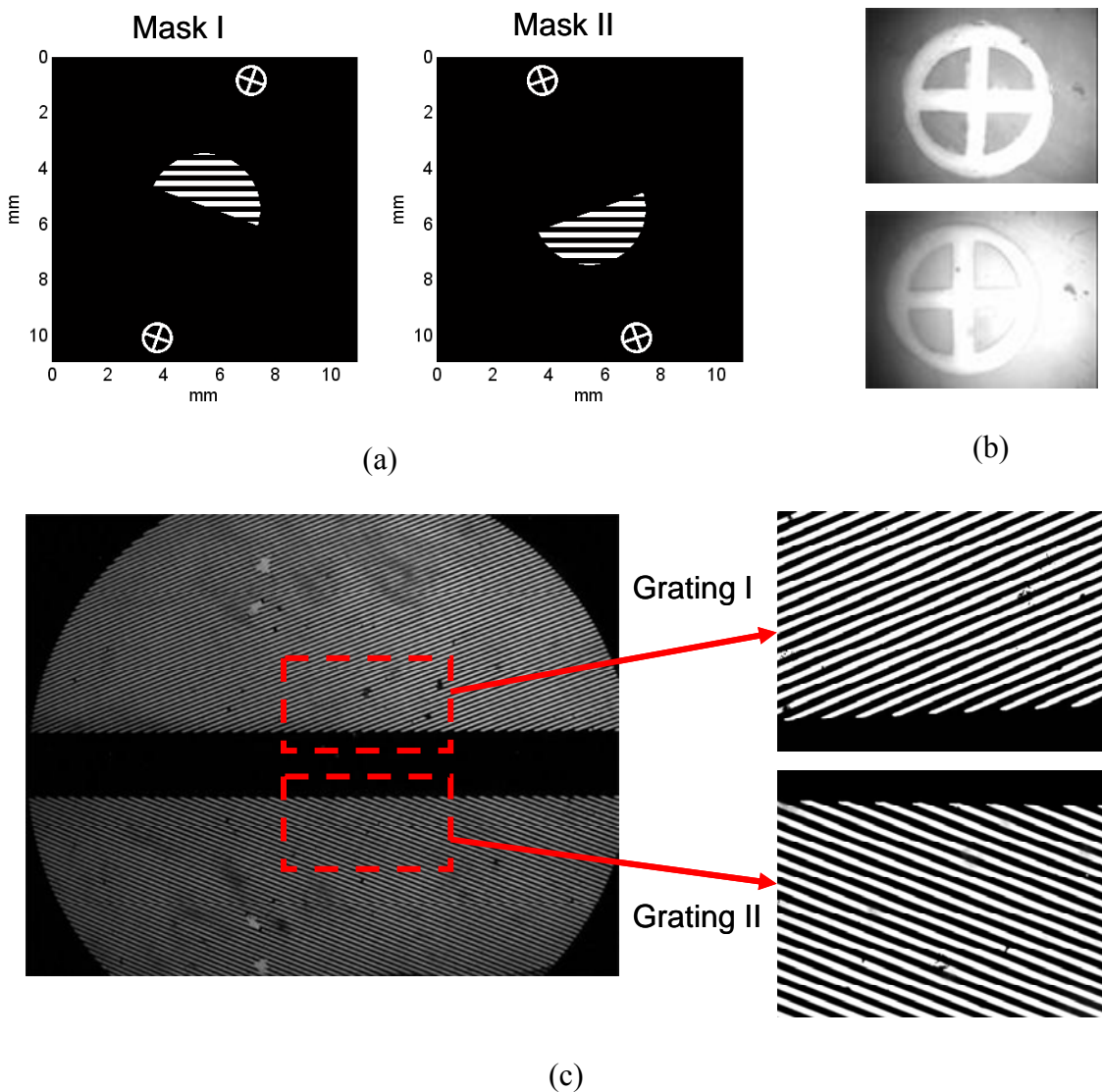


Figure 6.7 The second approach to solve the pixelation problem. (a) Bitmap representation of Masks I and II for Gratings I and II and alignment marks. Both gratings are written in the fast-scan direction so that the line-edges are straight. (b) Images of alignment marks printed on the DOE substrate after double exposure. (c) Fabricated DOE ($\Lambda = 30.5\mu\text{m}$, $\theta_g = 42^\circ$) on a chrome substrate. A microscopic image of the region near the grating boundary is also provided

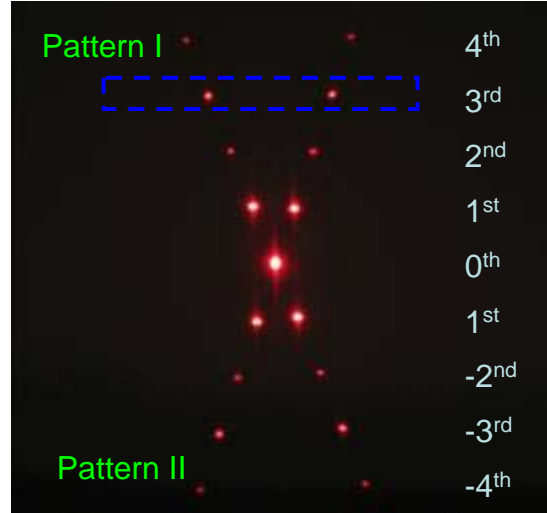


Figure 6.8 Picture of diffraction patterns of the DOE fabricated in the two-step method when illuminated by a collimated HeNe laser beam. Patterns I and II are generated from Gratings I and II, respectively. No unwanted diffraction patterns are present due to straight line edges of the gratings. The 3rd order beams are used for focus sensing.

6.5 Simulation of the ODD system

Optical properties of the beam emitted from the 4-watt HPLD used in the ODD system are similar to those of the 1-watt HPLD beam discussed in Chapter 4. The strongly elliptical HPLD beam is close to a Gaussian beam along the fast axis but has multiple lateral eigenmodes in the slow axis, which generates a nearly top-hat far-field irradiance profile along the slow axis during high-power operation. Therefore, the LDRT method described in Chapter 4 is used for modeling this HPLD beam in the ODD system. Figure 6.9(a) presents a layout of the imaging subsystem (from the source to the disc) of the ODD system in the LDRT model and traces of rays launched from the source. The fast axis of the HPLD is perpendicular to the plane of the drawing. A number of rays with the

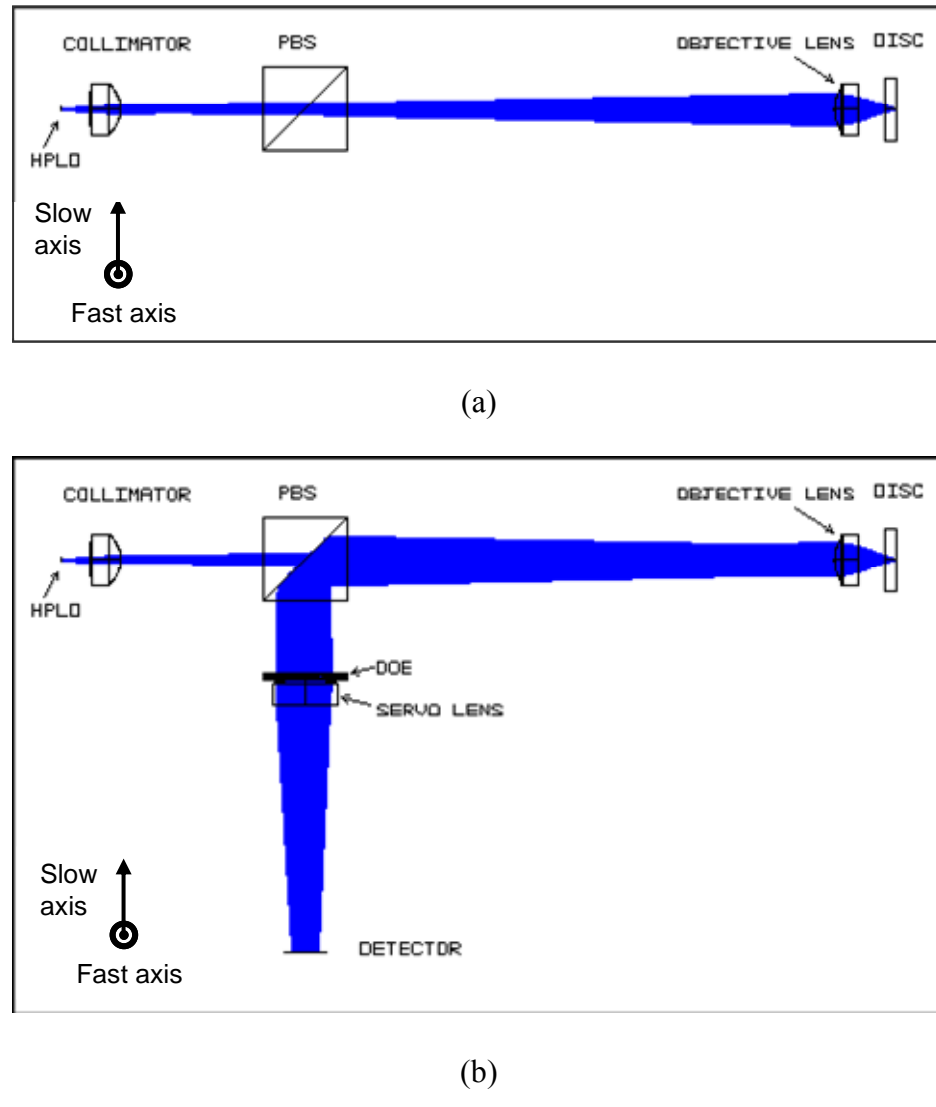


Figure 6.9 Layouts of (a) the imaging subsystem with traces of rays from the source to the disc and (b) the whole ODD system with traces of rays from source to disc and to detector in the non-sequential raytracing (LDRT) model.

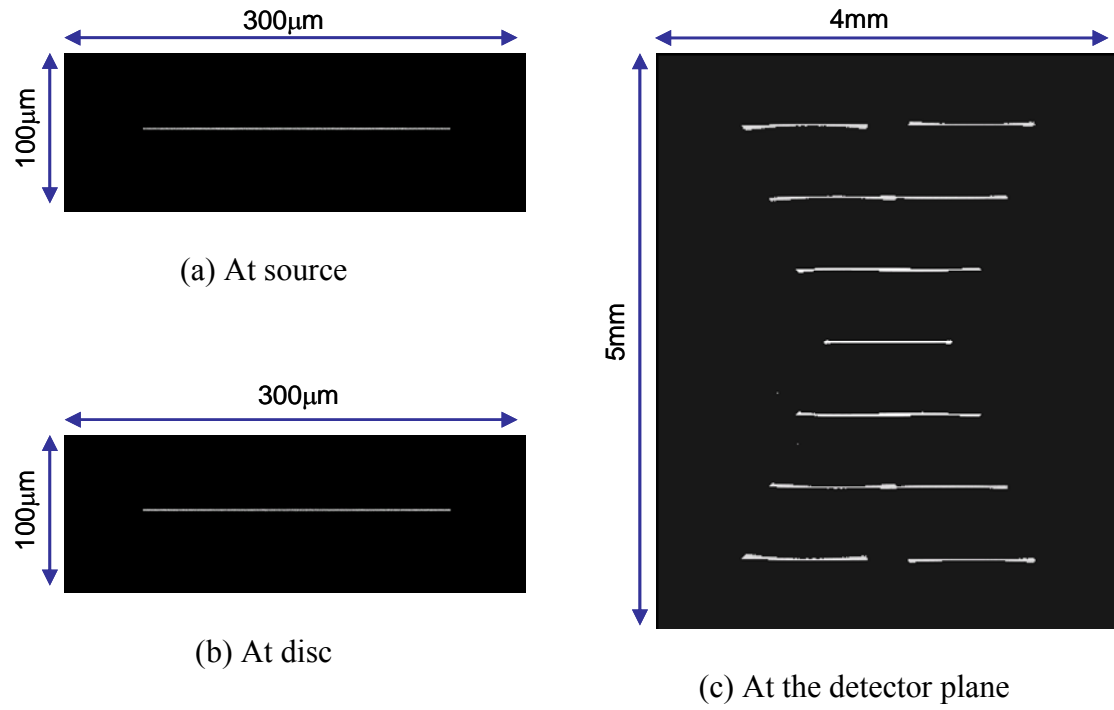


Figure 6.10 Grayscale transverse irradiances of rays simulated using an LDRT method at the source, the disc, and the detector plane. The irradiance distribution in (c) is plotted in log-scale to show all the present diffraction orders regardless of their diffraction efficiency.

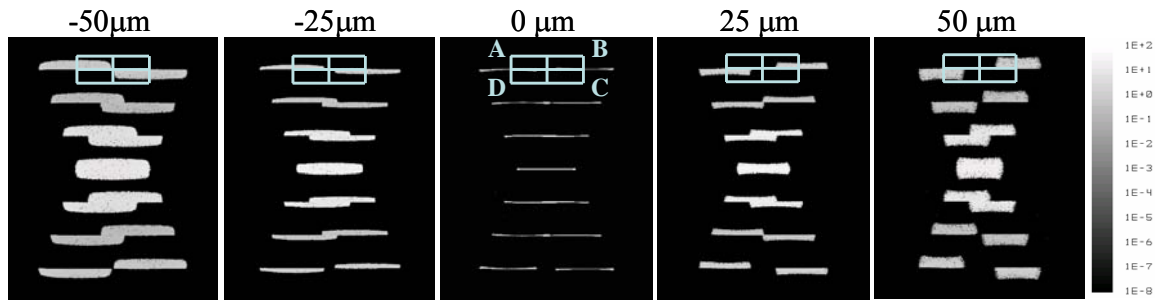


Figure 6.11 Simulated diffraction patterns on the detector plane with defocus at the disc obtained using the LDRT method. The irradiance distribution is plotted in log-scale to show all the present diffraction orders regardless of their diffraction efficiency. The size of observation window is 4 × 5 mm, and a quad-cell detector (1.2 × 0.6 mm) is drawn to have the +3rd orders on it.

top-hat angular distribution (full angles of 10° and 34°) are launched from a rectangular area of $200 \times 1\mu\text{m}$. Figures 6.10(a) and (b) show the grayscale irradiance distributions at the source and the disc, respectively, in the area of $300 \times 100\mu\text{m}$. The rays that are launched from the source, reflected from the disc and arriving at the detector plane are shown in Fig. 6.9(b) along with the whole ODD system layout. The transverse irradiance distribution at the detector plane ($4 \times 5\text{mm}$) is illustrated in Fig. 6.9(c). The distribution is plotted in log-scale in order to show both the intense 0^{th} and 1^{st} orders and the weak 2^{nd} and 3^{rd} orders. Due to the DOE comprising two angled gratings, two sets of diffraction patterns are produced.

6.6 Simulation and characterization of DOE focus servo

The LDRT model of the ODD system is used to simulate the beam distributions at the detector plane and the FES as the disc goes through the focal plane of the objective lens. A total of 100000 rays emanating from the source are used in each simulation. The measured diffraction efficiencies of each order in Table 6.2 are used for scaling the diffraction order contributions from the DOE. Figure 6.11 shows the irradiance of the diffracted beams on the detector plane ($4 \times 5\text{ mm}$) along with a quad-cell detector as defocus at disc Δz varies $-50\mu\text{m}$ to $50\mu\text{m}$. The irradiance distribution is plotted in a log scale so that all the orders are visible despite the significant difference in their efficiencies. The irradiance distributions exhibit that the DOE focus sensor works as envisioned in Fig. 6.2. Note that the horizontal beam width gets narrower as Δz increases,

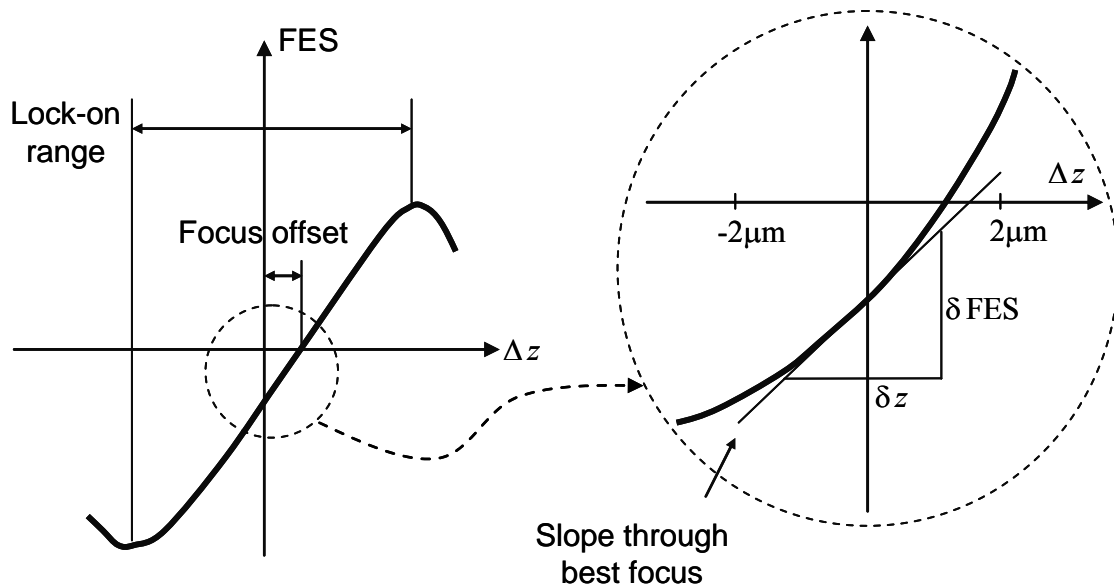


Figure 6.12 A typical FES is drawn along with several performance parameters of a focus servo, which are the slope through best focus, lock-on range, linearity within $\pm 2\mu\text{m}$ and focus offset.

indicating systematic astigmatism.

More comprehensive study on the characteristics of the DOE focus servo is done by evaluating simulated FES signals in the following paragraphs. Figure 6.12 illustrates several important parameters that quantify the performance of a focus servo, which are slope through best focus ($\alpha = \delta\text{FES} / \delta z$), symmetric lock-on range about best focus, degree of linearity within $\pm 2\mu\text{m}$ of best focus and focus offset [Wang and Milster 1993]. In general, a steep slope, a large lock-on range, a high degree of linearity, and no focus offset are desired. Performance parameters are determined by optical system design, DOE design, detector geometry, and errors in fabrication and alignment.

FES signals are generated for a short defocus range ($|\Delta z| < 50\mu\text{m}$) and a long

defocus range ($|\Delta z| < 1\text{mm}$). The FES over the short range is used to study the performance of the focus sensor near best focus, and the long-range FES is used to examine the signal behavior during the focus search mode.

To generate the short-range FES, 101 separate raytracing simulations are performed with a defocus step of $1\mu\text{m}$. One-hundred-one sets of detector signals, A, B, C and D are produced by incoherently summing the power carried by rays arriving at the detector cells. The normalized FES is calculated using Eq. (6.3). Figures 6.13(a) and (b) show the two summed detector signals (A+C and B+D) and the normalized FES as a function of Δz . The slope through best focus is $0.282\mu\text{m}^{-1}$, and the lock-on range is greater than $12\mu\text{m}$. The linearity is defined as rms departure of the normalized FES from a line of best fit, and a small value of linearity means the FES is straighter. The degree of linearity is 0.023. The focus offset is zero. These simulated performance parameters are summarized in Table 6.3.

For generation of the long-range FES, four detector signals are generated from 201 separate raytracing simulations with a defocus step of $10\mu\text{m}$. Figures 6.14(a), (b) and (c) show four detector signals, summed detector signals and the normalized FES as a function of Δz . The FES of the DOE focus servo is different from a typical FES of a conventional focus servo in a few distinct ways. In addition to crossing of signals at $\Delta z = 0$, each detector signal has three bumps at the positive side of Δz , as shown in Fig. 6.14(a), and there is a hump in the normalized FES at around $250\mu\text{m}$, as shown in Fig. 6.14(c). The humps in Figs. 6.14(a)-(c) at the positive Δz originate from the influence of diffraction orders other than the 3rd order. As the disc moves away from the objective lens

($\Delta z > 0$), the vertical beam widths of the 2nd, 1st and 0th order beams at the detector plane increase so that they intrude into the detector cells. Their influence is greater on signals C and D than on the signals A and B, since beam irradiance falling on the detector cells C and D that are closer to the lower orders ($m = 0, 1, 2$) is greater. Also, the successive intrusion of the 2nd, 1st and 0th order beams are exhibited by the multiple peaks in the hump, as indicated in Fig. 6.14(a). Despite the different levels of influence of each mode on the detector cells, the humps of the summed signals of cells in diagonal positions in Fig. 6.14(b) are nearly of the same amplitude. The crossing of the two signals at $\Delta z = 200\mu\text{m}$ in Fig. 6.14(b) occurs because the beam reflected from the disc is focused before hitting the DOE and the diffraction pattern is flipped upside down at $\Delta z > 200\mu\text{m}$. Therefore, another zero-crossing other than at the best focus ($\Delta z = 0\mu\text{m}$) appears during the focus search mode, as shown in Fig. 6.14(c).

Table 6.3 Simulated performance parameters of the DOE focus servo

Performance parameters	Values
Slope through best focus (μm^{-1})	0.2824
Lock-on range (μm)	> 12
Linearity within $\pm 2\mu\text{m}$	0.0229
Focus offset (μm)	0

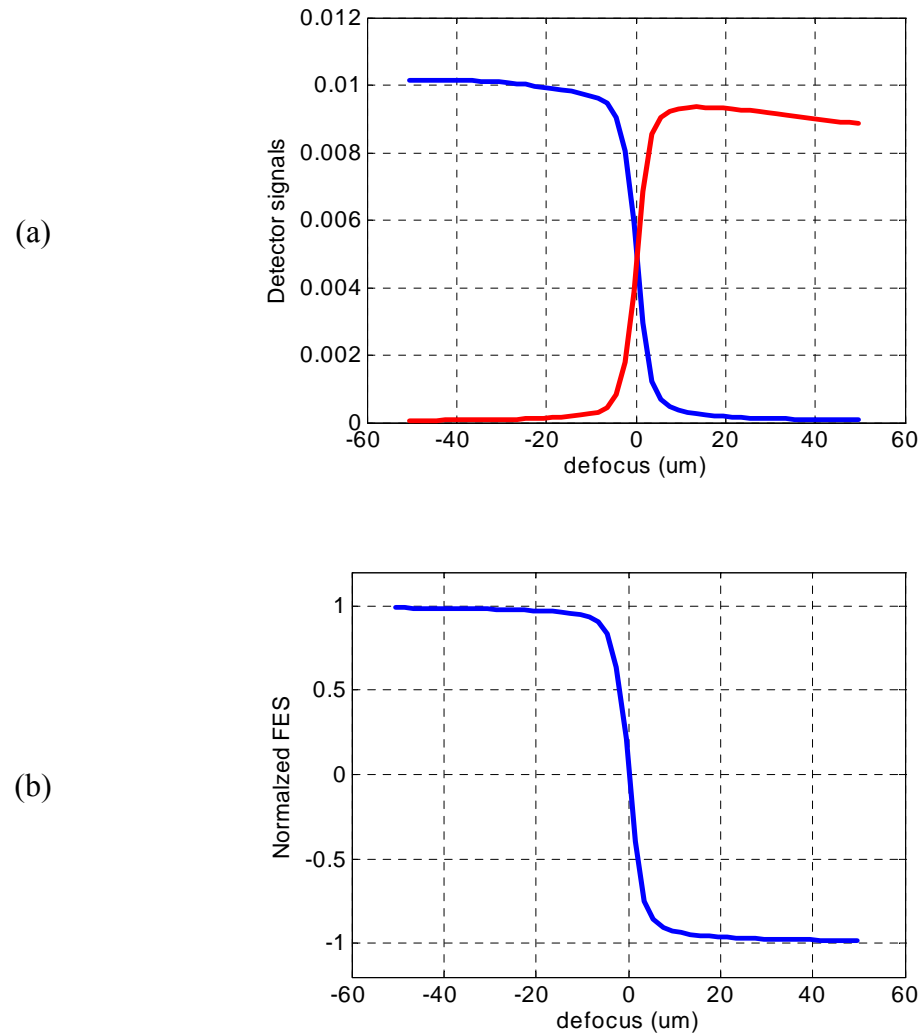


Figure 6.13 Simulated signals as a function of defocus at disc ($|\Delta z| < 50\mu\text{m}$). (a) Two summed detector signals (A+C, B+D) and (b) a normalized FES.

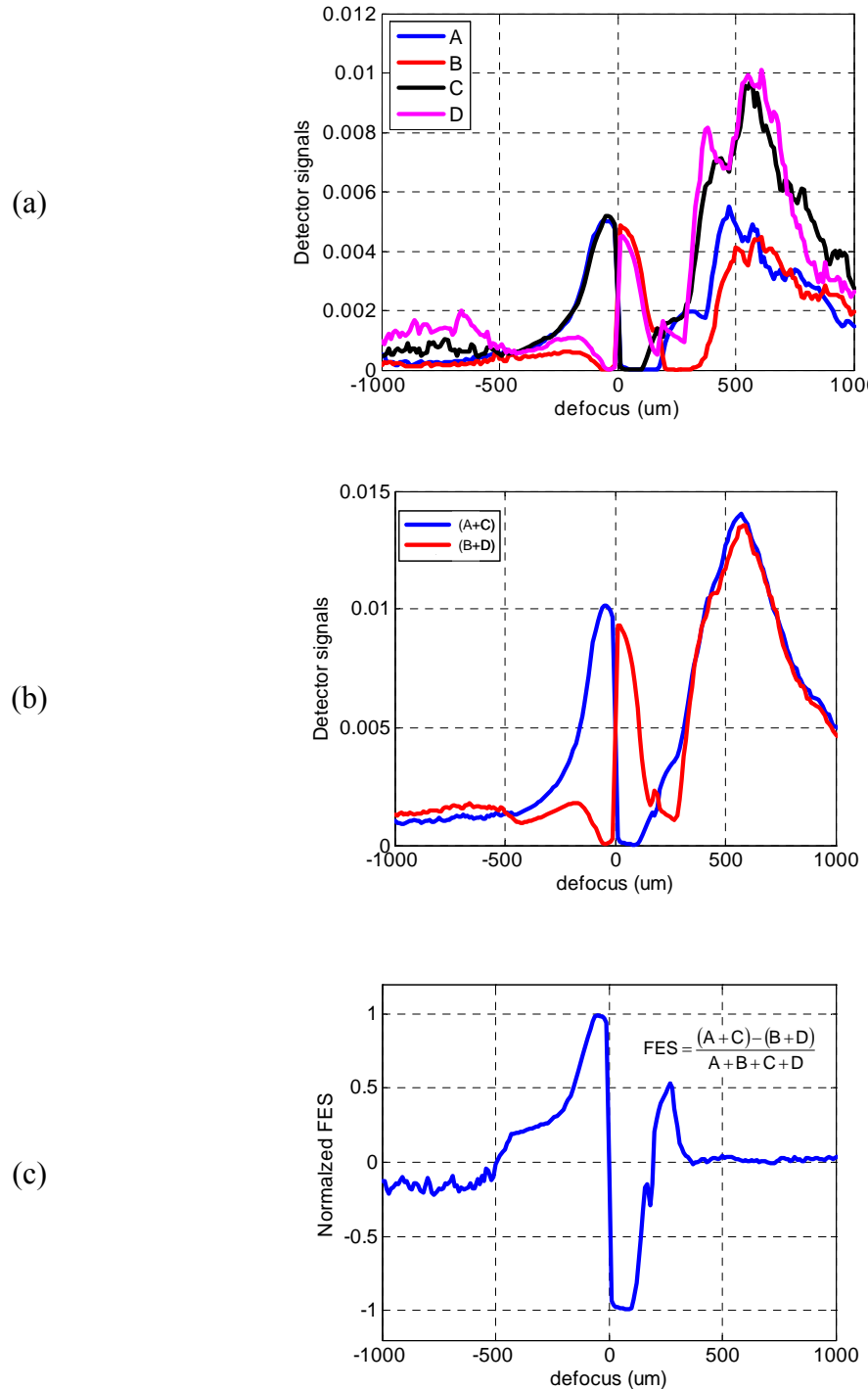


Figure 6.14 Simulated signals as a function of defocus at disc ($|\Delta z| < 1\text{mm}$). (a) Four detector signals (A, B, C, D), (b) two summed detector signals (A+C, B+D) and (c) a normalized FES.

6.7 Error sources and tolerance analysis

The ideal performance of the DOE focus servo is presented in Table 6.3. In a real system, however, there is always a certain amount of errors in fabrication of elements or construction of systems that deteriorate performance. Therefore, the errors and associated tolerances should be estimated as a part of the design process.

In this section, the performance degradation of the DOE servo is affected by misalignment of the HPLD, the DOE and the detector. Considered are four probable error sources related to alignment:

- 1) tilt of the HPLD about the z axis;
- 2) tilt of the DOE about the z axis;
- 3) decenter of the detector in the x axis; and
- 4) decenter of the detector in the y axis.

The LDRT model is used to simulate the FES signals in the presence of each individual error source. Firstly, the specific element is perturbed in the LDRT model by rotating or decentering with all the other components remaining ideal. Secondly, a number of separate raytracing simulations using 10000 rays each are performed to produce a set of four detector signals. One-hundred-one simulations are done for the short defocus range ($|\Delta z| < 50\mu\text{m}$) and 201 simulations for the long defocus range ($|\Delta z| < 1\text{mm}$). Finally, the normalized FES signals are generated from the detector signals using Eq. (6.3), and the performance parameters, such as slope through FES zero-crossing, linearity within $\pm 2\mu\text{m}$ of the FES zero-crossing and focus offset are evaluated. Note that the lock-on range is omitted due to ambiguity in determining the distinct range when the FES is

significantly distorted due to perturbation.

Figures 6.15 and 6.16 show the detector signals and the normalized FES signals for the HPLD tilt angles of $\theta_{LD} = -2^\circ, -1^\circ, 0^\circ, 1^\circ$ and 2° in the short defocus range, and for $\theta_{LD} = -4^\circ, -2^\circ, 0^\circ, 2^\circ$ and 4° in the long defocus range, respectively. Table 6.4 provides change in the performance parameters upon the perturbation. The major influence of tilt in the HPLD is the shift in the zero-crossing of the FES, which implies that the servo locks the focus outside the best focus by the amount of the focus offset. For the depth of focus of $1.6\mu\text{m}$, tolerance of the tilt angle of the HPLD is about $\pm 0.3^\circ$. Also, the slope of the FES is reduced by one-third at the tilt angle of $\pm 2^\circ$. The degree of linearity is evaluated within $\pm 2\mu\text{m}$ of zero-crossings of the FES signals.

The detector signals and the normalized FES signals are provided in Figs. 6.17 and 6.18 when the DOE is tilted about z axis by an angle $\theta_{DOE} = -2^\circ, -1^\circ, 0^\circ, 1^\circ$ and 2° in the range of $|\Delta z| < 50\mu\text{m}$, and for $\theta_{DOE} = -4^\circ, -2^\circ, 0^\circ, 2^\circ$ and 4° in the range of $|\Delta z| < 1\text{mm}$, respectively. It is clearly observed from the normalized FES signals that significant focus offsets are introduced and the signals become distorted due to tilt of the DOE. The performance parameters are evaluated from the FES and provided in Table 6.5. Focus offsets are the main problem associated with misalignment of the DOE. Tolerance of the DOE tilt angle is 0.18° for a system with depth of focus of $1.6\mu\text{m}$.

The influence of decenter of the quad-cell detector in the x and y axes on the FES is analyzed. Figures 6.19 and 6.20 show how detector signals and the FES signals change when the x -decenter Δx is $-40\mu\text{m}, 20\mu\text{m}, 0\mu\text{m}, 20\mu\text{m}$ and $40\mu\text{m}$. Although the individual detector signals deviate from the ideal-case ($\Delta x = 0\mu\text{m}$) signals, there is little degradation

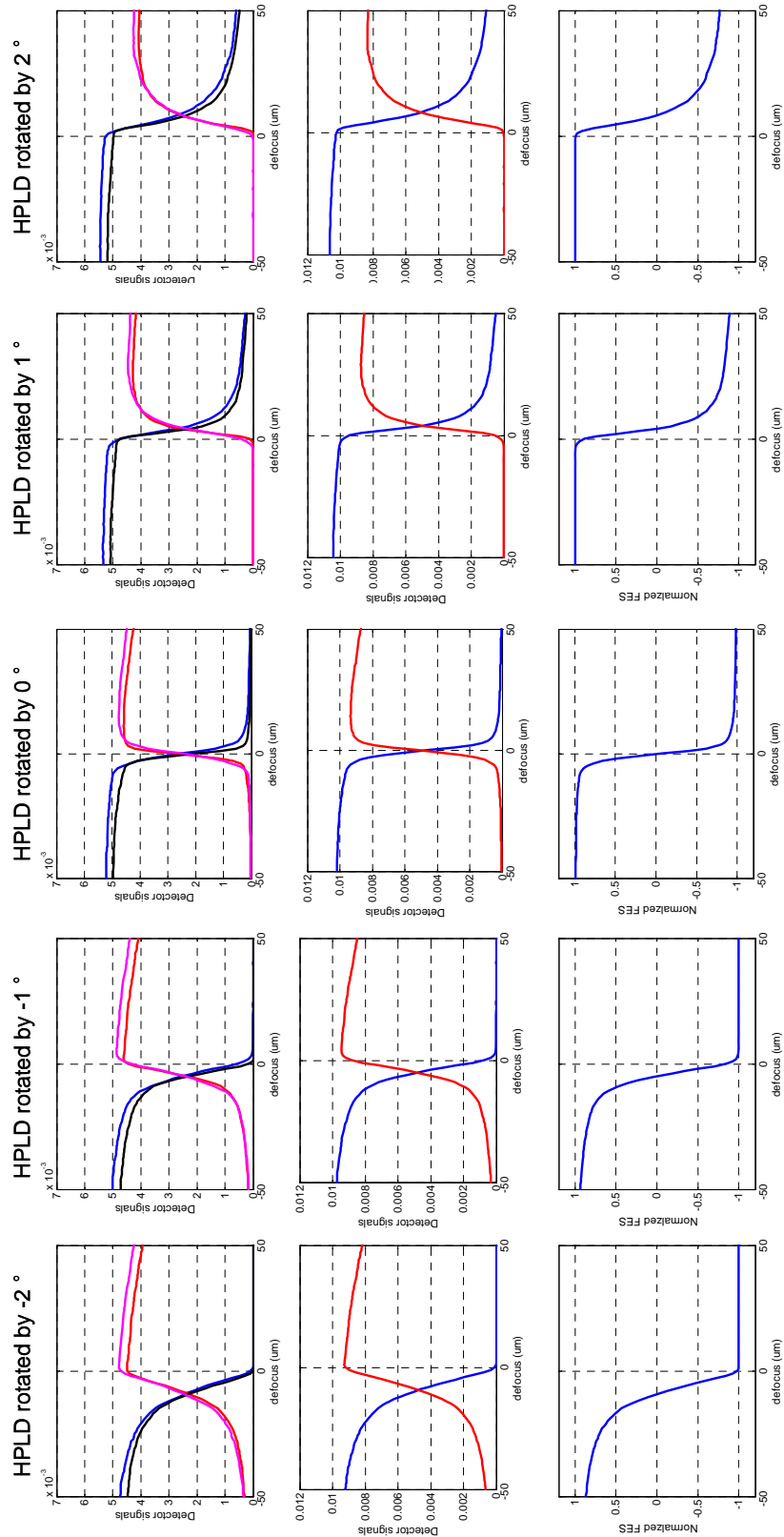


Figure 6.15 Simulated signals when the HPLD is rotated about the z axis ($|\Delta z| < 50\mu\text{m}$). The first row shows four detector signals (A, B, C, D), the second row shows two summed detector signals (A+C, B+D) and the bottom row shows normalized FES signals.

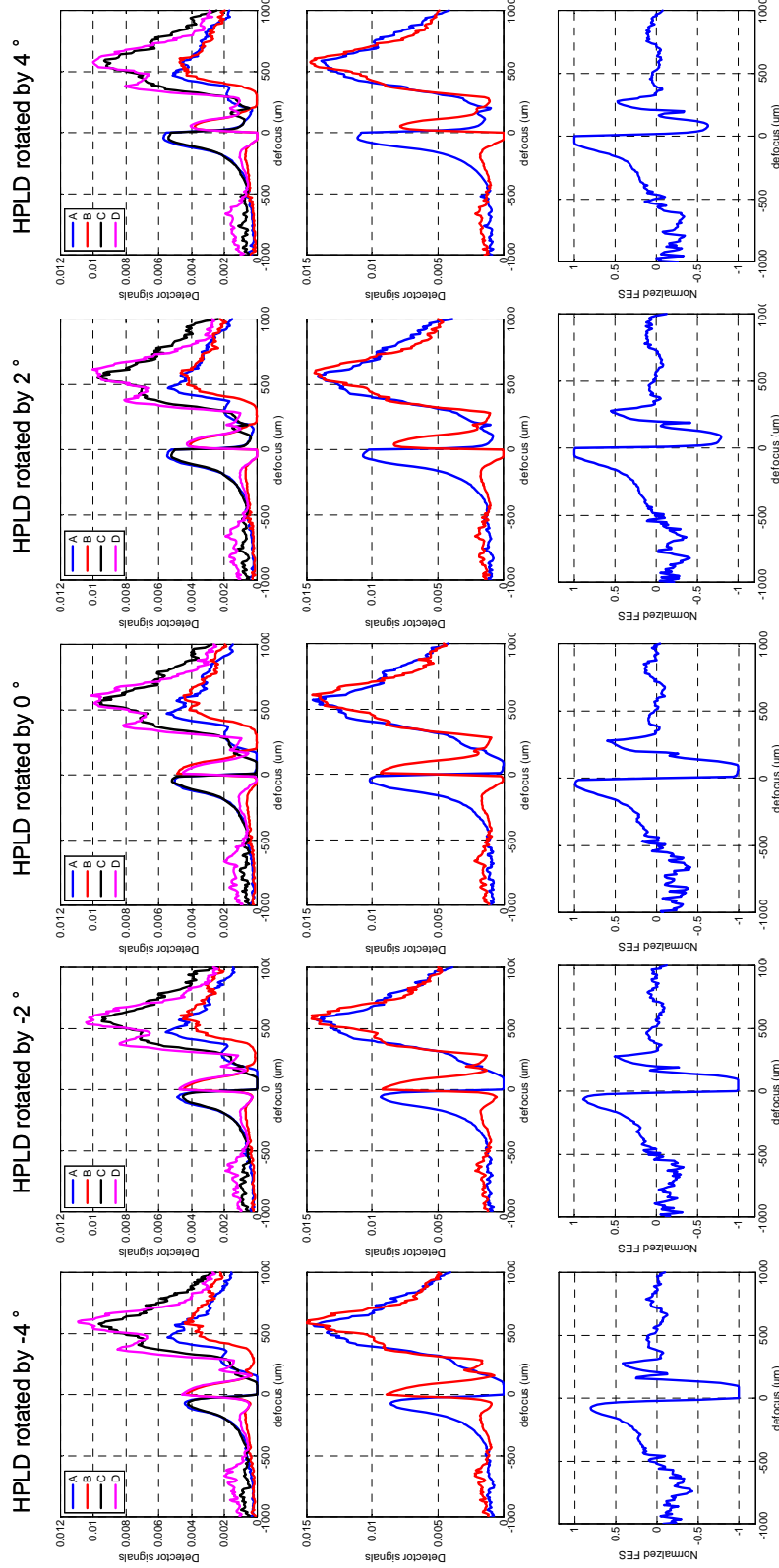


Figure 6.16 Simulated signals when the HPLD is rotated about the z axis ($|\Delta z| < 1\text{mm}$). The first row shows four detector signals (A, B, C, D), the second row shows two summed detector signals (A+C, B+D) and the bottom row shows normalized FES signals.

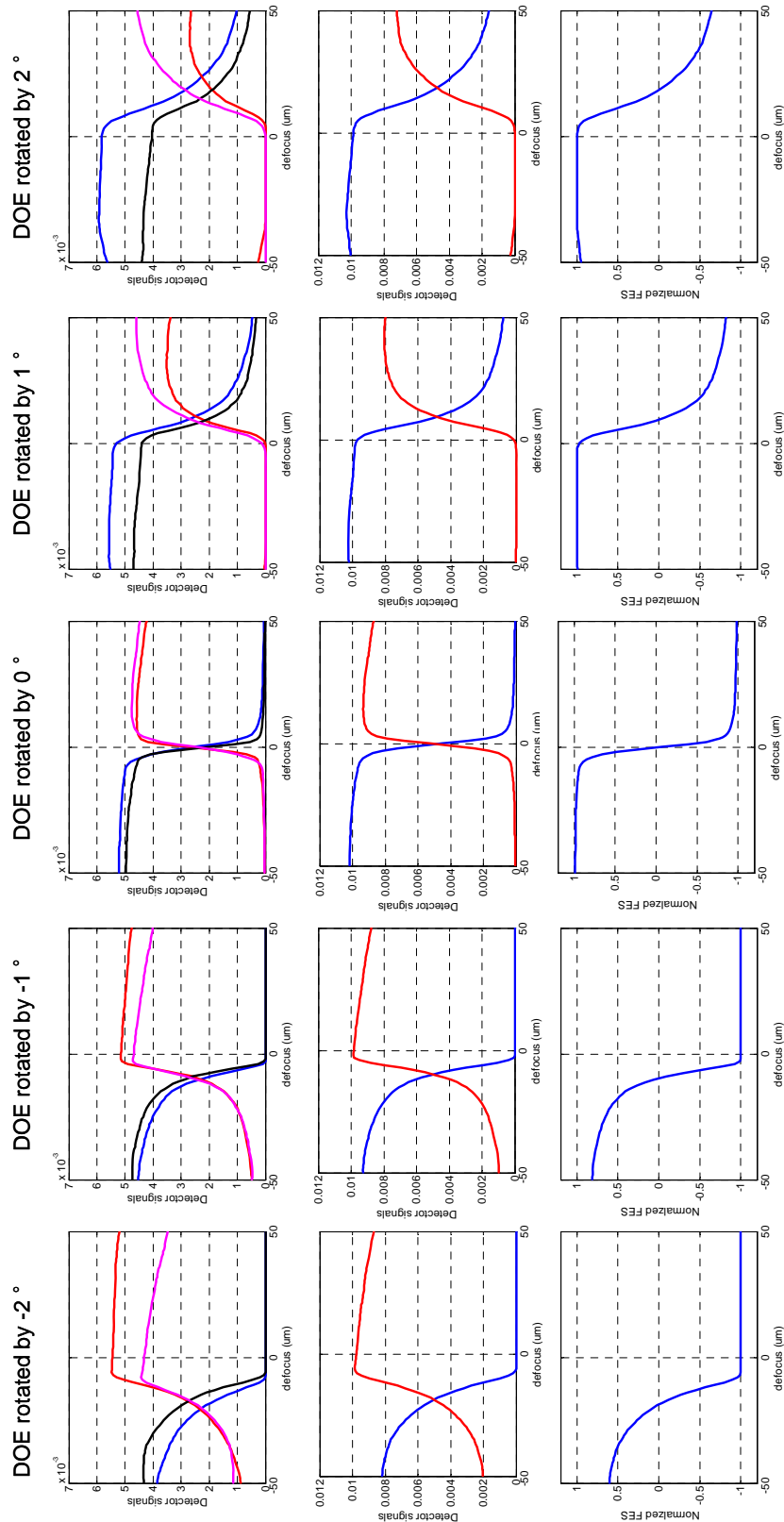


Figure 6.17 Simulated signals when the DOE is rotated about the z axis ($|\Delta z| < 50\mu\text{m}$). The first row shows four detector signals (A, B, C, D), the second row shows two summed detector signals (A+C, B+D) and the bottom row shows normalized FES signals.

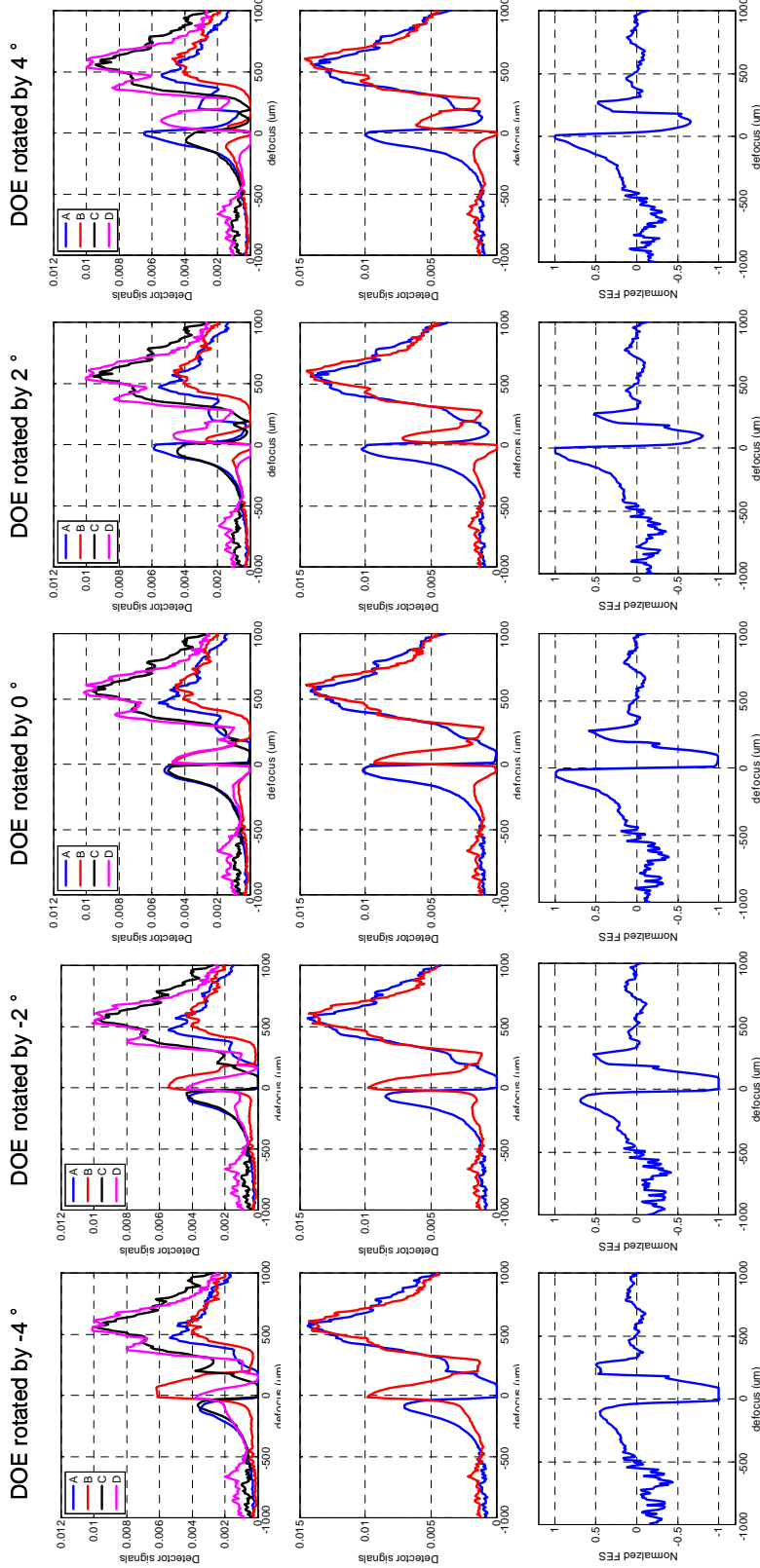


Figure 6.18 Simulated signals when the DOE is rotated about the z axis ($|\Delta z| < 1\text{mm}$). The first row shows four detector signals (A, B, C, D), the second row shows two summed detector signals (A+C, B+D) and the bottom row shows normalized FES signals.

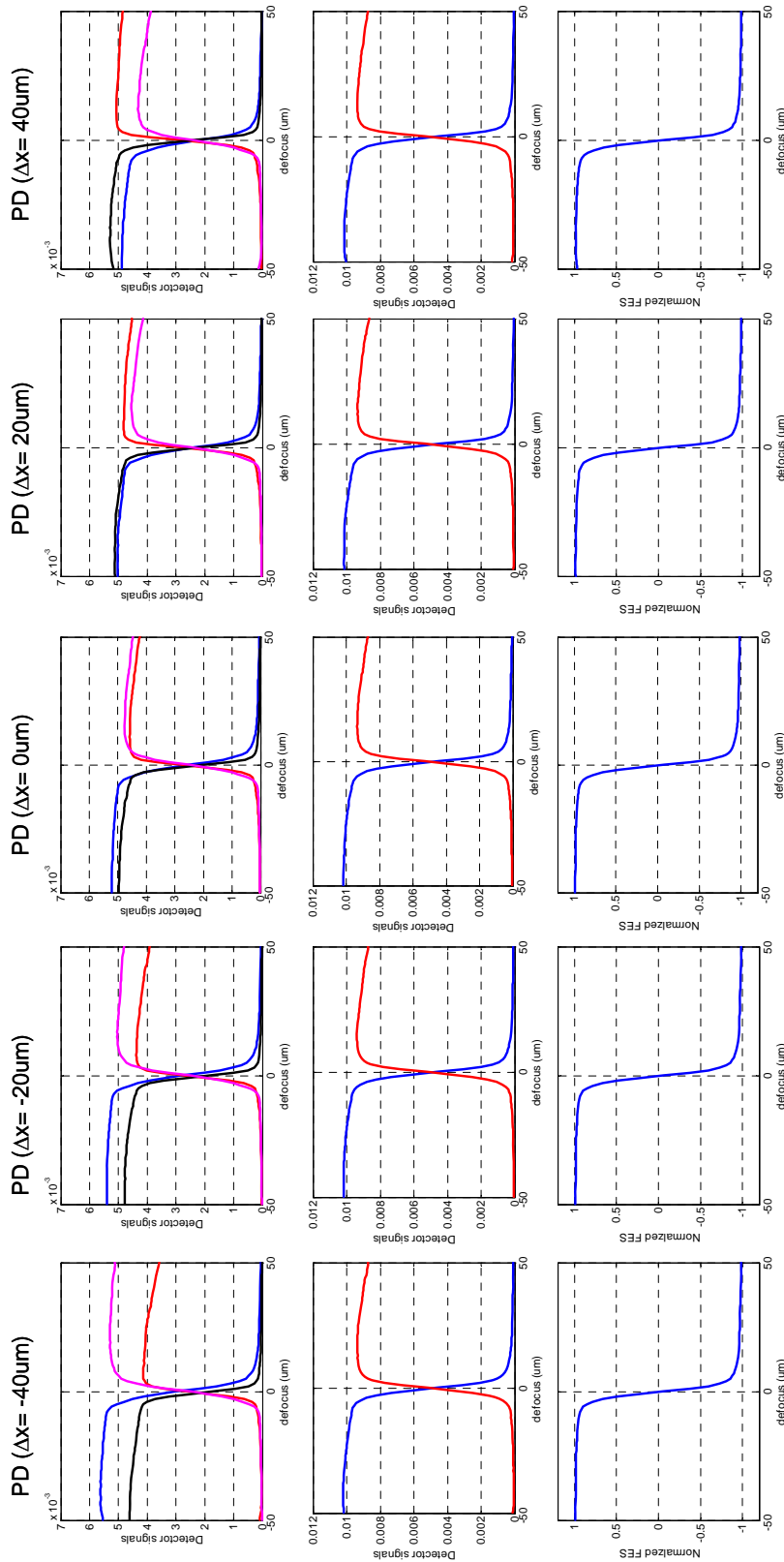


Figure 6.19 Simulated signals when the detector is decentered in the x axis ($|\Delta z| < 50\text{ }\mu\text{m}$). The first row shows four detector signals (A, B, C, D), the second row shows two summed detector signals (A+C, B+D) and the bottom row shows normalized FES signals.

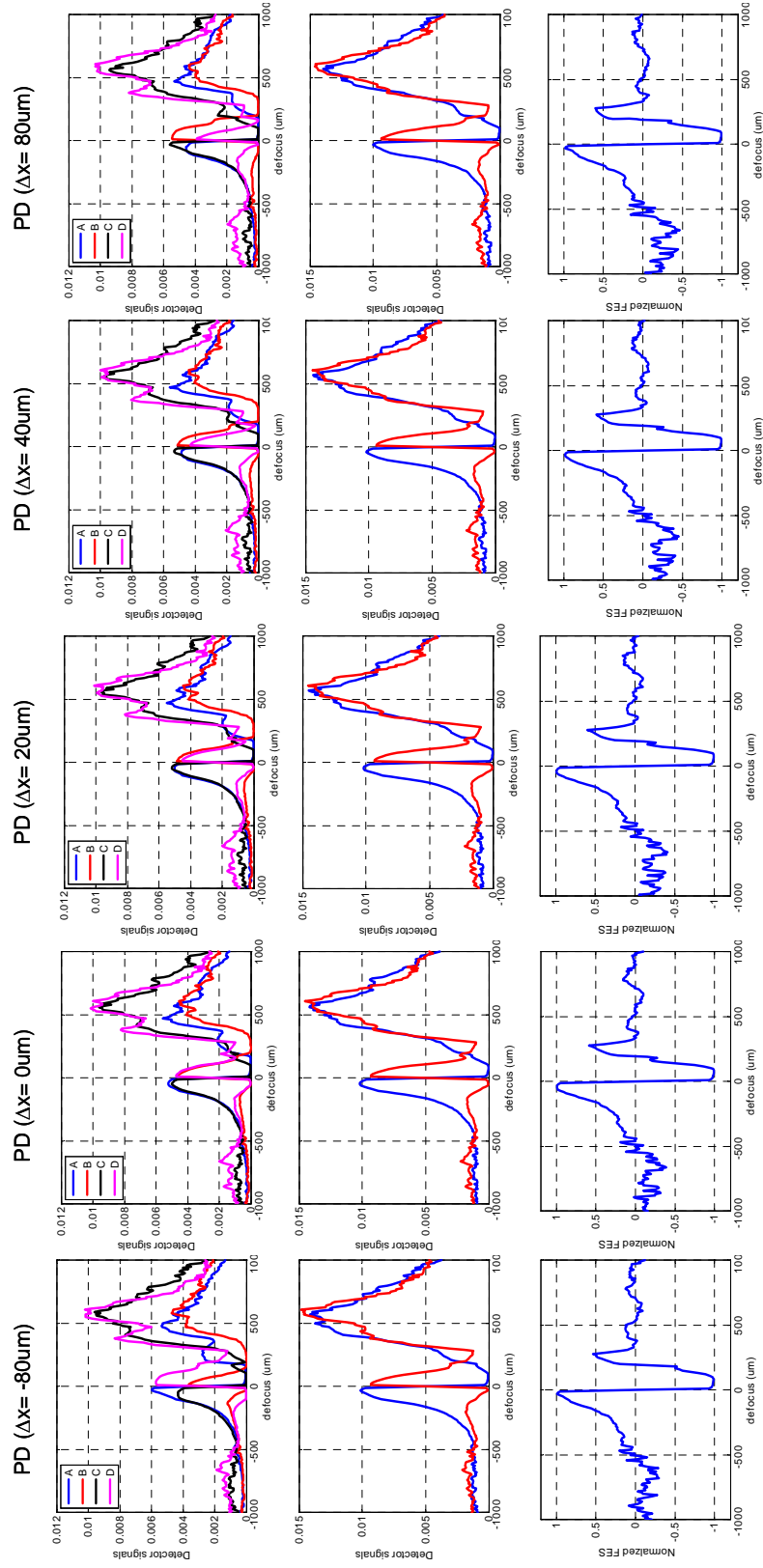


Figure 6.20 Simulated signals when the detector is decentered in the x axis ($|\Delta z| < 1\text{ mm}$). The first row shows four detector signals (A, B, C, D), the second row shows two summed detector signals (A+C, B+D) and the bottom row shows normalized FES signals.

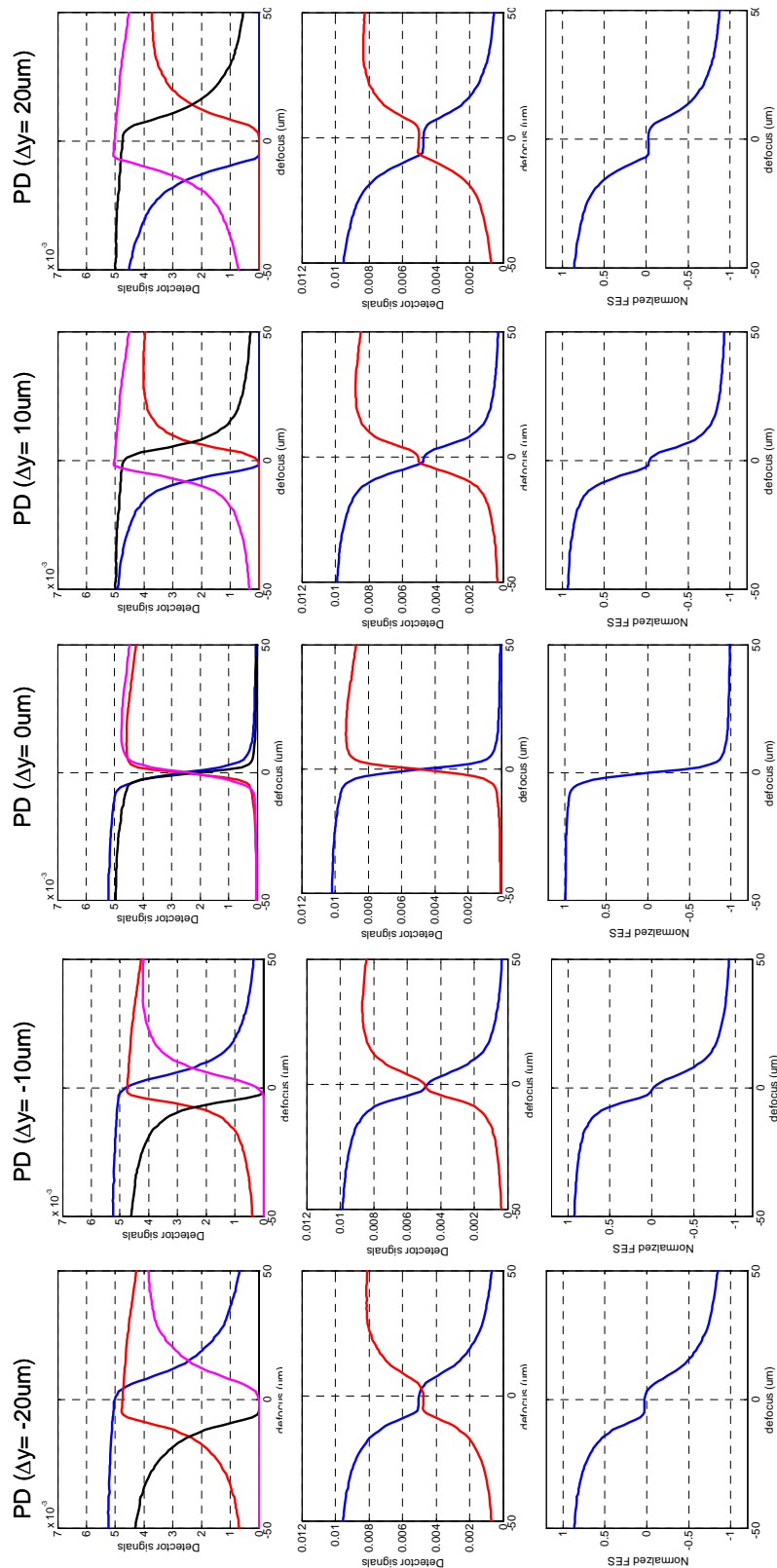


Figure 6.21 Simulated signals when the detector is decentered in the y axis ($|\Delta z| < 50\mu\text{m}$). The first row shows four detector signals (A, B, C, D), the second row shows two summed detector signals (A+C, B+D) and the bottom row shows normalized FES signals.

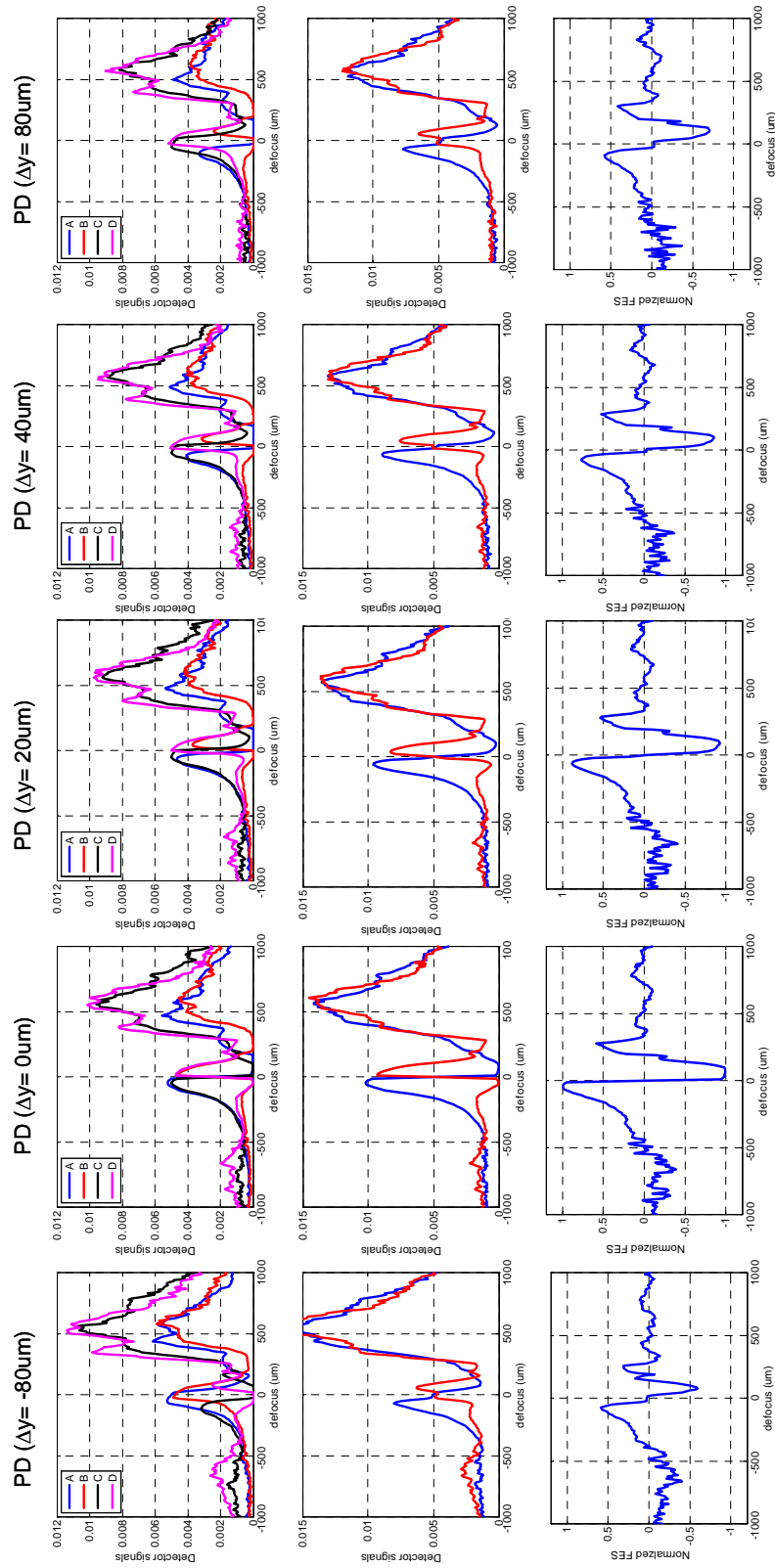


Figure 6.22 Simulated signals when the detector is decentered in the y axis ($|\Delta z| < 1\text{mm}$). The first row shows four detector signals (A, B, C, D), the second row shows two summed detector signals (A+C, B+D) and the bottom row shows normalized FES signals.

in the performance parameters, as shown in Table 6.6. This insensitivity stems from the double knife-edge technique implemented in the DOE focus sensor. The unbalance in the levels of the detector signals, A, D and B, C that is introduced by the x -decenter is compensated during FES calculation. At $\Delta x = 80\mu\text{m}$, the focus offset is less than $0.2\mu\text{m}$, which is acceptable for a system with depth of focus of $1.6\mu\text{m}$.

In contrast, when the detector is displaced in the y axis, individual detector signals shift with respect to best focus, and the normalized FES becomes highly non-linear due to the saddles near the best focus, as observed in Figs. 6.21 and 6.22. The tolerance of y -decenter is about $\pm 10\mu\text{m}$. Table 6.7 summarizes the performance parameters for Δy displacement.

Table 6.4 Performance parameters of the DOE focus servo when the HPLD is rotated about the z axis.

Performance parameters	-2°	-1°	0°	1°	2°
Slope (μm^{-1})	-0.097	-0.151	-0.282	-0.194	-0.104
Linearity within $\pm 2\mu\text{m}$	0.004	0.013	0.023	0.043	0.017
Focus offset (μm)	-9.05	-4.73	0	4.24	8.48

Table 6.5 Performance parameters of the DOE focus servo when the DOE is rotated about the z axis.

Performance parameters	-2°	-1°	0°	1°	2°
Slope (μm^{-1})	-0.06	-0.118	-0.282	-0.097	-0.045
Linearity within $\pm 2\mu\text{m}$	0.008	0.018	0.023	0.017	0.002
Focus offset (μm)	-18.45	-9.53	0	9.53	18.71

Table 6.6 Performance parameters of the DOE focus servo when the detector is decentered in the x axis.

Performance parameters	-40 μm	-20 μm	0 μm	20 μm	40 μm
Slope (μm^{-1})	-0.274	-0.278	-0.282	-0.286	-0.288
Linearity within $\pm 2\mu\text{m}$	0.022	0.022	0.023	0.024	0.024
Focus offset (μm)	0.08	0.05	0	-0.02	-0.03

Table 6.7 Performance parameters of the DOE focus servo when the detector is decentered in the y axis.

Performance parameters	-20 μm	-10 μm	0 μm	10 μm	20 μm
Slope (μm^{-1})	-0.018	-0.027	-0.282	-0.061	-0.041
Linearity within $\pm 2\mu\text{m}$	0.006	0.005	0.023	0.028	0.019
Focus offset (μm)	4.07	-0.66	0	-1.62	-5.89

6.8 FES from the constructed ODD system

Visual observation of diffraction patterns at the detector plane is in good agreement with the simulated beam distribution in Fig. 6.11, although a measured irradiance distribution of diffracted beams, comparable to Fig. 6.11, is not provided due to the large area of diffracted patterns and difficulty of placing a camera at the detector plane after the system is assembled. In the constructed prototype ODD system, the voltages from each cell of the quad-detector are summed and subtracted in the servo electronics to produce an FES. Images of the detector signals and an FES on an oscilloscope are presented in the Fig. 6.23. Figures 6.23(a) and (b) show the two summed detector signals A+C and B+D in the

short defocus range and the long defocus range, respectively. The short defocus range signals in Fig. 6.23(a) are obtained when a typical CD-R disc is mounted. The signals in the long defocus range in Figs. 6.23(b) and (c) are obtained when the objective lens is moved by a few millimeters in the focus search mode of the actuator. The signals experimentally obtained from the constructed prototype ODD system are in good agreement in waveform shapes with the simulated signals shown in Figs. 6.13 and 6.14. The negative going hump to the right of the best focus in Fig. 6.23(c) exhibits the influence of more intense +1st and/or 0th order beams falling on the detector on the FES. In a real ODD system, it only occurs during the focus search mode that produces a large amount of defocus. The measured FES is asymmetric through the best focus, which implies that there are some misalignments in the elements. The rounding of the waveform in the negative FES in Fig. 6.23(c) is similar to the simulated FES in presence of rotational misalignment of the HPLD and the detector. Consequentially, the slope through the best focus decreases and the nonlinearity increases. The measured lock-on range is approximately 125 μm , which is approximately ten times greater than the simulated lock-on range. A probable cause for this discrepancy is that the size of the beam at the detector is larger than that of the simulated beam due to aberrations caused by fabrication errors. Due to the uncertainty of the absolute focus, the focus offset is not estimated from the measured FES signal. However, it is observed that the beam is stably focus-locked on the media during high-power destruction operations for several tens of CD-R, CD-RW and CD-ROM destruction experiments.

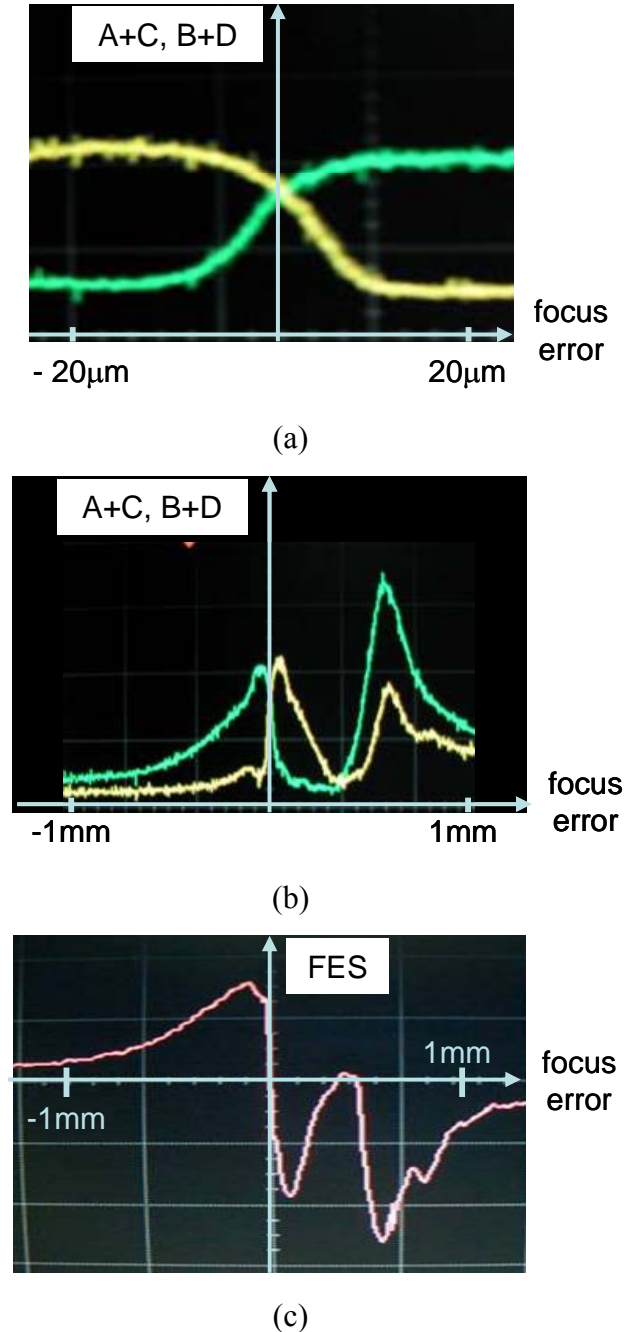


Figure 6.23 Experimental detector signals and FES. Two summed detector signals for a defocus range of (a) $|\Delta z| < 20 \mu\text{m}$ and (b) $|\Delta z| < 1\text{mm}$, and (c) FES for $|\Delta z| < 1\text{mm}$. The humps in (b) and (c) originate from intense $+1^{\text{st}}$ and/or 0^{th} orders penetrating into the quad-cell detector when a large defocus is introduced, and are only observed in a focus search mode of the actuator.

7 CHANGE IN DATA MARKS AND GROOVE STRUCTURES OF CD-R DISCS IN RESPONSE TO A HIGH POWER LASER BEAM

In order to assure complete destruction, it is necessary to understand how data marks are formed in writable discs, such as CD-R, CD-RW and DVD±R, and to evaluate the change in recorded data marks upon exposure to a high-power laser beam ($> 0.5\text{W}$). In this chapter, the mechanisms of data mark formation in writable discs are studied, and the changes in data marks and the groove structures are characterized after discs with different dye materials (cyanine, phthalocyanine, azo) are exposed to a high power laser beam under destruction conditions. The dye/reflector and substrate/dye interfaces of the exposed discs are observed using a high power optical microscope and an atomic force microscope (AFM).

Section 7.2 examines how data marks in writable media are formed. Section 7.3 explains the exposure system used in the experiments. Also, it describes how exposure experiments are performed and samples are prepared for static measurement. Section 7.4 presents the RF signals and histograms from the exposed discs. Section 7.5 provides optical and topological measurement results of unexposed and exposed data marks on optical discs with different types of dyes. In addition, the optical images of the samples obtained by use of optical filters and with illumination of infrared light emitting diodes (LEDs) are provided. Conclusions are presented in Section 7.6.

This chapter is published as a paper in a journal *Optical Engineering* in 2006 with the title of “Change in data marks and groove structures of compact recordable discs in

response to a high power laser beam". The original paper is attached in Appendix III.

7.1 Recording mechanism in writable media

The mechanisms of data mark formation in write-once organic recording media have been extensively studied since the CD-R was developed by Taiyo Yuden in 1989 [Hamada *et al.* 1989, Hamada *et al.* 1992, Holtslag *et al.* 1992, Huh *et al.* 1997]. It is known that several deformation phenomena at the dye/reflector interface and the substrate/dye interface are involved in the formation of a data mark. During the recording process, the energy of a focused laser beam is absorbed by the dye material, increasing the temperature in the dye and substrate layers. As the temperature in the dye layer increases above the dye decomposition temperature ($250\text{--}300^\circ\text{C}$), the dye is melted and decomposed, and gas bubbles or pits are formed at the dye/reflector interface, as illustrated in Figs. 7.1(a) and (b). This type of change is called a dye/reflector feature. Also, as the temperature in the substrate/dye interface is increased above the glass transition temperature ($140\text{--}170^\circ\text{C}$), the polycarbonate (PC) substrate softens and expands toward the dye layer, and the groove walls are deformed, as described in Fig. 7.1(c). This type of change is called a substrate feature. Therefore, a data mark in CD-R discs can contain various amounts of dye/reflector and/or substrate features. The combination of both types of features gives rise to changes in reflectivity when the readout beam scans the data mark.

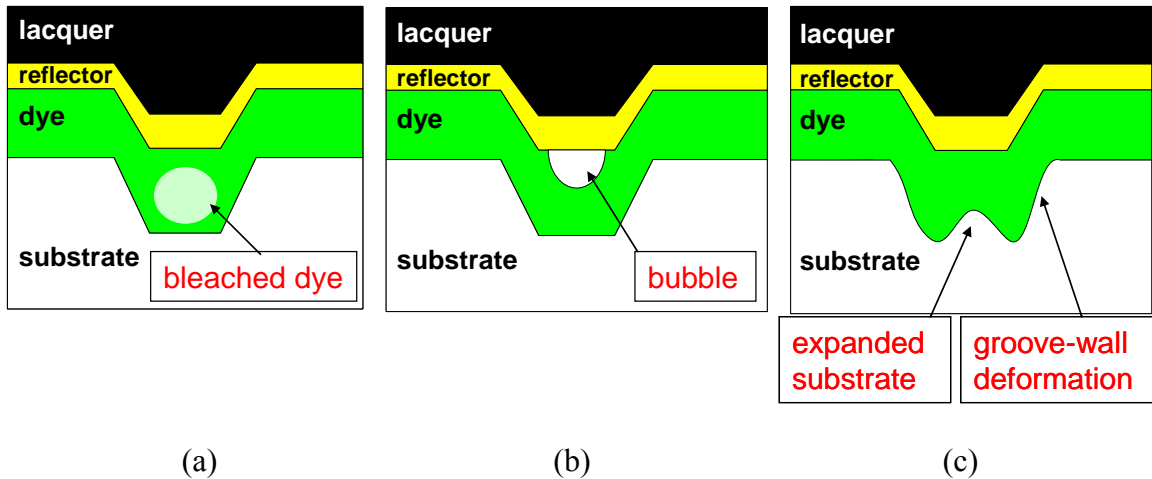


Figure 7.1 Recording mechanism in writable media. (a), (b) dye/reflector feature and (c) substrate feature.

7.2 Exposure experiments

Data marks and groove structures in discs are examined before and after exposure to a high power laser beam. CD-R discs with cyanine, phthalocyanine and azo dyes are used in the experiments. Firstly, data are recorded in the discs using a commercial CD recorder at 48 \times speed. The recorded discs are then put in an exposure system, similar to the ODD system shown in Fig. 6.1. The used exposure system exploits an HPLD ($\lambda = 730\text{nm}$, 0.75W, output aperture $100\mu\text{m} \times 1\mu\text{m}$) and a bi-prism focus sensor. The focused beam on the recording layer is a nearly line beam with dimensions of $50\mu\text{m} \times 2.5\mu\text{m}$. This system also exposes multiple tracks at a time by situating the focused line beam in the radial direction across tracks.

Exposure dose (EX) is the amount of energy applied per unit area on the dye layer. That is,

$$EX = \frac{\text{Energy}}{\text{Scan area}} = \frac{P}{W_r \cdot v_t} , \quad (7.1)$$

where P is the laser power through the lens, W_r is the radial width of the line beam at the disc and v_t is the tangential velocity of a focused beam on a disc. Since W_r is fixed to 40μm in the exposure system, there are two adjustable parameters (P, v_t) that are used to vary the exposure dose. Also, the radial velocity v_r should be slow enough to have some overlap in the exposed areas after one disc revolution, and fast enough to minimize the total disc destruction time. The radial velocity is combined in an overlap factor N_o , which is a measure of the portion of the focused beam that overlaps after one revolution of the disc. N_o is expressed as the ratio of the radial beam length to the distance the beam translates during one revolution. That is,

$$N_o = \frac{W_r}{v_r \cdot T} , \quad (7.2)$$

where T is the temporal period of revolution. The overlap factor should be greater than one ($N_o > 1$) in order to prevent the focused beam from translating longer than W_r and leaving some area unexposed.

Therefore, the exposure dose is adjusted by varying laser power and radial and tangential velocities of the focused beam on a disc. Exposure doses vary, depending on types of dyes in discs, because dyes have different absorptances and reactions to the laser beam. Exposure doses of 4.3nJ/μm² and 2.8nJ/μm² are applied to cyanine- and azo-dye discs, respectively. For phthalocyanine-dye discs, exposure doses of 2.2nJ/μm² and 9.4nJ/μm² are applied.

As a quick measure for data destruction, a readout spin stand is used to retrieve the data signals from the exposed discs. More extensive investigations on the physical change in data marks and CD structures are done in static measurements.

The unexposed and exposed sections on discs are examined in two types of static measurement instruments: a high power optical microscope (objective lens: 150 \times , $NA=0.9$) and an AFM. Also, visible wavelength filters (Kodak WRATTEN color filters) and infrared LEDs ($\lambda_{peak}=780\text{nm}$) are used in the optical microscope observation of phthalocyanine-dye discs. Two types of disc samples are prepared in order to see the features on the substrate as well as the dye. For the dye/substrate sample, the lacquer and reflector layers are removed by using air pressure, and, for the substrate-only sample, the dye is dissolved using isopropanol after the lacquer and reflector layers are blown off. The cyanine, phthalocyanine and azo disc samples are observed under the optical microscope and the AFM from the label side.

7.3 Dynamic Measurement and Results

After exposure, the discs are read at the constant linear velocity of 2.4m/s on a readout test stand. The retrieved time-domain data signals displayed on an oscilloscope (Tektronix DSA602) are observed to assess the levels of destruction. Also, two mega bytes of the data signal are captured using an 8-bit digitizer (NI PCI-5112), and the histograms of data are generated from the digitized signals. Data signals from the exposed sections of cyanine-dye and azo-dye discs at the used exposure doses could not be obtained due to a problem with the tracking servo caused by high-power exposure.

Also, the initial observation is that the amplitude of the RF data signal decreases as the applied exposure dose increases. Therefore, phthalocyanine-dye discs exposed at EX=9.4nJ/ μm^2 are examined in more detail in the following.

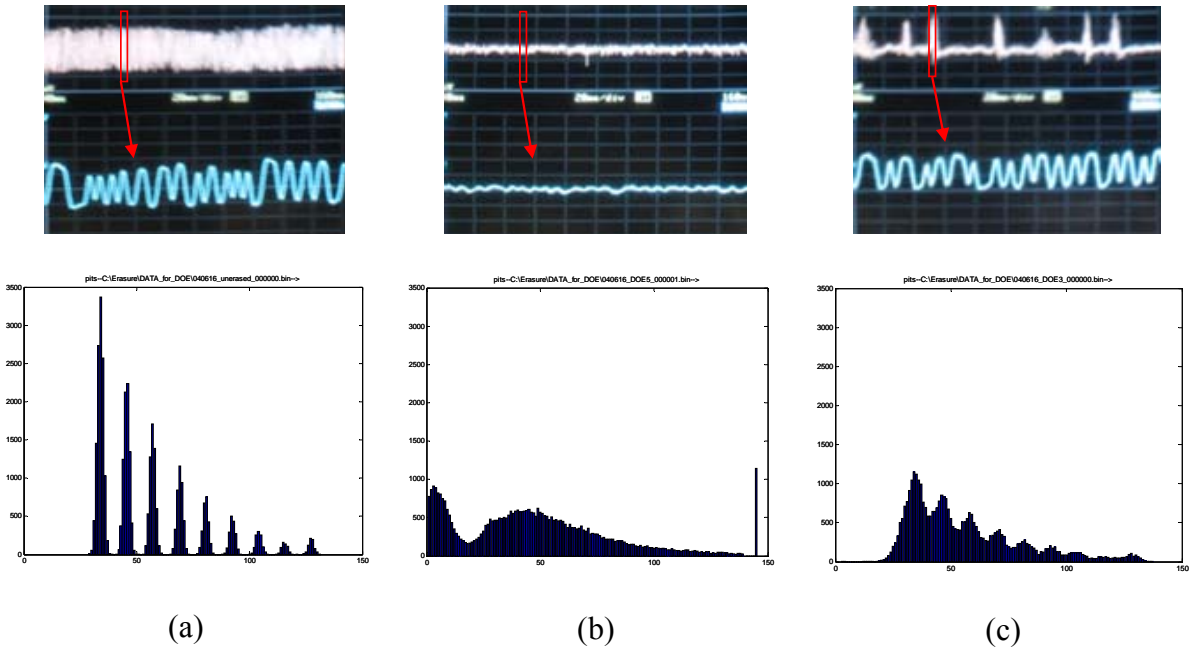


Figure 7.2 RF data signals and histograms from (a) unexposed and (b), (c) exposed sections of phthalocyanine-dye discs (EX= 9.4nJ/ μm^2). Small boxed portions of the upper signals are magnified in the lower signals. In (c), undestroyed data signals are intermittently shown due to the use of an overlap factor smaller than one.

The RF waveform retrieved from an unexposed section of a phthalocyanine-dye disc and its histogram are shown in Figure 7.2(a). Well-separated peaks are observed, which are nine groups for the run-length limited RLL(2, 10) code [Franašek 1972]. Figures 7.2(b) and (c) are the RF signals and the corresponding histograms from the exposed areas. The signal amplitude is decreased more than five times after exposure. In

the histograms in Fig. 7.2(b), there are large zero bin and upper bin populations with no discernable separations between the peaks. Thus, there is no recoverable information using a conventional readout system. In Fig. 7.2(c), however, peaks for a few pit lengths are observable due to the presence of the intermittent undamaged data signal, which results from having an overlap factor less than one. This intermittent full-amplitude data signal can lead to recovery of some data.

7.4 Static Measurements and Results

Firstly, cyanine-dye discs are examined. The optical microscope images of unexposed and exposed data marks are shown in Fig. 7.3. Unexposed data marks in Fig. 7.3(a) are clearly observable before exposure. When exposed to the high-power laser beam ($EX=4.3\text{nJ}/\mu\text{m}^2$), the data marks on both dye/substrate and substrate-only samples are no longer optically observable, as shown in Figs. 7.3(b) and (c). Figures 7.4(a) and (b) illustrate the profiles of a cyanine-dye disc measured using an AFM before and after exposure to the high-power laser beam. The depths of the dye/reflector and substrate features of exposed data marks decrease to less than half the depths of the unexposed data mark features. Also, the pregroove depths decrease from 160nm to 70nm, while the groove depth on the reflector/dye interface is reduced slightly. Furthermore, the angles of the pregroove side walls increase after exposure.

Optical images of the data marks on phthalocyanine-dye discs are shown in Fig. 7.5. The unexposed data marks on the dye/substrate sample look dark, compared to the land, as shown in Fig. 7.5(a). After an exposure dose of $2.2\text{nJ}/\mu\text{m}^2$ is applied to the disc,

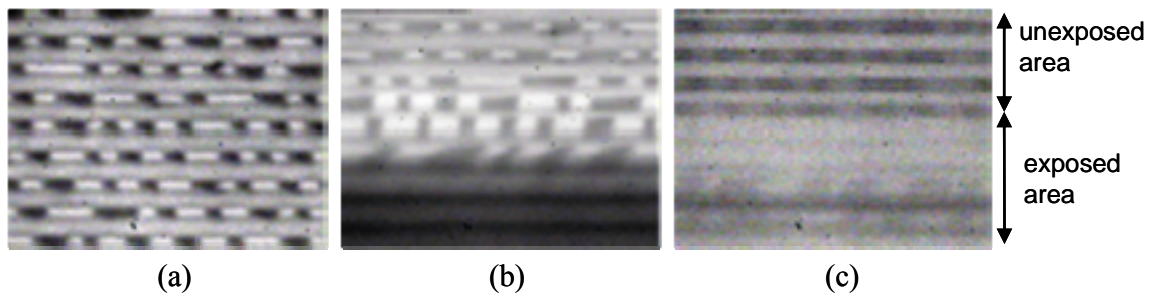


Figure 7.3 Optical microscope images of unexposed and exposed data marks on cyanine discs. (a) Unexposed data marks on dye/substrate sample, (b) exposed data marks on dye/substrate sample ($EX= 4.3\text{nJ}/\mu\text{m}^2$) and (c) exposed data marks on substrate-only sample ($EX= 4.3\text{nJ}/\mu\text{m}^2$). In (b) and (c), the upper portion of the observation area is unexposed.

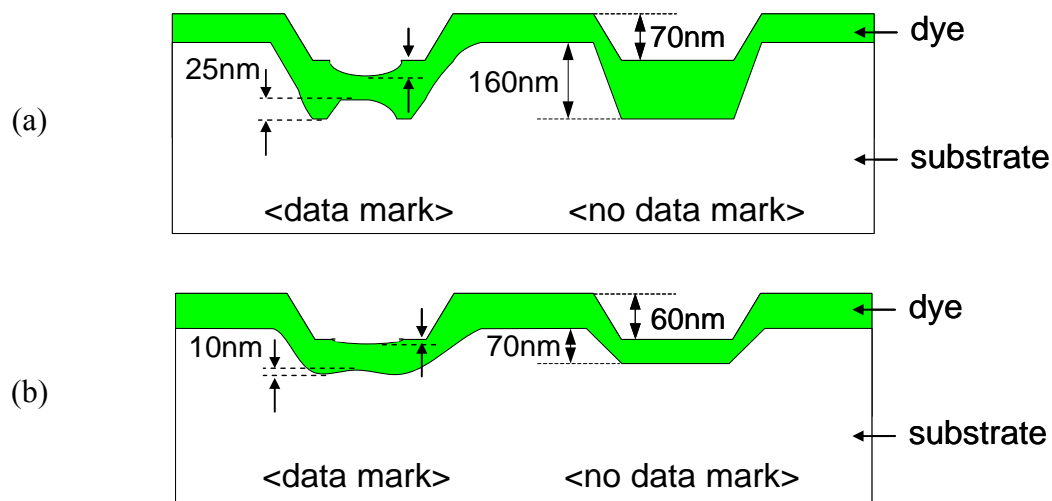


Figure 7.4 Profiles of a cyanine-dye disc measured using an AFM (a) before and (b) after exposure to a high-power laser beam ($EX= 4.3\text{nJ}/\mu\text{m}^2$).

the data marks turn brighter than the land area, as shown in Figs. 7.5(b). In this case, the contrast of the data marks on the dye/substrate sample reverses after exposure. One hypothesis for the contrast reversal is that phthalocyanine dye at the recorded data marks is not fully inert and responds to additional optical energy, resulting in higher visual-wavelength reflectance of the dye.

In order to verify this hypothesis, a static exposure experiment is performed. While being observed under a high-power optical microscope, recorded data marks are exposed to a tightly focused red laser beam through a microscope objective. The marks turn bright immediately, which supports the hypothesis of phthalocyanine dye still being active after recording. Also, data marks on the substrate-only sample are bright compared to the land area and become much brighter than the land after high-power exposure ($EX=2.2\text{nJ}/\mu\text{m}^2$), as shown in Fig. 7.5(c). The high reflectances of as-written and high-power exposed data marks originate from mixing of the dye and the substrate material. This reasoning is confirmed in an experiment where the substrate-only samples are exposed to a high-power laser beam. If no dye remains in the as-written data-mark areas, no reaction should occur during high-power exposure. Instead, sparking is observed in these areas. The sparking is characteristic of phthalocyanine dye in air under high-power exposure. The dye and substrate mixture is explained by the temperature at the dye/substrate interface that increases instantly above the decomposition temperature of the dye and the melting temperature of the PC during the processes of recording and high-power exposure. The decomposed dye and melted substrate material mix at the recorded marks and high-power exposed areas.

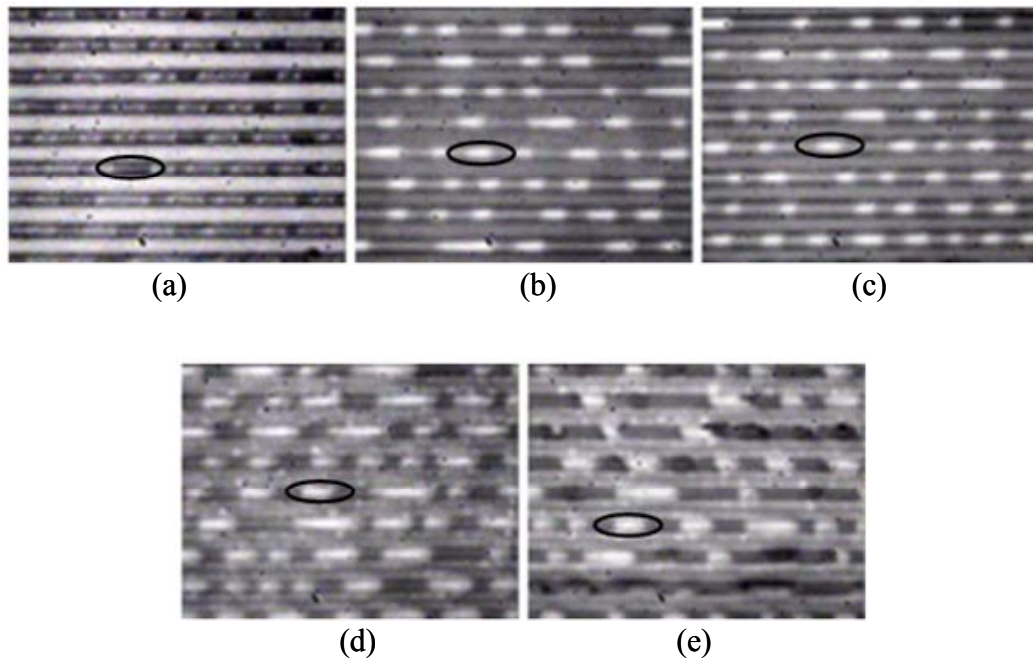


Figure 7.5 Optical microscope images of unexposed and exposed data marks on phthalocyanine discs. (a) Unexposed data marks on dye/substrate sample, (b) exposed data marks on dye/substrate sample ($EX= 2.2\text{nJ}/\mu\text{m}^2$), (c) exposed data marks on substrate-only sample ($EX= 2.2\text{nJ}/\mu\text{m}^2$), (d) exposed data marks on dye/substrate sample ($EX= 9.4\text{nJ}/\mu\text{m}^2$) and (e) exposed data marks on substrate-only sample ($EX= 9.4\text{nJ}/\mu\text{m}^2$). In each figure, a representative data mark is circled.

With an increased dose of $9.4\text{nJ}/\mu\text{m}^2$, the dye in no-data-mark areas of both dye/substrate and substrate-only samples turn as bright as the exposed data marks, as shown in Figs. 7.5(d) and (e). Despite the scattered bright dots, the data marks are still optically discernible. The results of the AFM measurements are shown in Figs. 7.6(a) and (b). The dye/reflector and substrate features of the data marks are significantly reduced in size. After exposure, as shown in Fig. 7.6(b), the protruded substrate on the data marks almost flattens, and the pregroove depth is decreased to half the depth before exposure.

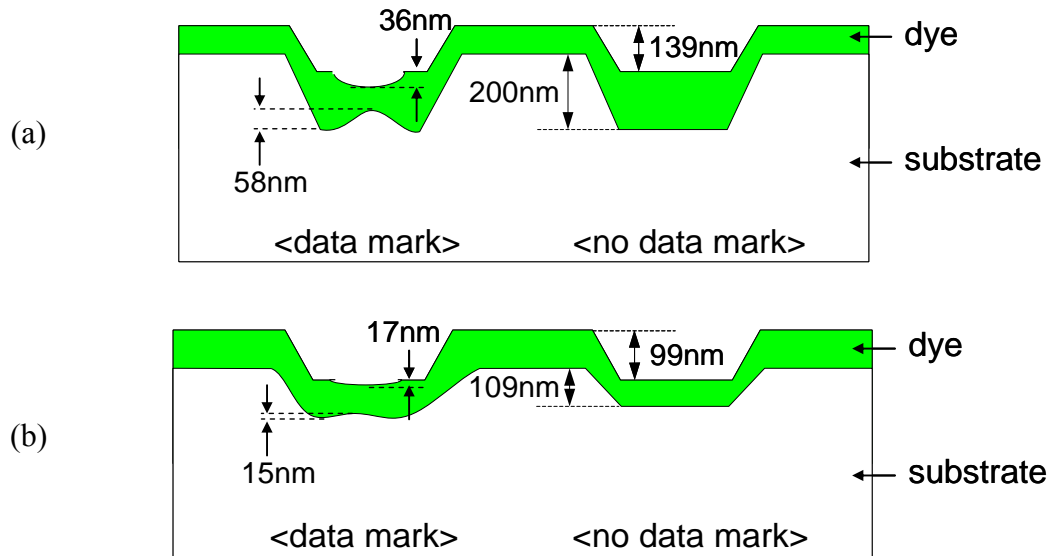


Figure 7.6 Profiles of a phthalocyanine-dye disc measured using an AFM
(a) before and (b) after exposure ($EX = 9.4\text{nJ}/\mu\text{m}^2$).

Therefore, once exposed at $9.4\text{nJ}/\mu\text{m}^2$, data marks on phthalocyanine-dye discs are still visible optically, but barely noticeable topologically.

Curiously, when the data marks of exposed phthalocyanine-dye discs are observed by use of 780nm LEDs as the illumination source, exposed data marks are not visible, contrary to observable as-written data marks. Therefore, it is difficult to retrieve any data from the exposed phthalocyanine disc using a conventional CD readout system using a 780nm laser diode. On the other hand, the exposed data marks are visible when illuminated by a white light with green and blue color filters. Accordingly, a CD readout system modified with a green- or blue-wavelength laser and an aberration-corrected objective lens might be able to recover data from the exposed disc, if the distortions caused by the exposure are not too severe.

Finally, the optical microscope images of unexposed and exposed data marks on azo-dye discs are shown in Fig. 7.7. The unexposed data marks on the dye/substrate sample are clearly observable as shown in Fig. 7.7(a), but contrast of the unexposed data marks on the substrate-only sample is low, as shown in the unexposed area of Fig. 7.7(c). When the azo-dye discs are exposed at $2.8\text{nJ}/\mu\text{m}^2$, data marks become optically indiscernible, as seen in Figs. 7.7(b) and (c). However, small bubbles are formed as by-products of fast dye decomposition. The profiles of an azo-dye disc measured using an AFM are presented in Fig. 7.8. Unexposed data marks on azo-discs have the smallest dye/reflector and substrate features among the three types. Upon exposure, data mark features and the groove modulation are slightly decreased. The surfaces of both dye/reflector and substrate/dye interfaces are rough, due to the bubbles.

Results discussed in the preceding paragraphs were repeatable over discs fabricated by several manufacturers. Although slight ($\pm 10\%$) differences are observed in

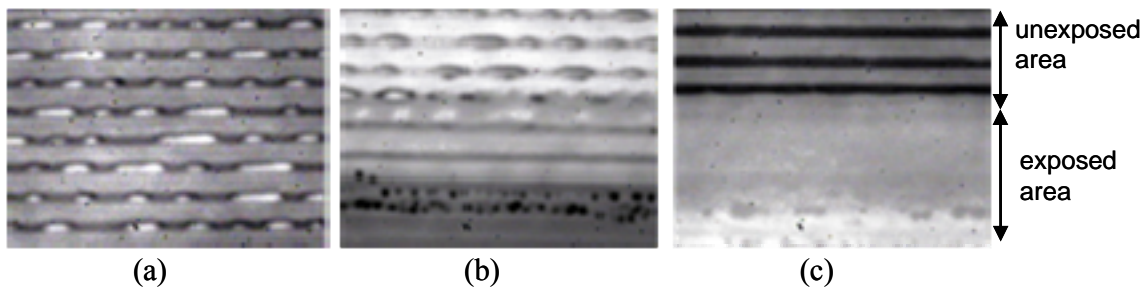


Figure 7.7 Optical microscope images of unexposed and exposed data marks on azo discs. (a) Unexposed data marks on dye/substrate sample, (b) exposed data marks on dye/substrate sample ($\text{EX}= 2.8\text{nJ}/\mu\text{m}^2$) and (c) exposed data marks on substrate-only sample ($\text{EX}= 2.8\text{nJ}/\mu\text{m}^2$). In (b) and (c), a small upper portion of the observation area is unexposed.

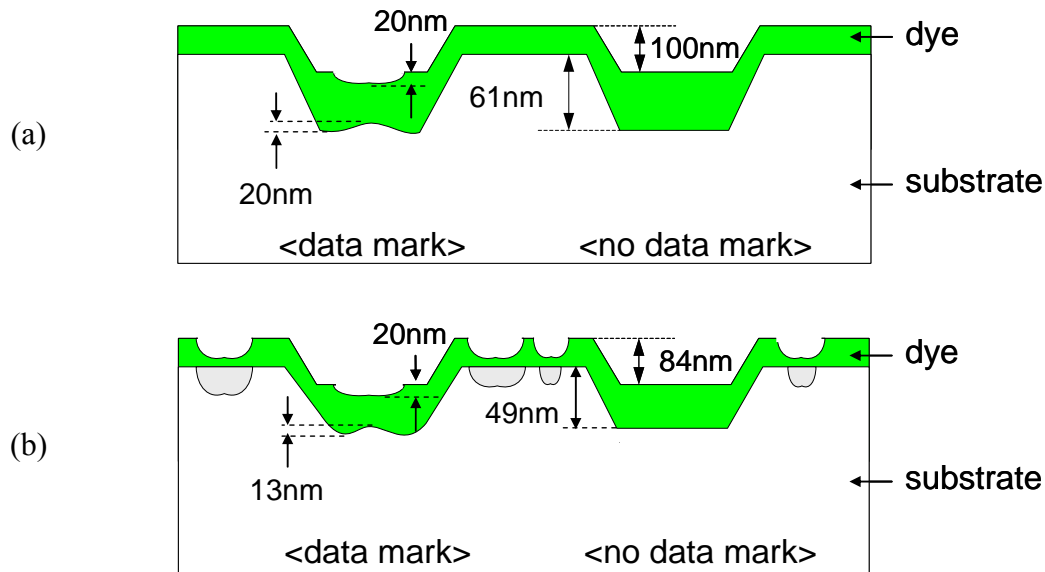


Figure 7.7 Profiles of an azo-dye disc measured using an AFM (a) before and (b) after exposure to a laser beam (EX= 2.8nJ/ μm^2).

the power levels required to produce the effects, the physical observations were essentially the same.

7.5 Chapter conclusions

Recorded CD-R discs are exposed to a high-power laser beam for the purpose of data destruction, and the changes in data marks and groove structure are observed using an optical microscope and an AFM. For the cyanine-dye discs exposed at 4.3nJ/ μm^2 , data marks are optically invisible and the depth modulations of data marks and the grooves are decreased when observed using the AFM. Surprisingly, for phthalocyanine discs, visible-light contrast of data marks are enhanced upon exposure, and the data marks are visible with an optical microscope at the exposure dose of 2.2nJ/ μm^2 . Small bright dots are

created on both dye and the substrate at the exposure dose of $9.4\text{nJ}/\mu\text{m}^2$, but the data marks are recognizable. The contrast reversal on the dye/substrate samples could be because phthalocyanine dye at the recorded data marks is not completely inert and reacts to a high power laser beam. Also, the contrast enhancement on the substrate-only samples is due to mixing of the dye and the substrate material. Optical observations of the exposed data marks by use of infrared LEDs and a white light with green and blue filters show that data can not be retrieved in a conventional CD reader. The azo discs exposed at $2.8\text{nJ}/\mu\text{m}^2$ show bubbles in both the dye layer and the substrate. Data marks are optically indistinguishable and pregroove modulation is decreased.

In summary, data destruction using a high-power laser beam is possible, but successful destruction depends greatly on exposure conditions and the type of dye used in the disc recording layer. This investigation has revealed interesting characteristics of recording using different dye materials, especially with phthalocyanine.

8 FURTHER DESTRUCTION TESTS USING ODD SYSTEM

8.1 Introduction

The prototype ODD system shown in Fig. 6.6 is used to destroy data on optical media including CD-ROM, CD-R, and CD-RW. For CD-R and CD-RW, data are recorded using a commercial CD recorder at the speed of 48 \times and 24 \times , respectively. The changes in data marks and surrounding structures are inspected using high power optical microscopes (standard 100 \times magnification and spherical-aberration correcting 100 \times magnification) before and after destruction tests.

For each destruction test, the exposure dose is adjusted by varying laser power and radial and tangential velocities of the focused beam on a disc. Exposure doses vary, depending on the CD format, because different formats have different compositions of layers. For example, a CD-ROM has no light-absorbing material between a PC substrate and a reflector layer, while a CD-R and a CD-RW has a dye layer and a metal alloy layer surrounded by dielectric thin films, respectively, that absorb some of the incident light energy. Furthermore, dye materials used in a CD-R have different absorptances and reactions to the laser beam, which must be taken into consideration when exposure doses required for complete data destruction of various CD formats need to be determined [Choi and Milster 2006].

After destruction tests, three types of disc samples that contain both unexposed and exposed areas are prepared: through-substrate sample, substrate-only sample, and

reflector sample. The through-substrate samples have the original format of a disc, and data marks are observed through the 1.2 mm thick substrate using a spherical-aberration correcting microscope objective. For the substrate-only sample, data marks are observed from the label side using a standard optical microscope after the reflective and protective layers are removed. In case of CD-R, dye is dissolved using isopropanol. The reflector samples are the removed reflective and protective layers, and data marks on the reflector are observed using a standard optical microscope.

8.2 Destruction test of CD-ROM discs

The optical microscope images of unexposed and exposed data marks are shown in Fig. 8.1. Unexposed data marks are clearly observable on the unexposed areas from all the three types of samples. When exposed to the high-power laser beam ($EX = 50\text{nJ}/\mu\text{m}^2$), the reflector material, aluminum, of CD-ROM discs interacts with oxygen infiltrated through the lacquer and label layers with help of heat and becomes aluminum oxide. It is shown by darker data marks at the unexposed and exposed boundary than in the unexposed area in Fig. 8.1(a) that aluminum oxidation occurs first on data marks and then spreads into adjacent data marks. Data marks on the exposed area of through-substrate and substrate-only samples are indistinguishable. However, exposed but undestroyed data marks are observable on the protective layer. In fact, the reflector sample has no reflector but the protective layer, since oxidized aluminum remains on the substrate when the reflective and protective layers are peeled off. To ensure complete data destruction, a CD-ROM disc is exposed at $EX = 200\text{nJ}/\mu\text{m}^2$. In the exposed area, no data marks are observable on

all three types of samples due to oxidized aluminum and the melted lacquer and label.

The total time for complete data destruction of a CD-ROM at $EX= 200\text{nJ}/\mu\text{m}^2$ is 10 minutes.

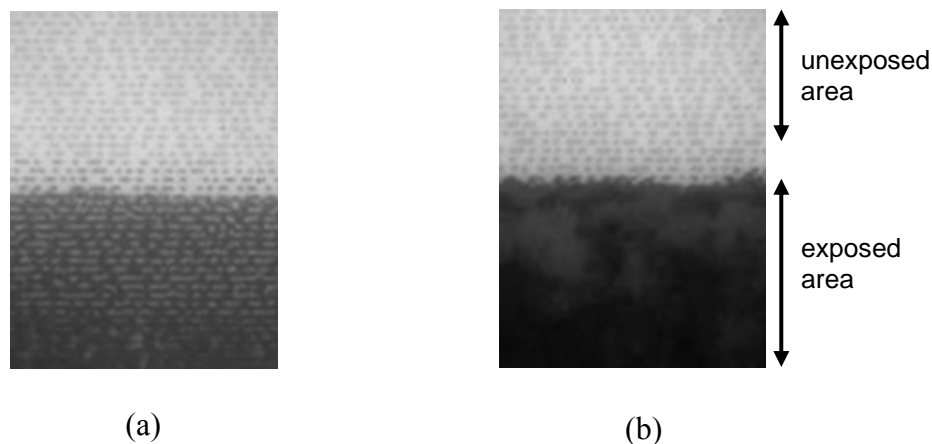


Figure 8.1 Optical microscope images of unexposed and exposed data marks on CD-ROM disks. (a) Unexposed and exposed data marks on through-substrate sample ($EX= 50\text{nJ}/\mu\text{m}^2$), and (b) unexposed and exposed data marks on through-substrate sample ($EX= 200\text{nJ}/\mu\text{m}^2$). In each image, an upper portion of the observation area is unexposed. On the exposed areas, aluminum in the reflective layers oxidizes, making data marks indiscernible.

8.3 Destruction test of CD-R discs

CD-R discs with different organic dyes are tested. Phthalocyanine, cyanine and metalized azo are the common dye materials used in CD-R discs and, therefore, commercially-available CD-R discs with these dyes are chosen for data destruction tests. It is demonstrated in Chapter 7 that phthalocyanine-dye discs are the most resistant to laser data destruction and that data marks of phthalocyanine-dye discs remain optically

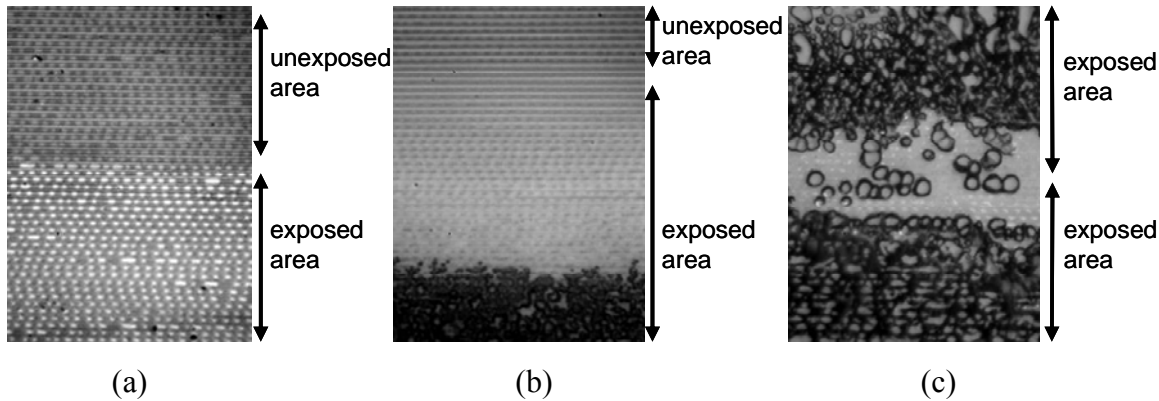


Figure 8.2 Optical microscope images of the unexposed and exposed data marks on phthalocyanine-dye CD-R disks. (a) Unexposed and exposed data marks on substrate-only sample ($EX= 15\text{nJ}/\mu\text{m}^2$). (b) Unexposed and exposed data marks on through-substrate sample ($EX= 35.5\text{nJ}/\mu\text{m}^2$). Bubbles are formed in some of the exposed area. (c) Unexposed and exposed data marks on substrate sample ($EX= 35.5\text{nJ}/\mu\text{m}^2$). The boundary between two exposed areas when exposed at the overlap factor N_o of 1. The radial width of the bubbled area is $130\mu\text{m}$. In (a) and (b), the upper portion of the images is unexposed.

discernible even after exposed to a high power laser beam ($EX= 9.4\text{nJ}/\mu\text{m}^2$ at $\lambda= 730\text{nm}$) and that the exposed discs might be retrieved using a CD readout system modified with a green- or blue-wavelength laser and an aberration-corrected objective lens. When exposed at less than $15\text{nJ}/\mu\text{m}^2$ in the ODD system, data marks on phthalocyanine-dye CD-R discs are optically visible, as shown in Fig. 8.2(a). This result is consistent with the observation in Section 7.4, except the different levels of exposure dose associated with different dye absorption at 730nm and 808nm . At an increased exposure dose ($EX= 35.5\text{nJ}/\mu\text{m}^2$), however, micro-bubbles are formed as shown in Fig. 8.2(b). These bubbles are produced from the melting of PC due to increased temperature at the dye/substrate interface. Data marks are distorted with the bubbles and are indiscernible on all the three

types of samples. However, the bubbles are only in the central portion of the exposed area, and contrast-reversed data marks are still observed at the unexposed and exposed boundary. Figure 8.2(c) shows the boundary between two exposed areas (EX= $35.5\text{nJ}/\mu\text{m}^2$ with $N_o = 1$). The radial width of the exposed bubbled area is $130\mu\text{m}$, leaving a $30\mu\text{m}$ band of the exposed area with little bubbles at the boundary. When the radial velocity is adjusted for $N_o = 1.16$, data on a phthalocyanine CD-R disc is completely destroyed within two minutes.

Micro-bubbles are also observed on cyanine-dye CD-R discs exposed at EX= $30\text{nJ}/\mu\text{m}^2$, as shown in Fig. 8.3(a). The bubbles are created at the dye/substrate interface, making data marks on through-substrate, substrate-only, reflector samples completely unrecognizable. CD-R discs with metalized azo dye exhibit bubbles when exposed to a lower dose (EX= $23.7\text{nJ}/\mu\text{m}^2$), as shown in Fig. 8.3(b). Data marks at the dye and substrate layers are covered with bubbles, and data marks on the reflector are also invisible. Note that the exposed area is brighter than the unexposed area because the azo dye decomposes upon exposure and changes the color from dark blue to nearly white.

8.4 Destruction test of CD-RW discs

A CD-RW disc is different from a CD-R disc in the data mark formation mechanism and the recording layer structure. A CD-RW disc has a recording medium consisting of a phase-change metal alloy layer and dielectric layers that insulate heat produced within the metal layer [Iwasaki *et al.* 1992]. A pulsed writing laser beam heats the crystalline metal

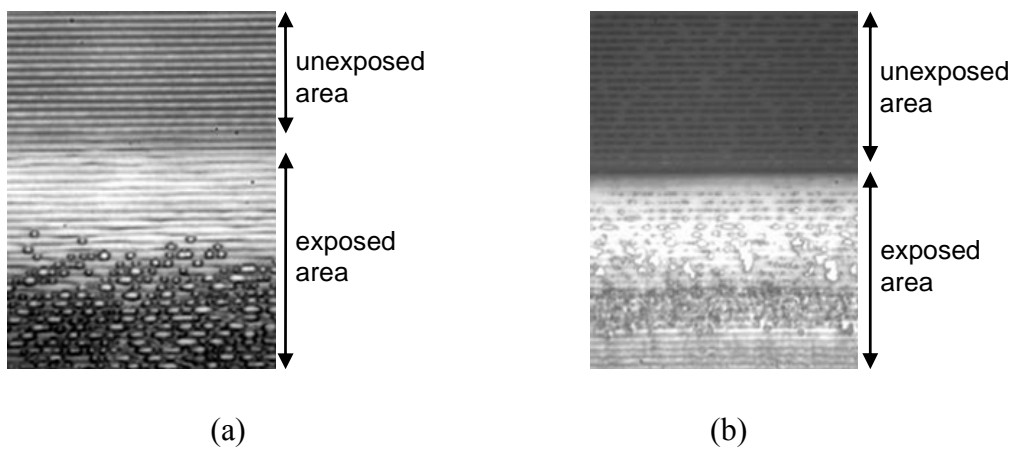


Figure 8.3 Optical microscope images of unexposed and exposed data marks on (a) through-substrate sample of a cyanine-dye CD-R disk ($EX= 30\text{nJ}/\mu\text{m}^2$) and (b) through-substrate sample of an azo-dye CD-R disk ($EX= 23.7\text{nJ}/\mu\text{m}^2$). In each figure, an upper portion of the observation area is unexposed.

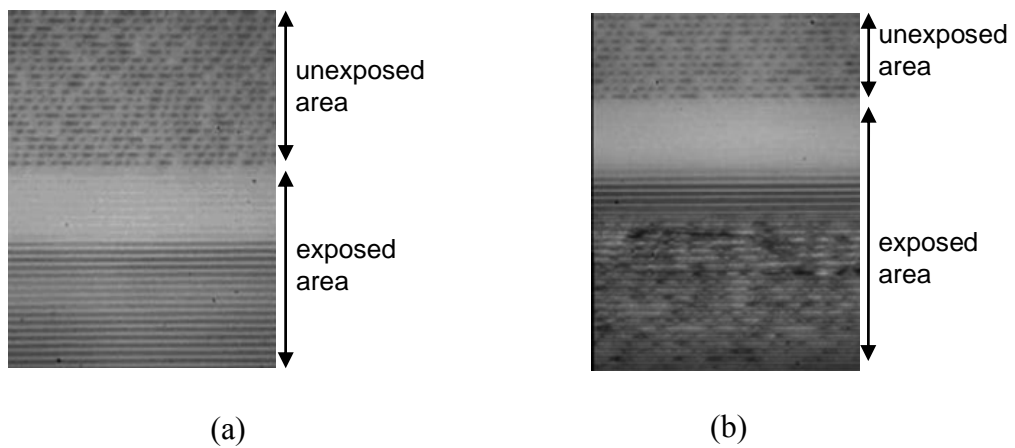


Figure 8.4 Optical microscope images of unexposed and exposed data marks on CD-RW disks.(a) Unexposed and exposed data marks on through-substrate sample ($EX= 17.5\text{nJ}/\mu\text{m}^2$), and (b) unexposed and exposed data marks on through-substrate sample ($EX= 30\text{nJ}/\mu\text{m}^2$).

alloy and changes its state into an amorphous state. During the erasure process, a constant and intermediate-power laser beam heats the metal alloy above 500°C and, a rapid quenching returns the material state of data marks to a blank crystalline state. When CD-RW discs are exposed to a high-power laser beam ($EX = 17.5\text{nJ}/\mu\text{m}^2$) in the ODD system, data marks are erased, as shown in Fig. 8.4(a). When exposed at $EX = 30\text{nJ}/\mu\text{m}^2$, however, the metal alloy as well as surrounding dielectric layers are melt, and data marks are totally destroyed, as shown in Fig. 8.4(b).

8.5 Summary of the destruction test results

The results of the tests are summarized in Table 8.1. Levels of exposure dose required to produce the same results were slightly different ($\pm 10\%$) for discs fabricated by several manufacturers, but the physical observations were essentially the same.

Table 8.1. Summary of destruction tests on CD-R and CD-RW discs

	CD-R			CD-RW
	Phthalocyanine	Cyanine	Azo	
Exposure dose ($\text{nJ}/\mu\text{m}^2$)	35.5	30	23.7	30
Total disc destruction time (min)	2	1.5	1	1.5

9 CONCLUSIONS AND FUTURE WORK

9.1 Conclusions

Secure disposal of optical discs has become important, as optical media are widely used to store personal or sensitive data. This dissertation studies optical techniques for securely destroying data stored in optical discs so that any bit of data can not be restored, even from a disc fragment. Along the way, a novel focus system is developed and tested. Also, unique imaging properties of high power laser diodes (HPLDs) are investigated, as well as ways to simulate optical systems using these light sources.

Several optical destruction techniques and related systems are investigated, and a few preliminary experiments completed for a feasibility study. Basic components of optical data destruction systems are described, and an engineering tool using a HPLD and a novel DOE focus sensor are designed and developed. The optical data destruction (ODD) system is used in many experiments with various exposure conditions to investigate the physical and topological change in data marks and to see the proof of complete and secure destruction.

After a brief overview of optical data storage technology, Gaussian beam optics, and several optical system modeling methods, optical characteristics of an HPLD beam and its propagation behavior in an optical system are explored. It is shown that the HPLD beam contains many higher-order lateral modes. Hence, the output beam in the lateral direction is many times diffraction-limited. Also, it is discovered that the spectrally-resolved lateral modes of the HPLD beam have irradiance profiles similar to Hermite-

Gaussian modes, but their lateral widths are limited by the width of the current-injecting stripe. The coherence experiment indicates that the mutual intensity decreases sharply as the separation of two points increases and as injected current increases. In addition, a geometrical optics model utilizing limited-divergence raytracing (LDRT) is introduced, and the propagation behavior predicted by this model in a simple two-lens system is compared with that of the real HPLD beam as well as Gaussian beam propagation property. The LDRT model shows a good agreement with the real HPLD beam and, therefore, it is used to model the ODD system and to simulate the focus error signal (FES).

A prototype ODD system is designed and constructed. The system uses a focused high power line beam that scans over data marks on optical media. Upon exposure, the physical and optical properties of the data marks and surrounding layers are changed due to heat generated by absorption of the incident light energy, making the data irretrievable by no means. The ODD system uses a novel DOE focus sensor to compensate focus errors due to warping in discs or disc tilt when mounted in a drive. The DOE has two amplitude gratings slanted at an angle that produce a crossed diffraction pattern. Only the +3rd order diffraction beams from the two gratings are used for focus sensing to avoid damage or performance deterioration of a photodiode caused by the intense incident light. Also, the efficiencies of the even diffraction orders are minimized by designing the duty cycle of the gratings to be 50%. This focus sensor is compatible with both a point light source and an extended line source. A stable focus lock of the line beam on the data layer of optical media has been maintained as a disc rotates in many destruction tests.

In Chapter 7, changes in data marks and groove structures are examined when a high power laser beam is focused on CD-R data layers. Observations are recorded as a function of exposure condition and the type of dye used in the recording layer. All samples experience a decrease in the depths of data mark features and the pregroove modulations upon exposure. Data marks on cyanine- and azo-dye discs become optically invisible after exposure, while data marks on phthalocyanine-dye discs remain visible even after high-power exposure. Also, phthalocyanine-dye discs show interesting phenomena, including mixture of the dye and the substrate material during recording and contrast reversal of the marks.

Further data destruction tests are performed on various formats of CD-ROM, CD-R, and CD-RW. When a CD-ROM disc is exposed to $50\text{nJ}/\mu\text{m}^2$, aluminum in the reflective layer is oxidized and blackens the exposed area. However, clear data marks are observed on the protective layer. A higher exposure ($200\text{nJ}/\mu\text{m}^2$) further oxidizes the aluminum and melts lacquer and label, destroying all data. CD-R discs with phthalocyanine, cyanine, metalized azo dyes exhibit bubbles upon exposure at $35.5\text{nJ}/\mu\text{m}^2$, $30\text{nJ}/\mu\text{m}^2$, and $23.7\text{nJ}/\mu\text{m}^2$, respectively. Bubbles and decomposed dyes are mixed so that no data marks are observed on the through-substrate, substrate-only, and reflector samples. When a CD-RW disc is exposed at $\text{EX}= 30\text{nJ}/\mu\text{m}^2$, the metal alloy as well as surrounding dielectric layers are melt, and data marks are obliterated.

In summary, an optical data destruction system using a HPLD is developed and tested, and the physical and topological change in data marks upon optical destruction is clearly explained from many destruction experiments with varying applied exposure dose.

Exposure conditions required for complete data destruction depend greatly on the format of optical media. This investigation has demonstrated that the complete destruction of data on CD-ROM, CD-R and CD-RW discs is possible. The new focus servo provides good performance in this application, and it is determined that the LDRT method is adequate for designing optical systems using this light source.

9.2 Future work

It is a natural step to extend the ODD system to destroy DVD, HD-DVD and BD discs, because the prototype ODD system is designed to destroy CD format discs only. This limitation originates from the fact that the objective lens in the current ODD system is designed to compensate the aberration through the CD substrate of 1.2mm, while the substrate thicknesses of DVD (0.6mm), HD-DVD (0.6mm) or BD (0.1mm) are smaller. Therefore, when discs in other formats are placed in the ODD system for destruction, the aberration through the wrong thickness substrate becomes detrimental and the beam widths at the data layer become larger, thus reducing the intended exposure dose. Therefore, some modification to the system should be made in order to extend its use to destroying the newer generation. One simple way is to add another substrate between the objective lens and the disc so that the total thickness of the substrates becomes 1.2mm. Since the objective lens has a working distance of 2.5mm, there is enough space for the auxiliary substrate. Disadvantages of this approach might be the reduction in the range of the actuator movement, possible resonance of the actuator due to the added weight or multiple reflections from the substrate surfaces. Also, the substrate should be optics-

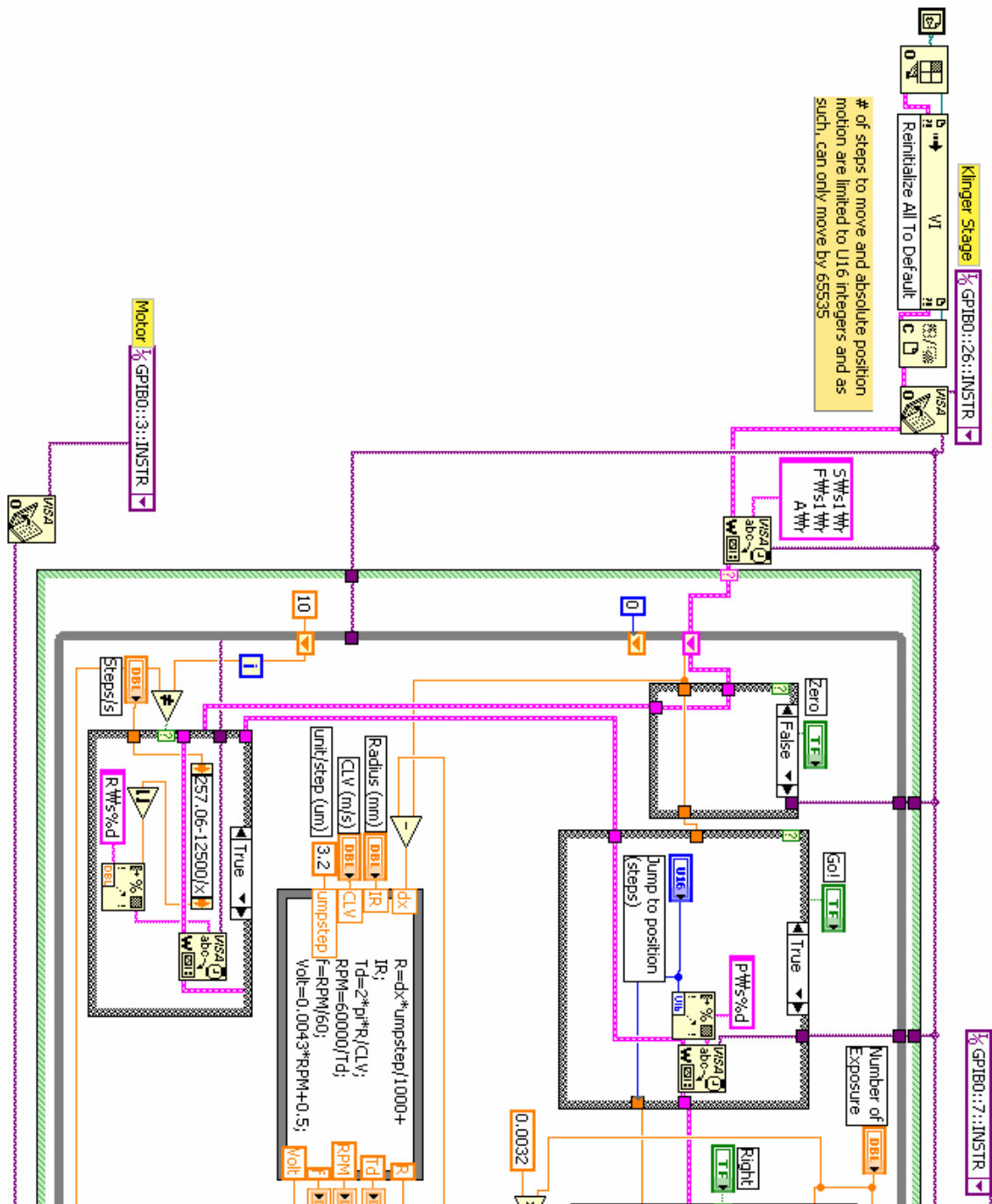
quality to minimize the aberration that might be introduced by it.

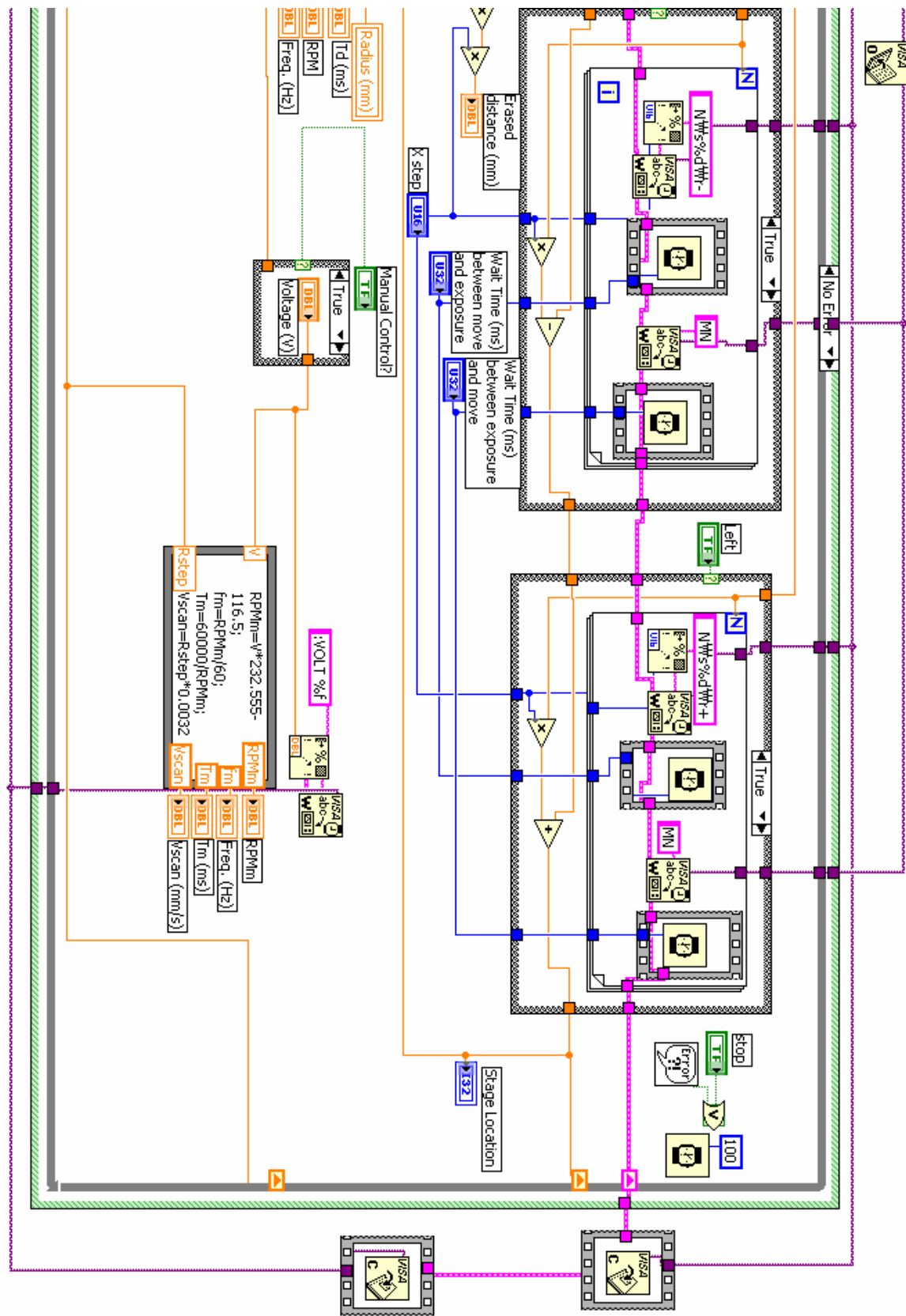
APPENDIX I: ACRONYMS AND ABBREVIATIONS

AFM	Atomic force microscope
ATIP	Absolute time in pre-groove
BD	Blu-ray disc
BS	Beamsplitter
CCD	Charge-coupled device
CD	Compact disc
CD-R	Compact disc recordable
CD-ROM	Compact disc read-only memory
CD-RW	Compact disc rewritable
COMD	Catastrophic optical mirror damage
CTE	Coefficient of thermal expansion
DE	Diffraction efficiency
DOE	Diffractive optical element
DVD	Digital versatile disc
DVD-ROM	Digital versatile disk read-only memory
EX	Exposure dose
FES	Focus error signal
FWHM	Full width at its half of maximum intensity
FW1/e²	Full width at its 1/e ² of maximum intensity
GB	Giga-byte

HD-DVD	High-definition digital versatile disc
HPLD	High-power laser diode
LD	Laser diode
LDRT	Limited-divergence raytracing
LED	Light emitting diode
MB	Mega-byte
MLT	Maskless lithography tool
NA	Numerical aperture
OD	Optical density
ODD	Optical data destruction
OPD	Optical path length difference
PBS	Polarization beamsplitter
PC	Polycarbonate
RLL	Run-length limited
TEC	Thermo-electric cooler
TES	Tracking error signal
WORM	Write once and read many
YDSI	Young's double slit interference

**APPENDIX II: BLOCKDIAGRAM OF LABVIEW PROGRAM CONTROLLING
ODD SYSTEM**





APPENDIX III: PUBLISHED JOURNAL PAPER

The following paper, titled as “Change in data marks and groove structures of compact recordable discs in response to a high power laser beam,” is published in *Optical engineering* in 2006.

Change in Data Marks and Groove Structures of CD-Recordable Discs in Response to a High Power Laser Beam

Taeyoung Choi

Tom D. Milster, FELLOW SPIE

University of Arizona

College of Optical Sciences

Tucson, AZ USA 85721

E-mail: tchoi@optics.arizona.edu

ABSTRACT.

Changes in data marks and groove structures are examined when a high power laser beam ($>0.5\text{W}$) is focused on compact disc recordable (CD-R) data layers. Observations are recorded as a function of exposure condition and the type of dye used in the recording layer. All samples experience a decrease in the depths of data mark features and the pregroove modulations upon exposure. Data marks on cyanine- and azo-dye disks become optically invisible after exposure, while data marks on phthalocyanine-dye disks remain visible even after high-power exposure. Also, phthalocyanine-dye disks show interesting phenomena, including mixture of the dye and the substrate material during recording and contrast reversal of the marks.

Subject terms: optical data storage; optical disks; optical recording; optical storage-

recording materials; high power laser diode.

1 Introduction

Some applications require the complete destruction of data from optical disks. One method for destruction is to use a high-power laser beam that scans over recorded data. In order to assure complete destruction, it is necessary to understand how data marks are formed in writable disks, such as CD-R, CD-RW and DVD±R, and to evaluate the change in recorded data marks upon exposure to a high-power laser beam ($>0.5\text{W}$). In this paper, the mechanisms of data mark formation in writable disks are studied, and the changes in data marks and the groove structure are characterized after disks with different dye materials (cyanine, phthalocyanine, azo) are exposed to a high power laser beam under destruction conditions. The dye/reflector and substrate/dye interfaces of the exposed disks are observed using a high power optical microscope and an atomic force microscope (AFM).

Section 2 of this paper examines how data marks in writable media are formed. Section 3 explains an exposure system used in the experiments. Also, it describes how exposure experiments are performed and samples are prepared for static measurement. Section 4 provides optical and topological measurement results of unexposed and exposed data marks on optical disks with different types of dyes. In addition, the optical images of the samples obtained by use of optical filters and with illumination of infrared light emitting diodes (LEDs) are provided. Conclusions are presented in Section 5.

2 Recording Mechanism in Writable Media

The mechanisms of data mark formation in write-once organic recording media have been extensively studied since the CD-R was developed by Taiyo Yuden in 1989.¹⁻⁴ It is known that several deformation phenomena at the dye/reflector interface and the substrate/dye interface are involved in the formation of a data mark. During the recording process, the energy of a focused laser beam is absorbed by the dye material, increasing the temperature in the dye and substrate layers. As the temperature in the dye layer increases above the dye decomposition temperature (250~300°C), the dye is melted and decomposed, and gas bubbles or pits are formed at the dye/reflector interface. This type of change is called a dye/reflector feature. Also, as the temperature in the substrate/dye interface is increased above the glass transition temperature (140~170°C), the polycarbonate (PC) substrate softens and expands toward the dye layer, and the groove walls are deformed. This type of change is called a substrate feature. Therefore, a data mark in CD-R disks can contain various amounts of dye/reflector and/or substrate features. The combination of both types of features gives rise to changes in reflectivity when the readout beam scans the data mark.

3 Exposure Experiments and Static Measurement Methods

Data marks and groove structures in disks are examined before and after exposure to a high power laser beam. CD-R disks with cyanine, phthalocyanine and azo dyes are used in the experiments. Firstly, data are recorded in the disks using a commercial CD recorder at 48X speed. The recorded disks are then put in an exposure system, which is shown in

Fig. 1. The collimated beam from a high power laser diode ($\lambda=730\text{nm}$, 0.75W, output aperture $100\mu\text{m} \times 1\mu\text{m}$) passes through various optics and is focused onto a disk. The focused beam on the recording layer is a line, because of the wide geometry of the laser output aperture. Therefore, it is possible to expose a number of tracks at a time by situating the focused line beam in the radial direction across tracks.

Exposure dose (EX) is the amount of energy applied per unit area on the dye layer. That is,

$$\text{EX} = \frac{\text{energy}}{\text{scan area}} = \frac{P}{L \cdot v_t}, \quad (1)$$

where P is the laser power through the lens, L is the radial length of the line beam and v_t is the tangential velocity of a focused beam on a disk. Since L is fixed to $40\mu\text{m}$ in the exposure system, there are two adjustable parameters (P, v_t) that are used to vary the exposure dose. Also, the radial velocity v_r should be slow enough to have some overlap in the exposed areas after one disk revolution, and fast enough to minimize the total disk erasure time. The radial velocity is combined in an overlap factor N_o , which is a measure of the portion of the focused beam that overlaps after one revolution of the disk. N_o is expressed as the ratio of the radial beam length to the distance the beam translates during one revolution. That is,

$$N_o = \frac{L}{v_r \cdot T}, \quad (2)$$

where T is the temporal period of revolution. The overlap factor should be greater than one ($N_o > 1$) in order to prevent the focused beam from translating longer than L and

leaving some area unexposed.

Therefore, the exposure dose is adjusted by varying laser power and radial and tangential velocities of the focused beam on a disk. Exposure doses vary, depending on types of dyes in disks, because dyes have different absorptances and reactions to the laser beam. Exposure doses of $4.3\text{nJ}/\mu\text{m}^2$ and $2.8\text{nJ}/\mu\text{m}^2$ are applied to cyanine- and azo-dye disks, respectively. For phthalocyanine-dye disks, exposure doses of $2.2\text{nJ}/\mu\text{m}^2$ and $9.4\text{nJ}/\mu\text{m}^2$ are applied.

The unexposed and exposed sections on disks are examined in two types of static measurement instruments: a high power optical microscope (objective lens: 150X, NA= 0.9) and an AFM. Also, visible wavelength filters (Kodak WRATTEN color filters) and infrared LEDs ($\lambda_{\text{peak}}= 780\text{nm}$) are used in the optical microscope observation of phthalocyanine-dye disks.

Two types of disk samples are prepared in order to see the features on the substrate as well as the dye. For the dye/substrate sample, the lacquer and reflector layers are removed by using air pressure, and, for the substrate-only sample, the dye is dissolved using isopropanol after the lacquer and reflector layers are blown off. The cyanine, phthalocyanine and azo disk samples are observed under the optical microscope and the AFM from the label side.

4 Measurement Results

Firstly, cyanine-dye disks are examined. The optical microscope images of unexposed and exposed data marks are shown in Fig. 2. Unexposed data marks in Fig. 2(a) are

clearly observable before exposure. When exposed to the high-power laser beam ($\text{EX}=4.3\text{nJ}/\mu\text{m}^2$), the data marks on both dye/substrate and substrate-only samples are no longer optically observable, as shown in Figs. 2(b) and (c). Figures 3(a) and (b) illustrate the profiles of a cyanine-dye disk measured using an AFM before and after exposure to the high-power laser beam. The depths of the dye/reflector and substrate features of exposed data marks decrease to less than half the depths of the unexposed data mark features. Also, the pregroove depths decrease from 160nm to 70nm, while the groove depth on the reflector/dye interface is reduced slightly. Furthermore, the angles of the pregroove side walls increase after exposure.

Optical images of the data marks on phthalocyanine-dye disks are shown in Fig. 4. The unexposed data marks on the dye/substrate sample look dark, compared to the land, as shown in Fig. 4(a). After an exposure dose of $2.2\text{nJ}/\mu\text{m}^2$ is applied to the disk, the data marks turn brighter than the land area, as shown in Figs. 4(b). In this case, the contrast of the data marks on the dye/substrate sample reverses after exposure. One hypothesis for the contrast reversal is that phthalocyanine dye at the recorded data marks is not fully inert and responds to additional optical energy, resulting in higher visual-wavelength reflectance of the dye.

In order to verify this hypothesis, a static exposure experiment is performed. While being observed under a high-power optical microscope, recorded data marks are exposed to a tightly focused red laser beam through a microscope objective. The marks turn bright immediately, which supports the hypothesis of phthalocyanine dye still being active after recording. Also, data marks on the substrate-only sample are bright compared to the land

area and become much brighter than the land after high-power exposure ($EX = 2.2\text{nJ}/\mu\text{m}^2$), as shown in Fig. 4(c). The high reflectances of as-written and high-power exposed data marks originate from mixing of the dye and the substrate material. This reasoning is confirmed in an experiment where the substrate-only samples are exposed to a high-power laser beam. If no dye remains in the as-written data-mark areas, no reaction should occur during high-power exposure. Instead, sparking is observed in these areas. The sparking is characteristic of phthalocyanine dye in air under high-power exposure. The dye and substrate mixture is explained by the temperature at the dye/substrate interface that increases instantly above the decomposition temperature of the dye and the melting temperature of the PC during the processes of recording and high-power exposure. The decomposed dye and melted substrate material mix at the recorded marks and high-power exposed areas.

With an increased dose of $9.4\text{nJ}/\mu\text{m}^2$, the dye in no-data-mark areas of both dye/substrate and substrate-only samples turn as bright as the exposed data marks, as shown in Figs. 4(d) and (e). Despite the scattered bright dots, the data marks are still optically discernible. The results of the AFM measurements are shown in Figs. 5(a) and (b). The dye/reflector and substrate features of the data marks are significantly reduced in size. After exposure, as shown in Fig. 5(b), the protruded substrate on the data marks almost flattens, and the pregroove depth is decreased to half the depth before exposure. Therefore, once exposed at $9.4\text{nJ}/\mu\text{m}^2$, data marks on phthalocyanine-dye disks are still visible optically, but barely noticeable topologically.

Curiously, when the data marks of exposed phthalocyanine-dye disks are observed by

use of 780nm LEDs as the illumination source, exposed data marks are not visible, contrary to observable as-written data marks. Therefore, it is difficult to retrieve any data from the exposed phthalocyanine disk using a conventional CD readout system using a 780nm laser diode. On the other hand, the exposed data marks are visible when illuminated by a white light with green and blue color filters. Accordingly, a CD readout system modified with a green- or blue-wavelength laser and an aberration-corrected objective lens might be able to recover data from the exposed disk, if the distortions caused by the exposure are not too severe.

Finally, the optical microscope images of unexposed and exposed data marks on azo-dye disks are shown in Fig. 6. The unexposed data marks on the dye/substrate sample are clearly observable as shown in Fig. 6(a), but contrast of the unexposed data marks on the substrate-only sample is low, as shown in the unexposed area of Fig. 6(c). When the azo-dye disks are exposed at $2.8\text{nJ}/\mu\text{m}^2$, data marks become optically indiscernible, as seen in Figs. 6(b) and (c). However, small bubbles are formed as by-products of fast dye decomposition. The profiles of an azo-dye disk measured using an AFM are presented in Fig. 7. Unexposed data marks on azo-disks have the smallest dye/reflector and substrate features among the three types. Upon exposure, data mark features and the groove modulation are slightly decreased. The surfaces of both dye/reflector and substrate/dye interfaces are rough, due to the bubbles.

Results discussed in the preceding paragraphs were repeatable over disks fabricated by several manufacturers. Although slight ($\pm 10\%$) differences are observed in the power levels required to produce the effects, the physical observations were essentially the same.

5 Conclusions

Recorded CD-R disks are exposed to a high-power laser beam for the purpose of data destruction, and the changes in data marks and groove structure are observed using an optical microscope and an AFM. For the cyanine-dye disks exposed at $4.3\text{nJ}/\mu\text{m}^2$, data marks are optically invisible and the depth modulations of data marks and the grooves are decreased when observed using the AFM. Surprisingly, for phthalocyanine disks, visible-light contrast of data marks are enhanced upon exposure, and the data marks are visible with an optical microscope at the exposure dose of $2.2\text{nJ}/\mu\text{m}^2$. Small bright dots are created on both dye and the substrate at the exposure dose of $9.4\text{nJ}/\mu\text{m}^2$, but the data marks are recognizable. The contrast reversal on the dye/substrate samples could be because phthalocyanine dye at the recorded data marks is not completely inert and reacts to a high power laser beam. Also, the contrast enhancement on the substrate-only samples is due to mixing of the dye and the substrate material. Optical observations of the exposed data marks by use of infrared LEDs and a white light with green and blue filters show that data can not be retrieved in a conventional CD reader. The azo disks exposed at $2.8\text{nJ}/\mu\text{m}^2$ show bubbles in both the dye layer and the substrate. Data marks are optically indistinguishable and pregroove modulation is decreased.

Furthermore, preliminary experiments show that it is possible to destroy optical disks of different formats, such as CD-RW, DVD±R, DVD±RW, BD(Bluray disc)-R and BD-RW. In particular, DVD-format disks are expected to be destroyed in a similar manner as cyanine and azo- dye CD-R disks are obliterated, because cyanine and azo dyes, not

phthalocyanine, are used as recording materials in DVD media.

In summary, data destruction using a high-power laser beam is possible, but successful destruction depends greatly on exposure conditions and the type of dye used in the disk recording layer. This investigation has revealed interesting characteristics of recording using different dye materials, especially with phthalocyanine.

ACKNOWLEDGEMENT

The authors thank Dr. D. Sarid and Mr. R. Grover at the College of Optical Sciences, the University of Arizona, for their help with the AFM measurements.

REFERENCES

- [1] E. Hamada, Y. Shin and T. Ishiguro, "CD-compatible write-once disc with high reflectivity," *Proc. SPIE* **1078**, 80-87 (1989).
- [2] A. H. M. Holtsga, E. R. McCord and G. H. Werumeus Buning, "Recording mechanism of overcoated metallized dye layers on polycarbonate substrates," *Jpn. J. Appl. Phys., Part I* **31**(2B), 484-493 (1992).
- [3] E. Hamada, T. Fuji, Y. Takagishi and T. Ishiguro, "Recording process of recordable compact disc," *Proc. SPIE* **1663**, 443-446 (1992).
- [4] Y. J. Huh, J. S. Kim, T. Y. Nam and S. C. Kim, "Deformation effects and recording characteristics of compact disc-recordables," *Jpn. J. Appl. Phys., Part I* **36**(2B), 403-409 (1997).

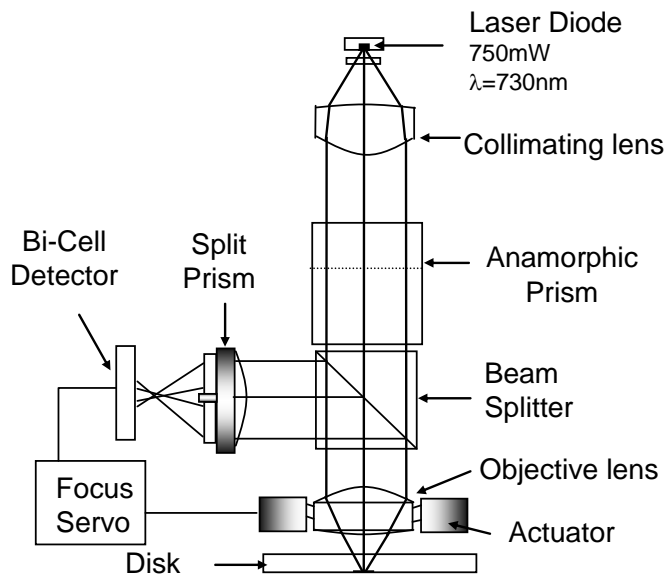


Fig. 1 A schematic of a laser exposure system for data destruction. The beam from a high power laser diode is collimated, passes through various optics and focused on the recording layer of a disk. The focus-lock is achieved with a bi-prism focus sensor and a closed-loop feedback servo.

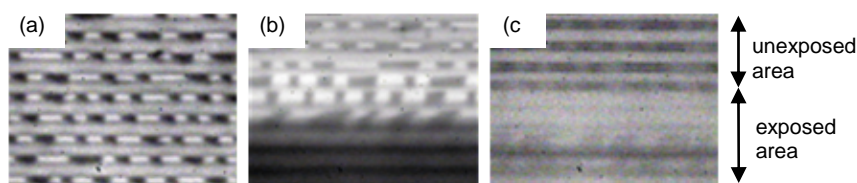


Fig. 2 Optical microscope images of unexposed and exposed data marks on cyanine disks. (a) Unexposed data marks on dye/substrate sample, (b) exposed data marks on dye/substrate sample ($\text{EX}= 4.3\text{nJ}/\mu\text{m}^2$) and (c) exposed data marks on substrate-only sample ($\text{EX}= 4.3\text{nJ}/\mu\text{m}^2$). In (b) and (c), the upper portion of the observation area is unexposed.

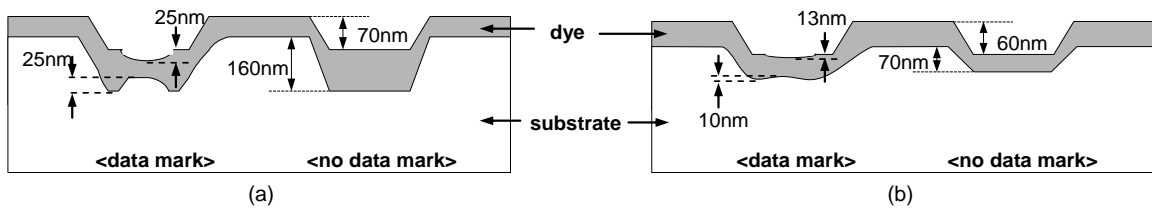


Fig. 3 Profiles of a cyanine-dye disk measured using an AFM (a) before and (b) after exposure to a high-power laser beam ($EX = 4.3\text{nJ}/\mu\text{m}^2$).

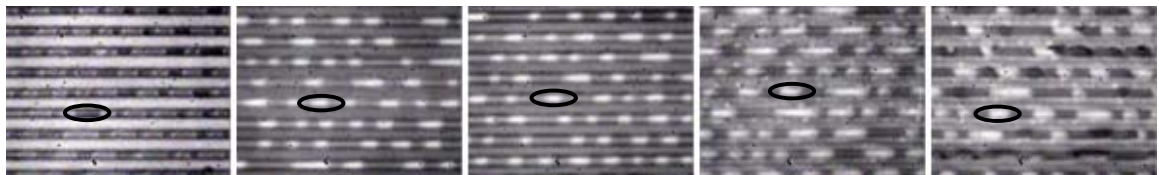


Fig. 4 Optical microscope images of unexposed and exposed data marks on phthalocyanine disks. (a) Unexposed data marks on dye/substrate sample, (b) exposed data marks on dye/substrate sample ($EX = 2.2\text{nJ}/\mu\text{m}^2$), (c) exposed data marks on substrate-only sample ($EX = 2.2\text{nJ}/\mu\text{m}^2$), (d) exposed data marks on dye/substrate sample ($EX = 9.4\text{nJ}/\mu\text{m}^2$) and (e) exposed data marks on substrate-only sample ($EX = 9.4\text{nJ}/\mu\text{m}^2$).

In each figure, a representative data mark is circled.

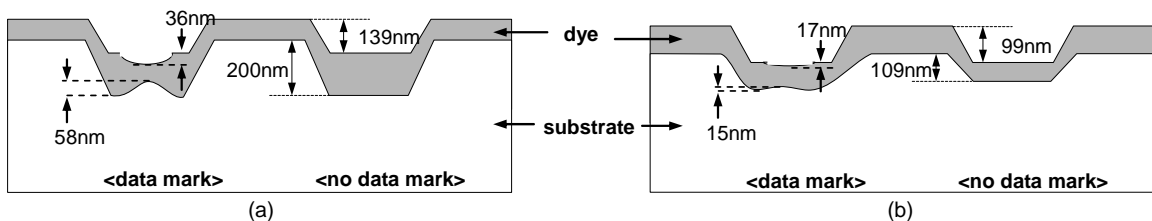


Fig. 5 Profiles of a phthalocyanine-dye disk measured using an AFM (a) before and (b) after exposure ($EX = 9.4\text{nJ}/\mu\text{m}^2$).

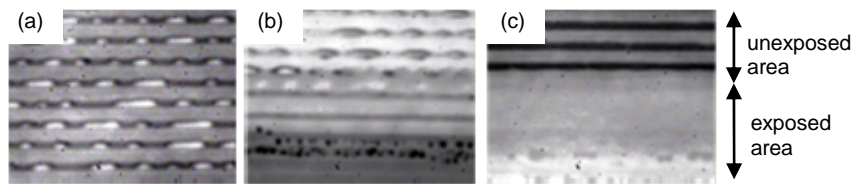


Fig. 6 Optical microscope images of unexposed and exposed data marks on azo disks. (a) Unexposed data marks on dye/substrate sample, (b) exposed data marks on dye/substrate sample and (c) exposed data marks on substrate-only sample. In (b) and (c), a small upper portion of the observation area is unexposed.

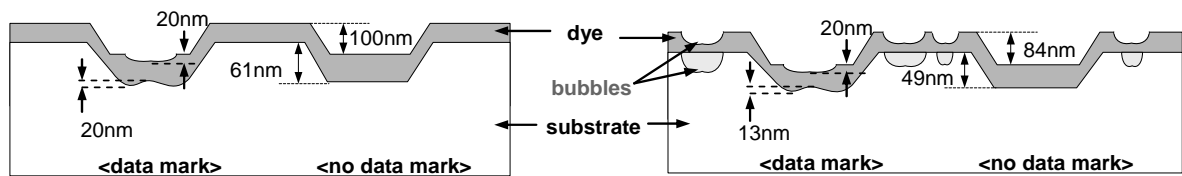


Fig. 7 Profiles of an azo-dye disk measured using an AFM (a) before and (b) after exposure to a laser beam ($EX = 2.8 \text{nJ}/\mu\text{m}^2$).

REFERENCES

- Akhavan, F. and T. D. Milster, "CD-R and CD-RW optical disk characterization in response to intense light sources," Proc. SPIE **3806**, 84-91 (1999).
- Alon A. and T. Kosoburd, "Multi-Beam Optical Pickup," US Patent 6,411,573 (2002).
- Arora, V. K. and A. L. Dawar, "Laser-induced damage studies in silicon and silicon-based photodetectors," Appl. Opt. **35**, 7061-7065 (1996).
- Bachmann, F. G, "Chances and Limitations of High Power Diode Lasers," Proc. SPIE **5336**, 95-106 (2004).
- Bélanger, P. A., "Beam propagation and the ABCD ray matrix," Opt. Lett. **16**(4), 196-198 (1991).
- Born M. and E. Wolf, *Principles of Optics*, 7th Ed., Cambridge University Press, Cambridge (1999).
- Bouwhuis G. and J. Braat, "Video disk player optics," Appl. Opt. **17**(13), 1993-2000 (1978).
- Brenner K. H. and J. Jahns, *Microoptics: From Technology to Applications*, Springer, New York (2004).
- Champagne, Y., "Second-moment approach to the time-averaged spatial characterization of multiple-transverse mode laser beams," J. Opt. Soc. Am. A., **12**(8), 1707-1714 (1995).
- Champagne Y., S. Mailhot, and N. McCarthy, "Numerical Analysis Procedure for the Lateral-Mode of Broad-Area Semiconductor Lasers with an External Cavity," IEEE J. Quantum. Electron., **31**(5) 795-810 (1995).
- Chang-Hasnain, C. J., E. Kapon, and R. Bhat, "Spatial mode structure of broad-area semiconductor quantum well lasers," Appl. Phys. Lett. **54**, 205-207 (1989).
- Chernyshov, A. K., S. P. Kotova, and V. L. Velichanskii, "Characterization and spatial matching of laser diode beams," J. Russ. Laser Res., **23**(2), 132-147 (2002).
- Choi, T. and T. D. Milster, "Change in data marks and groove structures of compact recordable discs in response to a high power laser beam," Opt. Eng. **45**(6), 064302 (2006).

REFERENCES - *Continued*

- Cohen, D. K., "Analysis of methods for detecting focus error in optical data storage system," Ph.D dissertation (University of Arizona, Tucson, Ariz., 1987)
- Cook, D. D. and F. R. Nash, "Gain-induced guiding and astigmatic output beam of GaAs lasers," *J. Appl. Phys.* **46**, 1660-1672 (1975).
- Diehl, R., *High-Power Diode Lasers: Fundamentals, Technology, Applications*, Springer-Verlag, New York (2000).
- Franaszek, P.A., "Run-Length-Limited Variable Length Coding with Error Propagation Limitation", U.S. Patent 3,689,899 (1972).
- Giuliani, J. F. and C. L. Marquardt, "Electrical effects in laser-damaged phototransistors," *J. Appl. Phys.* **45**, 4993 (1974).
- Hamada, E., Y. Shin and T. Ishiguro, "CD-compatible write-once disc with high reflectivity," *Proc. SPIE* **1078**, 80-87 (1989).
- Hamada, E., T. Fuji, Y. Takagishi and T. Ishiguro, "Recording process of recordable compact disc," *Proc. SPIE* **1663**, 443-446 (1992).
- Harvey, K. C. and C. J. Myatt, "External-cavity diode laser using a grazing-incidence diffraction grating," *Opt. Lett.* **16**(12), 910-912 (1991).
- Holtslag, A. H. M., E. R. McCord and G. H. Werumeus Buning, "Recording mechanism of overcoated metallized dye layers on polycarbonate substrates," *Jpn. J. Appl. Phys., Part I* **31**(2B), 484-493 (1992).
- Huh, Y. J., J. S. Kim, T. Y. Nam and S. C. Kim, "Deformation effects and recording characteristics of compact disc-recordables," *Jpn. J. Appl. Phys., Part I* **36**(2B), 403-409 (1997).
- Iwasaki, H., Y. Ide, M. Harigaya, Y. Kageyama, I. Fujimura, "Completely Erasable Phase Change Optical Disc," *Jpn. J. Appl. Phys. Part 1* **31**(2B), 461-465 (1992).
- Kasanavesi, S. K., T. D. Milster, D. Felix, and T. Choi, "Data recovery from a compact disc fragment," *Proc. SPIE* **5380**, 116-127 (2004).
- Kingslake, R., *Lens Design Fundamentals*, Academic, New York (1978).

REFERENCES - *Continued*

- Kintzer, E. S., J. N. Walpole, S. R. Chinn, C. A. Wang, L. J. Missaggia, "High-power, strained-layer amplifiers and lasers with tapered gain regions," *Photon. Tech. Lett., IEEE*, **5**(6), 605-608 (1993).
- Kruer, M., R. Allen, L. Esterowitz and F. Bartoli, "Laser damage in silicon photodiodes" *Opt. and Quantum Electron.* **8**(5), 453-458 (1976).
- Lammert, R.M., M.L. Osowski, S.W., Oh, C., Panja, J.E., and Ungar, "High power (>10W from 100 /spl mu/m aperture) high reliability 808nm InAlGaAs broad area laser diodes," *Electron. Lett.*, **42**(9), 49-50 (2006).
- Li, L., "The advances and characteristics of high-power diode laser materials processing," *Opt. and Lasers in Engineering*, **34**(4-6), 231-253 (2000)
- Løbel, M., P. M. Petersen, and P. M. Johansen, "Single-mode operation of a laser-diode array with frequency-selective phase-conjugate feedback," *Opt. Lett.* **23**, 825-827 (1998).
- MacCormack, S. M. and J. Feinberg, "High-brightness output from a laser-diode array coupled to a phase-conjugating mirror," *Opt. Lett.* **18**, 211-213 (1993).
- Mailhot, S., Y. Champagne, and N. McCarthy, "Single-mode operation of a broad-area semiconductor laser with an anamorphic external cavity: experimental and numerical results," *Appl. Opt.* **39**, 6806-6813 (2000).
- Marchant, A. B., *Optical Recording: A Technical Overview*, Addison Wesley, Boston (1990).
- Milster, T. D., "Physical Optics Simulation in Matlab for High-Performance Systems," *Opt. Rev.* **10**(4), 246-250 (2003).
- Milster, T. D., "Optical Data Storage," in *The Optics Encyclopedia: Basic Foundations and Practical Applications*, T. G. Brown, K. Creath, H. Kogelnik, M. A. Kriss, J. Schmit, M. J. Weber, Eds., Wiley-VCH, Germany (2004).
- Mittelstein, M., J. Salzman, T. Venkatesan, R. Lang, and A. Yariv, "Coherence and focusing properties of unstable resonator semiconductor lasers", *Appl. Phys. Lett.* **46**(923) (1985).
- Moser, A., "Thermodynamics of facet damage in cleaved AlGaAs lasers," *Appl. Phys. Lett.* **59**, 522-524 (1991).

REFERENCES - *Continued*

- Moser, A. and E. E. Latta, "Arrhenius parameters for the rate process leading to catastrophic damage of AlGaAx-GaAs laser facets," *J. Appl. Phys.* **71**, 4848-4853 (1992).
- Pan, M. -W., D. J. Evans, G. R. Gray, L. M. Smith, R. E. Benner, C. W. Johnson, and D. D. Knowlton, "Spatial and temporal coherence of broad-area lasers with grating feedback," *J. Opt. Soc. Am. B* **15**(10), 2531-2536 (1998)
- Photon Inc., "Measuring Astigmatism the Easy Way," Application Note 6410, Photon Inc., Santa Clara, CA (1992).
- Salzman, J., R. Lang, A. Larson, and A. Yariv, "Unstable resonator cavity semiconductor lasers," *Appl. Phys. Lett.* **46**, 218-220 (1985).
- Self, S. A., "Focusing of spherical Gaussian beams," *Appl. Opt.* **22**(5), 658-661 (1983).
- Siegman, A. E., *Lasers*, University Science Books, Mill Valley, CA (1986).
- Siegman, A. E., "New developments in laser resonators," *Proc. SPIE*, **1224**, 2-14 (1990).
- Smith, W., *Modern optical Engineering*, 3rd Ed., MacGraw-Hill, New York (2000).
- Sun, H., "Measurement of laser diode astigmatism," *Opt. Eng.* **36** 1082-1087 (1997).
- Tamkin, J. M., B. Bagwell, B. T. Kimbrough, G. Jabbour, and M. R. Descour, "High speed gray scale laser direct write technology for micro-optic fabrication," *Proc. SPIE* **4984**, 210-218 (2003).
- Wang, M. S. and T. D. Milster, "Differential wax-wane focus servo," *Appl. Opt.* **32**(25), 4797-4807 (1993).
- Watkins, S. E., C. Z. Zhang, R. M. Walser, and M. F. Becker, "Electrical performance of laser damaged silicon photodiodes," *Appl. Opt.* **29**(6), 827-835 (1990).
- Wolf, E. and G. S. Agarwal, "Coherence theory of laser resonator modes," *J. Opt. Soc. Am. A* **1**, 541-546 (1984).